

COMPUTATIONAL ASSESSMENT OF EFFECTIVE DOSE AND PATIENT SPECIFIC  
DOSES FOR KILOVOLTAGE STEREOTACTIC RADIOSURGERY OF WET  
AGE-RELATED MACULAR DEGENERATION

By

JUSTIN MITCHELL HANLON

A DISSERTATION PRESENTED TO THE GRADUATE SCHOOL  
OF THE UNIVERSITY OF FLORIDA IN PARTIAL FULFILLMENT  
OF THE REQUIREMENTS FOR THE DEGREE OF  
DOCTOR OF PHILOSOPHY

UNIVERSITY OF FLORIDA

2010

© 2010 Justin Mitchell Hanlon

To my Mom and Dad,  
for all of the support they have given me over the years

## ACKNOWLEDGMENTS

I would like to express my sincere gratitude to my advisor, Dr. Wesley Bolch, for the opportunity he has afforded me and his guidance towards the completion of my degree. I would like to extend additional thanks to the remainder of my committee: Drs. David Hintenlang, Glenn Sjoden, Wesley “Clay” Smith, Choonsik Lee, and Erik Chell. Erik, not only a member of my committee but an employee of Oraya, has always been a pleasure to work with on this project. Special thanks are extended to Choonsik, who shared his immense wealth of knowledge, and educated me to my present level of expertise. I must also express my appreciation to the rest of the staff at Oraya Therapeutics for both their financial and valuable research support. Michael Gertner and Steven Hansen have had a vision for Oraya, and it has been a wonderful opportunity to watch it grow and to have been a small part of the process. Working with Michael “Mario” Firpo has been a pleasant experience, as he has always provided invaluable advice and suggestions, specifically with the revision of several of my manuscripts. Your keen eye has been an integral part of this project.

I would like to acknowledge NRE staff members Diana Dampier, Ruth Brumbaugh, Terri Sparks, and Donna Seifert, all of whom have been helpful during my time in the department. I would like to recognize Dr. David Gilland, a professor for a number of my graduate courses, for his quality of instruction and engaging classes.

I would like to reflect on my past experiences and thank several others who have assisted me in reaching my goals and dreams. I can still remember the first person that inspired my interest in science, and for that I must acknowledge Mrs. Little, my high school chemistry teacher. I wish to thank her for the invaluable experience of preparing me for college level research at a very young age. I would like to extend my gratitude to

Dr. George Xu, my advisor at Rensselaer Polytechnic Institute, for the opportunity to perform several years of undergraduate research, which undoubtedly prepared me for graduate level work. I would also like to thank Dr. Bryan Bednarz, at the time a graduate student of Dr. Xu's, who gave me some valuable advice and served as a role model during my time at RPI as an undergraduate student.

# TABLE OF CONTENTS

	<u>page</u>
ACKNOWLEDGMENTS.....	4
LIST OF TABLES.....	8
LIST OF FIGURES.....	9
ABSTRACT .....	11
CHAPTER	
1 INTRODUCTION .....	13
1.1 AMD Disease.....	13
1.2 Current Treatments.....	16
1.3 IRay™.....	18
1.3.1 Description of Kilovoltage Stereotactic Radiosurgery for AMD.....	18
1.3.2 The Macula and Fovea Offset.....	19
1.4 Objectives of This Research.....	20
2 DIMENSIONAL DATA FOR OCULAR ANATOMY AND THE OPTIC NERVE PATHWAY VIA 1-mm COMPUTED TOMOGRAPHY IMAGE SETS.....	27
2.1 Purpose .....	27
2.2 Data Collection and Measurement Parameters .....	28
2.3 Analysis of CT Data .....	32
2.4 Alternative Approach for Future Studies .....	35
2.5 Conclusions Pertaining to Development of Models for AMD Treatment Simulation .....	36
3 ANTHROPOMETRIC PHANTOMS EMPLOYED.....	48
3.1 History of Computational Phantoms.....	48
3.2 UF NURBS Hybrid Reference Models .....	49
3.2.1 Head Model Detail.....	50
3.2.2 Ocular Model Detail.....	51
3.2.3 Optic Nerve Model Detail .....	52
3.3 Patient Specific Phantoms .....	53
3.3.1 Selection and Development .....	53
3.3.2 Expanded (3D) Angular Measurements .....	54
3.3.3 Patient Specific Treatment Planning .....	56
3.4 Voxelization .....	58

4	COMPUTATIONAL METHODS .....	70
4.1	The Monte Carlo Radiation Transport Code MCNPX .....	70
4.2	Monte Carlo Techniques Used for Treatment Modeling.....	71
4.2.1	Cell and Surface Cards .....	71
4.2.2	Source Definition .....	72
4.2.3	Tally Specification .....	72
4.2.4	Material, Mode, and NPS Cards.....	74
4.3	Post Processing.....	75
4.3.1	Calculation of Effective Dose .....	75
4.3.2	Utilizing Mesh Tally Output.....	77
5	TREATMENT OUTCOME EVALUATION AND ANALYSIS .....	79
5.1	Radiation Dose Thresholds for Complications .....	79
5.2	Reference Model Dose Assessment.....	80
5.2.1	Tissue-specific Mean Absorbed Doses .....	80
5.2.2	DVH Analysis .....	81
5.2.3	Effective Dose .....	83
5.3	Patient Specific Dose Assessment .....	84
5.4	Photon Fluence Evaluation.....	86
6	CONCLUSIONS .....	103
6.1	Limitations of This Work.....	103
6.2	General Conclusions.....	105
6.3	Future Work.....	108
APPENDIX		
A	EXAMPLE OF MCNPX INPUT CODE .....	109
B	SAMPLES OF MATLAB CODES .....	111
LIST OF REFERENCES .....		116
BIOGRAPHICAL SKETCH.....		121

## LIST OF TABLES

<u>Table</u>	<u>page</u>
2-1	Statistical summary of ocular length measurement parameters ..... 38
2-2	Statistical summary of optic nerve length measurement parameters ..... 38
2-3	Regression coefficients, number of samples, and $R^2$ value for Gaussian probability density function for gender-independent measurement parameters . 39
2-4	Regression coefficients, number of samples, and $R^2$ value for Gaussian probability density function for gender-dependent measurement parameters .... 39
3-1	Comparison of tissue masses in the UF hybrid NURBS and voxel male head phantoms with those given in ICRP Publication 89 for the reference adult male..... 60
3-2	Comparison of tissue masses in the UF hybrid NURBS and voxel female head phantoms with those given in ICRP Publication 89 for the reference adult female..... 61
4-1	Tissue weighting factors for the calculation of effective dose as given by ICRP 103..... 78
5-1	Mean absorbed dose (mGy) to various tissues in the reference head models for a 3 x 8 Gy Oraya Treatment to the right eye ..... 87
5-2	Mean whole-body absorbed doses $D_T$ (mGy) for the estimate of the effective dose..... 87
5-3	The gaze angles, voxelized optic nerve volume, and percentage of that volume receiving more than the absorbed dose listed, representing the dose distribution, for a cumulative 24 Gy treatment dose to the macula ..... 88
5-4	The voxelized lens volume and percentage of that volume receiving more than the absorbed doses listed, representing the dose distribution, for a cumulative 24 Gy treatment dose to the macula..... 89
5-5	The voxelized macula volume and percentage of that volume receiving more than the absorbed doses listed, representing the dose distribution, for a cumulative 24 Gy treatment dose to the macula..... 90
5-6	The highest tissue-averaged doses received from the set of 32 eyes undergoing treatment simulation and the associated eye model ..... 91

## LIST OF FIGURES

<u>Figure</u>		<u>page</u>
1-1	Schematic of an axial cross section of ocular anatomy .....	24
1-2	IRay™ (Oraya Therapeutics, Inc., Newark, CA) .....	25
1-3	Schematic of the treatment geometry for a right eye .....	25
1-4	I-Guide™ (Oraya Therapeutics, Inc., Newark, CA).....	26
1-5	Typical retinal geography highlighting the optic disc, fovea, posterior pole, and Oraya Shift.....	26
2-1	Schematic of an axial cross-section of a pair of eyes (not to scale), indicating those anatomic parameters obtained via measurement within a single CT image slice.....	40
2-2	Schematic of a sagittal cross-section of an eye (not to scale), indicating those anatomic parameters obtained via measurement within multiple CT images .....	41
2-3	CT images of the right orbit of male subject A .....	42
2-4	Schematic of the Frankfurt plane and normalization parameter .....	43
2-5	Dimensions and locations of tissue structures within the human eye as provided in NCRP Report No. 130.....	44
2-6	Correlation scatter plot for parameter $M_1$ versus parameter $M_i$ .....	44
2-7	Histograms for gender-dependent ocular measurements.....	45
2-8	Histograms for gender-dependent optic nerve measurements.....	46
2-9	Histograms for gender-independent measurements.....	47
3-1	The whole body male (left) and female (right) reference phantoms developed within the Advanced Laboratory for Radiological Dosimetry Studies.....	62
3-2	University of Florida NURBS male (left) and female (right) head models based on organ masses listed in ICRP Publication 89 .....	63
3-3	Dimensions of the tissues structures in the NURBS eye model .....	63
3-4	Engineering drawings of the eye detail embedded within the reference NURBS head model .....	64

3-5	Male NURBS eye models with five optic nerve variations (red), the macula targets (green), and the lenses (blue).....	65
3-6	Segmentation of the lens (blue), globe (orange), optic nerve (red), brain (purple), and skull (teal) from a 1 mm axial CT image of the orbital region .....	65
3-7	Patient specific models in object file format generated from three-dimensional reconstruction of 1 mm CT data (shown without skin) .....	66
3-8	Scatter plots of optic nerve tilt as a function of gaze angle .....	67
3-9	Coronal (left) and sagittal (right) views of the head model voxelized to 1 mm <sup>3</sup> resolution .....	68
3-10	Cropped eye section voxelized to 0.5 mm <sup>3</sup> resolution .....	68
3-11	Axial cross sectional view of a patient specific model voxelized to 0.5 mm <sup>3</sup> resolution .....	69
4-1	MCNPX plot of the male eye section model voxelized to 0.5 mm <sup>3</sup> resolution.....	78
5-1	DVHs for the 'mean' optic nerves .....	91
5-2	DVHs for the extremes of male optic nerve tilt .....	92
5-3	DVHs for the extremes of female optic nerve tilt.....	93
5-4	Spatial contour map of the dose distribution within the reference eye model of the adult male .....	94
5-5	Dose contour maps for patient model mer .....	95
5-6	Dose contour maps for patient model fkl .....	96
5-7	Dose contour maps for patient model fjl .....	97
5-8	Correlation scatter plots of mean absorbed dose to the optic nerve as a function of gaze angle .....	98
5-9	Correlation scatter plot and linear regression of optic nerve hotspot dose as a function of optic nerve thickness.....	99
5-10	Phase space diagram of energy and angular dependence of photon fluence 50 cm from the macula target.....	99
5-11	Photon fluence distribution plots 50 cm from macula target .....	100
5-12	Photon fluence contour maps at the edge of the lattice structure .....	101

Abstract of Dissertation Presented to the Graduate School  
of the University of Florida in Partial Fulfillment of the  
Requirements for the Degree of Doctor of Philosophy

COMPUTATIONAL ASSESSMENT OF EFFECTIVE DOSE AND PATIENT SPECIFIC  
DOSES FOR KILOVOLTAGE STEREOTACTIC RADIOSURGERY OF WET  
AGE-RELATED MACULAR DEGENERATION

By

Justin Mitchell Hanlon

August 2010

Chair: Wesley Bolch

Major: Nuclear Engineering Sciences

Age-related macular degeneration (AMD) is a leading cause of vision loss and a major health problem for people over the age of 50 in industrialized nations. The current standard of care, ranibizumab, is used to help slow and in some cases stabilize the process of AMD, but requires frequent invasive injections into the eye. Interest continues for stereotactic radiosurgery (SRS), an option that provides a non-invasive treatment for the wet form of AMD, through the development of the IRay™ (Oraya Therapeutics, Inc., Newark, CA). The goal of this modality is to destroy choroidal neovascularization beneath the pigment epithelium via delivery of three 100 kVp photon beams entering through the sclera and overlapping on the macula delivering up to 24 Gy of therapeutic dose over a span of approximately 5 minutes. The divergent x-ray beams targeting the fovea are robotically positioned and the eye is gently immobilized by a suction-enabled contact lens. Device development requires assessment of patient effective dose, reference patient mean absorbed doses to radiosensitive tissues, and patient specific doses to the lens and optic nerve.

A series of head phantoms, including both reference and patient specific, was derived from CT data and employed in conjunction with the MCNPX 2.5.0 radiation transport code to simulate treatment and evaluate absorbed doses to potential tissues-at-risk. The reference phantoms were used to evaluate effective dose and mean absorbed doses to several radiosensitive tissues. The optic nerve was modeled with changeable positions based on individual patient variability seen in a review of head CT scans gathered. Patient specific phantoms were used to determine the effect of varying anatomy and gaze.

The results showed that absorbed doses to the non-targeted tissues were below the threshold levels for serious complications; specifically the development of radiogenic cataracts and radiation induced optic neuropathy (RON). The effective dose determined (0.29 mSv) is comparable to diagnostic procedures involving the head, such as an x-ray or CT scan. Thus, the computational assessment performed indicates that a previously established therapeutic dose can be delivered effectively to the macula with IRay<sup>TM</sup> without the potential for secondary complications.

## CHAPTER 1 INTRODUCTION

### 1.1 AMD Disease

Age-related macular degeneration (AMD) is a leading cause of vision loss for people over the age of 50 in the United States and a major health problem worldwide.<sup>1</sup> Advanced AMD has dry and wet forms which lead to blurring or blackening of the central vision while peripheral vision is retained.<sup>2</sup> There is no clear cut definition for AMD; some reserve the diagnosis only for patients who experience vision loss, while others include patients who have any change (drusen or geographic atrophy) to their retinal pigment epithelium (RPE).<sup>3</sup> Drusen are small yellowish-white deposits found near the fovea. Utilizing the latter form of the definition, the majority of patients in the early stages do not experience vision impairment until progression into the advanced stages of the disease. In fact, drusen are present in over half of the population over 70 years of age.<sup>1</sup> Considering the entire population in this age group, 6-8% have the advanced form of the disease resulting in severe visual loss.<sup>4</sup> In the latter stages, central vision loss is associated with either the general geographic atrophy of the RPE (dry form) or development of serous and hemorrhagic detachment of the retina and RPE (wet form).<sup>3</sup> The dry form accounts for about 85% of all AMD cases<sup>4</sup>; however, the wet form accounts for 80-90% of the cases in the advanced stage resulting in severe visual loss.<sup>5</sup>

AMD can have a profound impact on the quality of life of an individual, and unfortunately, despite its importance and severity, there are limited treatment options. This is because the pathophysiology of AMD is largely unknown. Research has shown risk associated with the complement factor H gene. Factor H is a 155 kDa sialic acid

containing glycoprotein that helps regulate complement-mediated immune system response.<sup>6</sup> One study suggests that a single-nucleotide polymorphism in the promoter region of HTRA1 is a major genetic risk factor for AMD.<sup>7</sup> Another more recent study found that the polymorphism Y402H in the complement Factor H is related to the development of AMD, and that the pathophysiology of AMD may be related to several other disorders, suggesting that the formation of drusen may be a systemic and localized immune system reaction that is observed in several tissues including the eye, kidney, and similar plaques in the brain.<sup>6</sup> However, AMD most likely results from the behavior of multiple genes, age, and hereditary traits.<sup>4</sup> Other risks include environmental factors, cigarette smoking, diet, fat intake and obesity, high cholesterol levels, and heavy sunlight exposure.<sup>4</sup>

A brief description of ocular anatomy is essential to understanding the progression of the disease (Figure 1-1). The shell of the eye in the posterior region largely consists of three layers: the retina, choroid, and sclera. The sclera is a fibrous tissue that protects and encases the eye. The choroid is a dense pigment layer that is rich with vasculature which supplies the innermost layers of the eye with nutrients and other essentials. The retina is a thin (~0.5 mm) sensory tissue layer that converts light signal to nerve signal with photoreceptor cells. The macula is a region of the retinal tissue surrounding the fovea, which is responsible for central vision. Bruch's membrane is the inner most layer of the choroid, itself consisting of five layers: the basement membrane of the RPE, the inner collagenous zone, a central band of elastic fibers, the outer collagenous zone, and the basement membrane of the choriocapillaries. The RPE, a part of the retina, provides metabolic support to the photoreceptor cells and transports

metabolic waste from photoreceptor cells through Bruch's membrane to the vasculature in the choroid (choriocapillaries).<sup>8</sup>

Drusen are the earliest clinically detectable sign of the disease, from which vision is retained but some patients report having trouble reading in dim light. There are many types of drusen - hard, soft, semisolid, basal laminar, and calcified - all of which typically form around the fovea.<sup>3</sup> In general, drusen are small yellowish deposits that form between the basement membrane of the RPE and the rest of Bruch's membrane.<sup>3</sup> Their manifestation has been linked to free radical formation from visible light which damages photoreceptor molecules. The RPE is unable to digest the damaged cells correctly and metabolism is altered, resulting in an abnormal secretion of material from the basal cell layer.<sup>9</sup> Laboratory investigations have found partially digested RPE and retinal cell organelles within Bruch's membrane and beneath drusen.<sup>3</sup> However, the formation of drusen remains unclear because these findings may be the result, and not the cause, of drusen.<sup>10</sup>

In the advanced stage of the disease, the dry form of AMD occurs from atrophy of the RPE layer below the retina, causing a loss of rods and cones in the central portion of the eye. The wet (neovascular) form begins with the formation of fibrovascular tissue from the choroids that breaks through Bruch's membrane.<sup>3</sup> This choroidal neovascularization (CNV) grows beneath the RPE or into the sensory retina. As a consequence, there is often leakage and bleeding from the vessels that will lead to increased tension at the macular lesion, resulting in serous or hemorrhagic detachment of the RPE, fibrovascular disciform scarring, or vitreous hemorrhage.<sup>3</sup> These events lead to severe and rapid vision loss, ultimately causing blindness if left untreated.

## 1.2 Current Treatments

There are no treatment options for dry AMD; however, vitamin supplements and antioxidants have been shown to slow the progression of the disease up 25% over a 5 year period.<sup>4</sup> Physicians will monitor the dry form closely until the disease progresses into the more debilitating wet form, for which there are a number of treatments used to help slow the process of the disease. Current treatment modalities include laser therapy,<sup>11</sup> photodynamic therapy (PDT) using verteporfin (Visudyne®, Novartis, Basel, Switzerland),<sup>11-12</sup> intraocular drug therapy with ranibizumab (Lucentis®, Genentech, San Francisco, CA),<sup>13</sup> intraocular therapy using pegaptanib sodium (Macugen®, OSI-Eyetech, New York, NY),<sup>14</sup> and brachytherapy using beta emitting radiation (Epi-Rad90™ Ophthalmic System, NeoVista, Fremont, CA).<sup>15-16</sup> Many consider the vascular endothelium growth factor inhibitor (VEGF-inhibitor), ranibizumab, to be the current standard of care. VEGF inhibitors are commonly associated with cancer treatments since the antibodies competitively bind with VEGF to prevent the growth of proliferating blood vessels. AMD is not cancerous but this treatment is applicable because of the development of choroidal neovascularization that leads to vision loss. The drug is effective but requires frequent, invasive injections into the eye for an indefinite period, a burden on the patient and the healthcare system. Research for improved treatment modalities and combination therapies are ongoing.

Previous to the development of ranibizumab, radiation-based modalities such as external beam photon therapy,<sup>17</sup> external beam proton therapy,<sup>18</sup> and Gamma Knife radiosurgery (GKS)<sup>19-21</sup> were explored as potential non-invasive treatment options for the wet form of the disease. Pilot studies involving the use of both photon and proton external beam radiotherapy typically employed a treatment scheme where 10–20 Gy is

delivered to the macula in 2–3 Gy fractions.<sup>16, 22</sup> Some have produced results of reduction in vision loss, whereas others have failed to show any benefit, and in some cases have shown deleterious effects, such as cataract formation and xerophthalmia.<sup>22</sup> Nevertheless, there have been sufficient pilot clinical trials to suggest that photon radiotherapy may be a viable option to treat AMD if higher fractions can be applied to the macula target, simultaneously limiting non-target tissue toxicity.<sup>22</sup> The most promising study, Bergink *et al*,<sup>23</sup> utilized a treatment scheme delivering a total of 24 Gy in 4 fractions. The results of that study compare the treatment group with an observation group and found significant difference ( $P < 0.08$ ) in terms of visual acuity after 12 months follow-up with no side effects from radiation.

Fractionation schemes in radiation therapy are vital to the efficacy of treatment and can vary widely depending on the location and type of target. The biological effective dose (BED) to the target tissue is not only a function of total dose, but the number of fractions and dose per fraction. Single fraction application is unusual for cancer tumor treatment, but may have significant impact on the ability to successfully treat the choroidal neovascularization (CNV) underlying the macula tissue. Char *et al*,<sup>24</sup> reported borderline positive results by delivering a single fraction of 7.5 Gy, and the Epi-Rad90™ (NeoVista, Fremont, CA) system has been evaluated clinically using a 24 Gy single fraction treatment scheme.<sup>15-16</sup>

The described radiotherapy studies have not demonstrated long-term control of the disease. Considering that brachytherapy requires surgical intervention, and trials have shown some positive results with delivery of ~24 Gy to the macular lesion, a novel non-invasive device for radiation treatment of AMD is being developed by Oraya

Therapeutics, Inc. that delivers a higher therapeutic dose (16 - 24 Gy) in a single fraction. Preliminary experimental data recently obtained in a mini-pig animal model suggest that single fraction kilovoltage stereotactic radiosurgery can be accomplished without adverse effects.<sup>25</sup>

### **1.3 IRay™**

#### **1.3.1 Description of Kilovoltage Stereotactic Radiosurgery for AMD**

Based on the studies suggesting that radiosurgery may be a viable option for AMD treatment, the IRay™ (Figure 1-2) has been developed by Oraya Therapeutics, Inc. (Newark, CA) that addresses many of the inherent limitations of other systems used in the past.<sup>26</sup> This one-time, non-invasive treatment option will provide benefit to patients and the medical community in terms of cost, pain, and hospital time. The goal of this modality is to destroy the CNV beneath the RPE via delivery of three 100 kVp photon beams entering through the pars plana to overlap on the predicted foveal center delivering up to 24 Gy of therapeutic dose over a span of approximately 5 minutes. The anode, with 1 mm<sup>2</sup> focal spot, is 15 cm from the macula target with 0.75 mm Al and 0.8 mm Be filtration. The x-ray beams targeting the fovea are robotically positioned and the eye is gently immobilized by a suction-enabled contact lens. The divergence of the photon beam is characterized by a profile with a diameter of approximately 3.5 mm upon scleral entry and 4 mm at the retina. The three beams, each intersecting and delivering 8 Gy at the target, were chosen to disperse the scleral entry dose, the dose to the edge of the lens closest to each beam, and the dose to the orbital bone and brain tissue.

The beam geometries can be described using a spherical 3D polar coordinate system with the z-axis aligned with the geometric axis of the eye, but transposed by an

offset described subsequently. The *geometric axis* of the eye is defined as the line that intersects the point on the distal portion of the cornea and is perpendicular to the corneal curvature at this point (Figure 1-1). The *posterior pole* is the point where the geometric axis intersects the retina. For all 3 beam angles, the nominal polar angle is 30 degrees; however, if the scleral entry point of the beam is less than 4 mm from the limbus for a given patient treatment, the system will readjust that polar angle until the 4 mm criterion is met. The azimuthal angles are described in the coronal plane of the patient such that 0 degrees is superior to the patient and an angle of 90 degrees would be towards the nose for a treatment of the right eye. The beam azimuthal entry angles chosen for prototype therapies are 150, 180, and 210 degrees and are commonly referred to as the 5, 6, and 7 o'clock beams. Schematics of the beam geometry are presented in Figure 1-3. The treated eye of each patient is gently immobilized by a suction-enabled contact lens with a central post and a control-yoke housing three optically sensed fiducial markers (I-Guide™) (Figure 1-4). Motion of the patient's eye is substantially reduced by the I-Guide™ and the residual motion is tracked in real time using a two-camera imaging system. Eye motion that would result in substantial dose outside the target area triggers an interruption of the x-ray beam. Targeting error due to patient motion is monitored and maintained below 400 μm on the retina.

### **1.3.2 The Macula and Fovea Offset**

In ocular anatomy, the fovea is known to be offset from the posterior pole of the eye (Figure 1-1). An evaluation of this separation was performed in house at Oraya Therapeutics using a customized Canon CR-45 UAF non-mydratic fundus camera with a low-power laser beacon and an anterior imaging system with added collinear at the

imaging axis. When a subject's eye is oriented such that the reflection of the laser beacon and the center of the limbus boundary coincide with the system axis as seen in the anterior eye view, the laser beacon position in the fundus image occurs at the intersection of the geometric axis with the retina (the posterior pole).

Analysis of these fundus images from seven healthy volunteers showed that the nominal fovea is located 1.25 mm laterally and 0.50 mm inferiorly from the posterior pole. This fovea offset, referred to internally to the research team as the *Oraya Shift*, is important because the current treatment involves aligning the system to the geometric axis of the eye, followed by a translation of the device by the offset in order to target the nominal fovea. A retinal geography of the fovea offset is shown in a representative fundus image in Figure 1-5. This offset is important not only for more accurate targeting of subfoveal disease, but also because it moves the treatment beams away from the optic disc, substantially reducing optic nerve dose.

Further studies have confirmed the validity of the offset. A total of 48 additional eyes, both healthy and low vision, were analyzed for the position of the fovea relative to the posterior pole.<sup>27</sup> Similar results were obtained. As part of a larger targeting study, thirteen cadaver eyes were dissected and the position of the fovea was compared to the positions of needles placed through the retina at the point of treatment. The average position of the fovea was found to be within 100  $\mu\text{m}$  in the lateral-medial direction and 100  $\mu\text{m}$  in the superior-inferior direction of the nominal fovea as defined by the offset.<sup>27</sup>

#### **1.4 Objectives of This Research**

Dosimetry characterization of this treatment is an integral part of device development, risk assessment, and the approval process for the Federal Drug

Administration (FDA). Previous Monte Carlo radiation transport simulations were used to provide insight into beam characterizations for optimal therapy applications including focal spot size, maximum tube potential, and azimuthal angles of beam entry.<sup>28</sup> In the present work, the dosimetry characterization of the kilovoltage stereotactic AMD radiosurgery has been expanded and enhanced in a number of areas.

Chapter 2 describes the collection and analysis of 40 head CT scans. Evaluation of the ocular anatomy and optic nerve pathway is presented through the statistical analysis of several measurement parameters. The results of this study provide a better quantitative understanding of the optic nerve pathway and indicate the necessity to use separate models for the detailed ocular anatomy of the male and female during treatment simulations. The range of optic nerve exit tilt angles observed was utilized to evaluate a worst-case-scenario risk assessment.

Chapter 3 highlights the creation of a reference NURBS-based model structure and the fabrication of a 16 patient, 32 eye set of patient specific voxel models. In the process, both a reference adult male and reference adult female head model were constructed consistent with the anatomical data of the International Commission on Radiological Protection's (ICRP) Publication 89.<sup>29</sup> The detailed models include the entire head and neck of the patient including several radiosensitive tissues at potential risk, namely the lens, optic nerve, brain, cranial bone marrow, cranial endosteum, thyroid, and salivary glands. These tissues allow for the assessment of effective dose from this treatment so that comparisons of relative stochastic risk may be made against other medical imaging and therapy procedures. The detailed ocular anatomy combines data from Chapter 5 of Report No. 130 by the National Council on Radiation Protection

and Measurement (NCRP)<sup>30</sup> and ICRP 89. Most importantly, the optic nerve pathways, for both male and female and including both mean and extremes of optic nerve exit tilt, were modeled from data in Chapter 2 of this work. Patient specific models were designed to evaluate dose as a function of varying ocular anatomy and gaze angle.

Chapter 4 details the Monte Carlo methods used to simulate treatment and Chapter 5 presents dosimetry calculations in the form of tissue-specific mean absorbed dose tables, dose volume histograms (DVHs), color coded dose contour maps, and absorbed dose distribution tables. These latter tables are an alternate data format comparable to DVH plots, but allow for condensed presentation and listing of specific quantitative values. Effective dose is calculated using the reference adult male and female head phantoms for a 24 Gy treatment to the macula region. Contributions from both the primary tube output and an estimation of leakage are included in the effective dose calculation. For the patient specific phantoms, trends in dimensional anatomy as a function of absorbed dose are presented and analyzed. Treatment evaluation and analysis includes a comparison between absorbed dose to non-target tissues observed in this study and the generally accepted thresholds for complication and debilitation, specifically the development of cataracts and radiation induced optic neuropathy (RON). Lastly, the energy and angular distribution of photon fluence at a radius of 50 cm from the macula target is presented, along with photon fluence contour maps that provide a visual representation of photon fluence at the edge of the lattice structure used during treatment simulation. The conversion of fluence to dose rate will provide parameters necessary for shielding calculations.

Ultimately, the work of this research will provide a better understanding of the treatment physics and risk of non-invasive kilovoltage stereotactic radiosurgery for AMD.

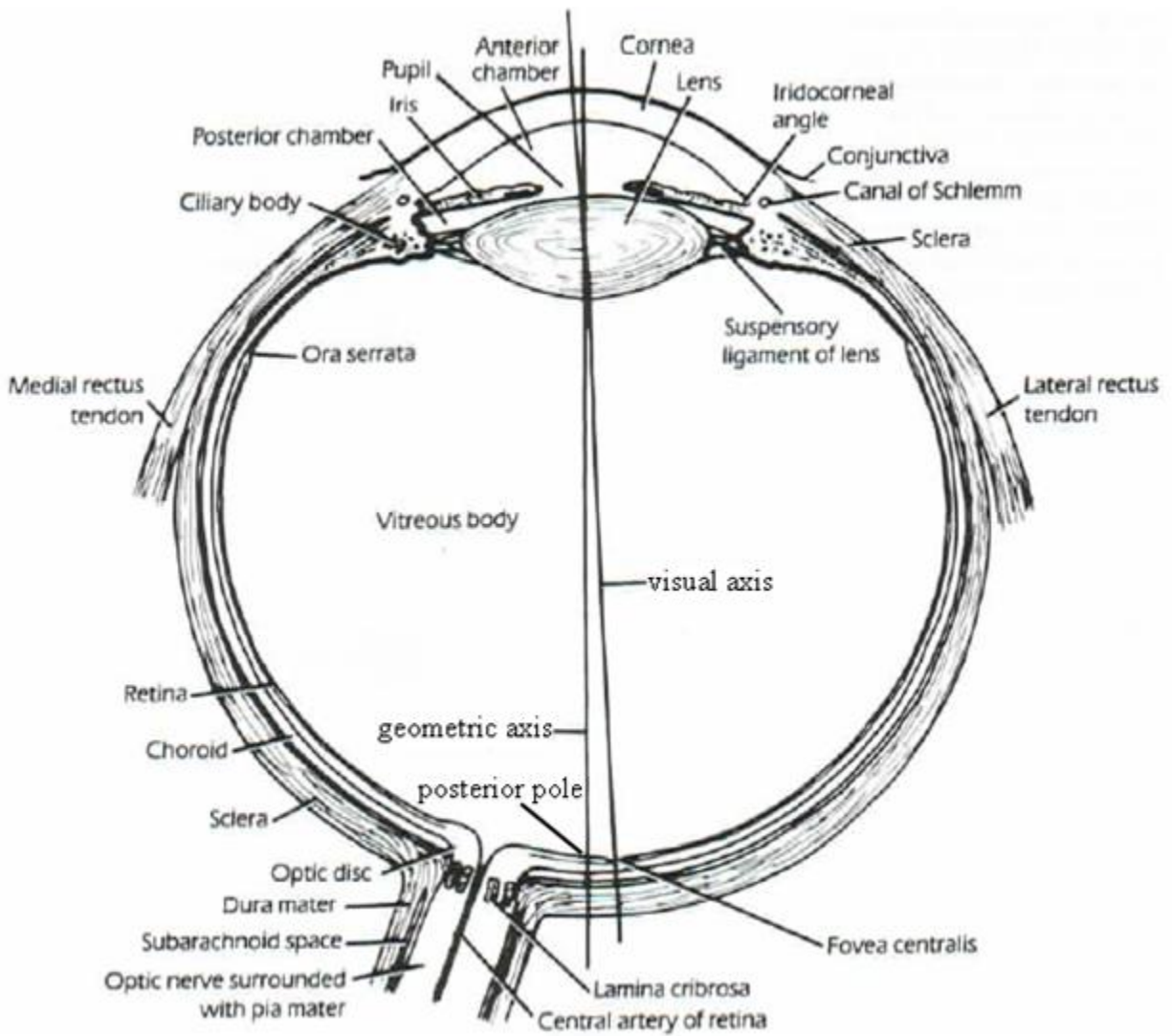


Figure 1-1. Schematic of an axial cross section of ocular anatomy (adapted from Snell<sup>8</sup>)

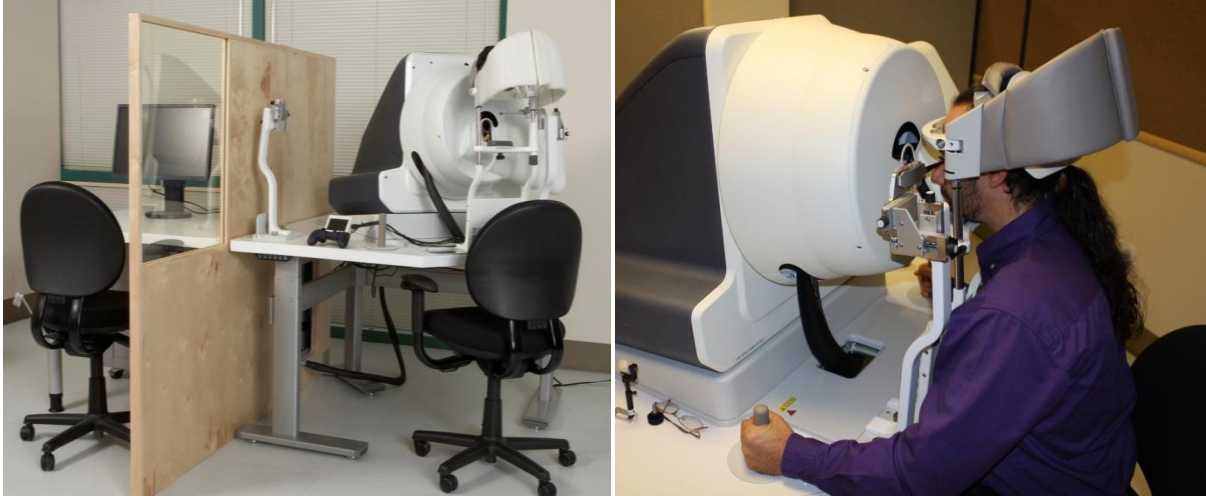


Figure 1-2. IRay™ (Oraya Therapeutics, Inc., Newark, CA)

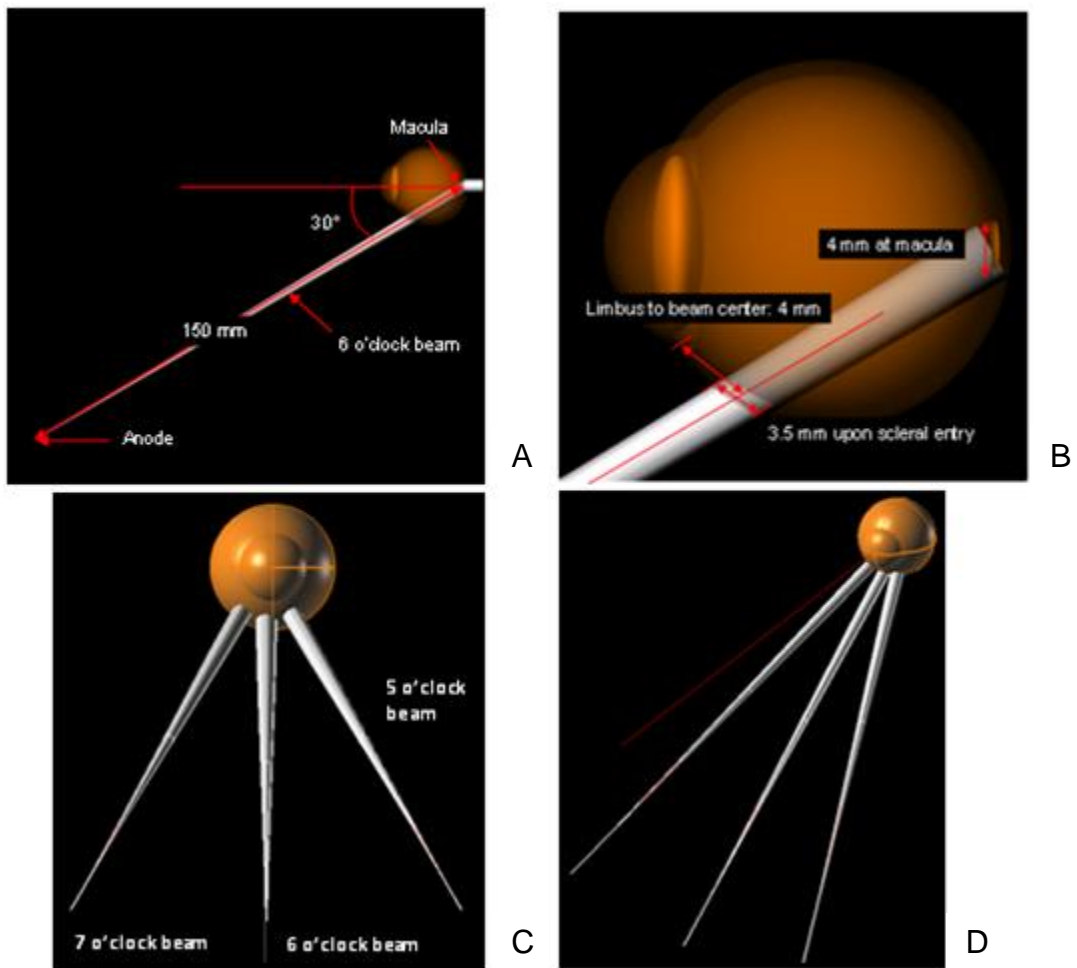


Figure 1-3. Schematic of the treatment geometry for a right eye (A) sagittal view (6 o'clock beam only) (B) sagittal view zoomed in (C) front view (D) perspective view

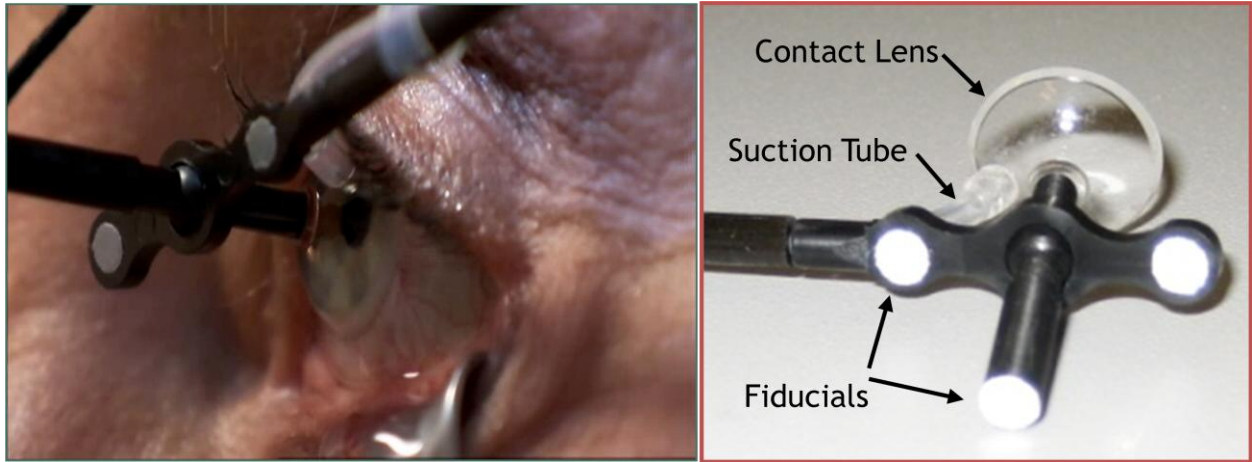


Figure 1-4. I-Guide™ (Oraya Therapeutics, Inc., Newark, CA)

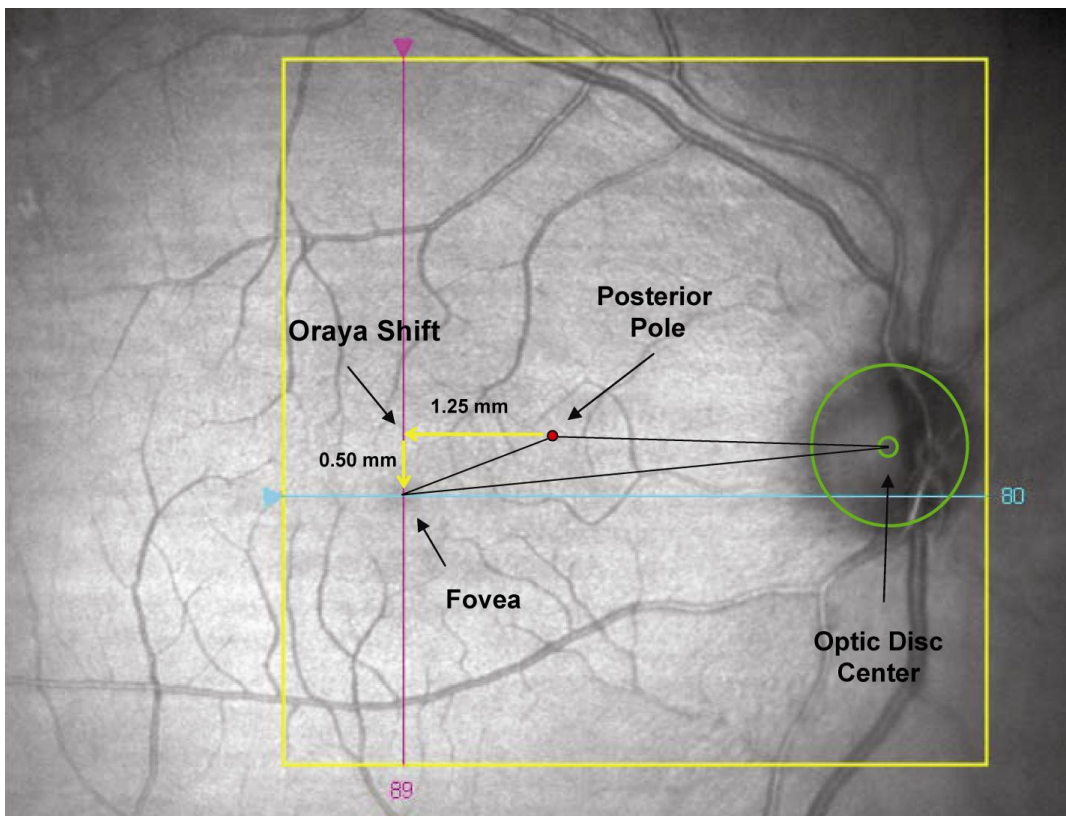


Figure 1-5. Typical retinal geography highlighting the optic disc, fovea, posterior pole, and Oraya Shift

## CHAPTER 2 DIMENSIONAL DATA FOR OCULAR ANATOMY AND THE OPTIC NERVE PATHWAY VIA 1-MM COMPUTED TOMOGRAPHY IMAGE SETS

### 2.1 Purpose

Dimensional data on the eye and optic nerve are critical parameters in the development of radiation treatments for eye disease. Device development and safety assessments require not only the central estimates, but also gender-dependent variability in a potential patient population. Such data, however, are limited in the open literature. Some reference data are given for ocular size measurements in Chapter 5 of Report No. 130 by the National Council on Radiation Protection and Measurement (NCRP),<sup>30</sup> and in Chapter 11 of Publication 89 by the International Commission on Radiological Protection (ICRP).<sup>29</sup> The NCRP 130 eye model is in part based on measurements reported by Charles and Brown,<sup>31</sup> yet other information in the model is unpublished.<sup>32</sup> Furthermore, ICRP 89 reference values are limited to values of only total eye and lens mass. In both sources, no mention is made of gender-dependent variations in ocular structure size or optic nerve pathways.

The anatomical location and function of the optic nerve is well known in a qualitative manner, yet limited data exist to quantify the position of the optic nerve and its pathway within the tissue structures of the human head. The optic nerve can be distinguished in both CT and MR images, but is difficult to image in any one slice because of its shape and size.<sup>33</sup> There are other imaging modalities, such as Optical Coherence Tomography (OCT), that are specialized in imaging the optic nerve for glaucoma-related studies, but these tend to focus on the optic disc rather than the optic pathway.<sup>34</sup> While there is some quantitative information on the movements of the ocular

muscles,<sup>35</sup> limited knowledge exists regarding the optic nerve's movements as a function of eye gaze angle.

In the past, such quantitative knowledge was not necessary for invasive surgical medical procedures involving the eye and its orbit since these structures can easily be localized by the ocular surgeon. Recently, the development of non-invasive stereotactic radiosurgery has become increasingly popular in medical therapies. Non-invasive surgery is a benefit to the patient when considering pain, medical costs, and hospital time. Research for a new type of ocular radiosurgery is underway for the treatment of age-related macular degeneration (AMD) which has shown to have numerous benefits over other types of treatments for this disease.<sup>28, 36</sup> Due to attenuation of the x-ray beams passing through the eye, the proximity of the macula to the optic nerve and disc, and the possibility of damage to these structures from radiation during treatment, the ability to quantify ocular and optic nerve tissue structures is now needed for medical device development and treatment risk assessment.

To address these needs, a retrospective study of 1-mm slice resolution computed tomography images has been undertaken for a 40-patient population of equal numbers of males and females. The study explored differences between male and female eye and optic nerve sizes, which may affect the attenuation of radiation beams passing through the eye during stereotactic radiosurgery. The study also examined optic nerve pathways in both genders to ascertain correlations with eye position, as the location of the optic nerve is of utmost importance during radiosurgery treatment planning.

## **2.2 Data Collection and Measurement Parameters**

With Institutional Review Board approval (IRB #481-2007 University of Florida), 40 CT scans were obtained from Shands Hospital at the University of Florida for

retrospective analysis. The gender distribution was 20 male and 20 female. The requirements for eligible CT sets included (1) maxillofacial axial scans, (2) 1-mm slice resolution, (3) soft tissue contrast settings, and (4) patient age over 18 years. The CT scans were analyzed and measurements made using the image processing code 3D Doctor™ (Able Software Corp., Lexington, MA).

Measurements pertaining to the optic nerve included (1) vertical tilt angle of the optic nerve as it leaves the posterior region of the eye, (2) optic nerve thickness at the posterior region of eye (scleral optic nerve thickness), (3) optic nerve thickness as it passes through the orbit (orbital optic nerve thickness), and (4) optic nerve length from posterior of eye to the posterior region of the orbit. These 4 optic nerve measurement parameters will be referred to as  $M_1$  to  $M_4$ , respectively.  $M_1$  is positive in the superior direction and negative in the inferior direction.

Ocular measurements included (a) apex of cornea to lens distance (corneal depth), (b) lens depth, (c) lens width, (d) eye depth, (e) eye width, (f) combined sclera, choroid, and retinal thickness in the posterior hemisphere of the eye (tri-layer thickness), (g) eye separation from apex of the right cornea to apex of the left cornea, (h) angle between the Frankfurt Plane (defined below) and the axial plane of the CT image (head tilt angle), and (i) vertical gaze angle. These 9 ocular measurement parameters will be referred to as  $M_a$  to  $M_i$ , respectively. The parameters measured on axial images are shown graphically in Figure 2-1.

$M_1$  was calculated using the trigonometric relation  $\tan^{-1}(X/Y)$  where X is obtained by counting the number of CT slices between the axial image that showed the inferior portion of the optic nerve exiting the posterior region of the eye and the axial image that

showed inferior portion of the optic nerve as it exits the orbit, and Y is the compressed, 2D length of the optic nerve. Measurement  $M_4$  was calculated using Pythagorean's Theorem with X and Y given for  $M_1$ . A representation of this method is shown in Figure 2-2A. In many cases, the optic nerve appeared to significantly change direction at some point in its pathway (i.e., the optic nerve displayed some degree of slack in its pathway at more central gaze angles). In such a case, the angle in  $M_1$  was made to the inflection point, rather than to the posterior of the orbit to accurately depict an exit angle. A representation is shown in Figure 2-2B. The inferior side of the optic nerve was chosen for measurements because a clearer distinction could be made at the optic nerve-sclera junction as compared to its superior side.

Figure 2-3 demonstrates the method for these measurements and why it is sometimes important to measure to an alternate point in order to truly represent an appropriate exit angle. Viewing the CT images in an inferior-to-superior order, the optic nerve can be first seen clearly in slice 135 of Figure 2-3, but it does not connect to the eye until slice 137, yielding  $X = -2$  and Y represented by the black line in slice 135. If the angle had been measured to the inferior portion of the optic nerve as it exits the orbit, as highlighted by the black circle in slice 140, X would have been +3, yielding a superiorly tilted angle when in fact the exit angle is inferiorly tilted.

Many of these measured structures can be seen on multiple images with 1-mm slice CT resolution. To keep the ocular measurements ( $M_a$  through  $M_g$ ) consistent from patient to patient, a reference slice was chosen that could be easily identified within every CT image set. Typically, the lens could be identified on ~9 CT images, and so the median slice of this subset was selected as the reference plane. Due to right-left head

tilt, this slice may not be the same for the left and right eyes and, in such a case, measurements to the left and right eye were made on separate reference images, and  $M_g$  was made on either the right or left eye reference slice, whichever had the best view of the opposing cornea.  $M_2$  and  $M_3$  were made on whichever image showed the largest thickness.

The reference plane described is the optimal plane for measurement because it would contain the geometric axis assuming the patient scanned had no head tilt or gaze angle, and it is assumed that the eye is approximately rotationally symmetric around its geometric axis. Under this assumption, the lens and eye width measured correspond to a lens and eye diameter. However, most patients display some form of head tilt and gaze angle within their CT images, and so these parameters were calculated as well. To correct for patient head tilt,  $M_1$  and  $M_i$  were normalized to the Frankfurt plane. Figure 2-4A shows the Frankfurt plane, defined as an axial plane intersecting both the inferior point of the bony orbit and the superior point of the ear canal. The Frankfurt plane is described as being most nearly parallel to the Earth's surface for a person in an upright reference position. A correction factor was measured by performing 3D reconstruction of the patient's skull using an interactive segmentation tool in 3D Doctor<sup>TM</sup>. The resulting polygon mesh file was exported to Rhinoceros 4.0<sup>TM</sup> (McNeel North America, Seattle, WA), as shown in Figure 2-4B, to make an angular measurement between the Frankfurt plane and scanning plane.

Parameter  $M_i$  (vertical gaze angle) was calculated similarly to  $M_1$ , by using the trigonometric relation  $\tan^{-1}(A/B)$  where A is determined from counting the number of CT slices between the median slice of the lens (reference slice described above) and the

medial slice of the optic nerve in the posterior region of the eye (slice contains a good approximation for the posterior pole even though it cannot be visualized in CT images), and B is the compressed, two dimensional length between the two structures (distance measurement made on one of the images between the lens and optic nerve).

Anatomically, A is in the superior-inferior direction (z-direction), B is in the axial plane (x-y plane), and  $M_i$  is the angle between the two. A representation of this measurement is shown in Figure 2-2C.

### 2.3 Analysis of CT Data

Parameters  $M_i$  and  $M_h$  were merely evaluations of patient head and eye positioning during the CT imaging with little correlation between subjects and thus are not relevant to gender-dependent discussions. The standard deviation for vertical tilt ( $M_1$ ) was quite high being 7.8 degrees for men and 8.4 degrees for women. Slice resolution and contrast settings were potential sources of error for parameter  $M_1$ , although this parameter could also be considered arbitrary since gaze angle was not fixed. Consequently, it is useful to give the range for this measurement, which was from -17.6 (inferior tilt) to 15.5 degrees (superior tilt) for the male subjects and from -24.4 (inferior tilt) to 9.7 degrees (superior tilt) for the female subjects. A medial-lateral tilt angle was estimated and ranged from +18.9 to +28.5 degrees, but was not included in statistical analysis because of the absence of consistent anatomical landmarks within the 2D image set to normalize amongst subjects. These angular measurements did not indicate any patterns that would suggest a difference between right and left optic nerves, nor between males and females.

Excluding  $M_1$ ,  $M_h$ , and  $M_i$ , the means, standard deviations, uncertainty, and ranges for ocular and optic nerve parameters are given in Tables 2-1 and 2-2, respectively.

The tables also give the t-values and p-values obtained from performing an unpaired Student's t test between the male and female sample populations. Choosing a statistical significance threshold of 0.05 for the p-value (95% confidence) to reject the null hypothesis, it was determined that there is a gender-dependent difference in means for the following parameters: scleral optic nerve thickness ( $M_2$ ), orbital optic nerve thickness ( $M_3$ ), optic nerve length ( $M_4$ ), eye depth ( $M_d$ ), eye width ( $M_e$ ), and eye separation ( $M_g$ ). For these parameters, gender-dependent means, standard deviations, uncertainty propagations, and ranges are also given in Tables 2-1 and 2-2. The measurements did not indicate patterns that would suggest a difference between right and left eye structures. Uncertainty for each measurement was determined from the diagonal length through a pixel (0.5 mm) and slice resolution (1 mm) of the image set, and propagated to determine the total uncertainty in the mean.

The NCRP 130 eye dimensions are shown in Figure 2-5. Comparing current measurements of  $M_a$  through  $M_f$  and  $M_2$  to corresponding NCRP 130 measurements, parameters  $M_a$ ,  $M_b$ ,  $M_d$ , and  $M_f$  are in agreement, while parameters  $M_c$ ,  $M_e$ , and  $M_2$  indicate that current determination of the diameters of the lens, eye, and optic nerve are smaller in comparison to those given in the NCRP report.

To establish a relationship between vertical optic nerve tilt and vertical gaze angle, a scatter plot and linear regression equation are shown in Figure 2-6. The relationship established was not strong enough to determine a definitive quantitative relationship ( $R^2=0.3377$ ), but there is some correlation between the two parameters. Thus, the vertical optic nerve exit angle is related to the vertical gaze angle, which can be visualized from the three diagrams drawn in Figure 2-2. When looking straight

ahead in the primary gaze position, there appears to be “slack” in the optic nerve. This slack allows the optic disc and nerve to move with the eye when shifting gaze. For an upward gaze, the optic nerve would have a superiorly tilted exit angle, and for a downward gaze it would have an inferiorly tilted exit angle. Furthermore, the length measurements on the anterior portion of the optic nerve give some idea of where a dip normally occurs in the optic nerve slack (14.3 mm for men and 9.6 mm for women).

Figures 2-7 and 2-8 give histograms for gender-dependent ocular and optic nerve parameters, respectively. Figure 2-9 gives histograms for the remaining gender-independent parameters. The bin width in each plot was determined by the following expression:

$$W = 3.49 \sigma N^{-1/3} \quad (2-1)$$

where  $W$  is the bin width,  $\sigma$  is the standard deviation, and  $N$  is the number of samples. The expression gives the optimal bin width for the most efficient unbiased estimation of the probability density function.<sup>37</sup> A three-parameter Gaussian probability density function was derived for each histogram using the following model:

$$pdf = \frac{a \left[ \exp \left( -0.5 \left( \frac{x - x_0}{b} \right)^2 \right) \right]}{N} \quad (2-2)$$

where  $a$ ,  $b$ ,  $x_0$  are fitting coefficients and  $N$  is the number of samples. These values, along with the  $R^2$  values of the curve, are listed in Tables 2-3 and 2-4 for the ocular and optic nerve parameters, respectively. The original Gaussian fit line was normalized by the number of samples to give a probability density function ranging from 0 to 1. The regression lines are statistically strong for most parameters, with  $R^2$  values above 0.95

for each parameter with the exception of  $M_2$  and  $M_4$  (for males only), which were 0.88 and 0.91, respectively.

#### **2.4 Alternative Approach for Future Studies**

While this study provides improved data for these applications, additional improvements are warranted in future studies. CT image contrast is dependent on both the x-ray tube potential (kVp) and tube current (mA) used during patient imaging. As this was a retrospective study, these values were not always consistent from patient to patient. As image contrast varies, it became difficult to differentiate structures with similar Hounsfield numbers, such as optic nerve fibers and myelin sheath, leading to potential variability during the measurement process. Another factor to consider in this analysis was the 1-mm resolution of the CT images, a value chosen because it is one of the highest resolutions readily available for head CT studies. While higher resolution image sets are occasionally taken, they are uncommonly administered in order to reduce radiation dose to the patient. Consequently, the 1-mm resolution offered the highest resolution available for which a relatively large patient population could be sampled. Clearly higher resolution CT image sets would vastly improve some of the measured parameters, namely the vertical optic nerve exit angle and the vertical gaze angle. It should be noted, however, that 3D reconstructions of 2D images, will not provide improved measurement accuracy, as the 3D images involve some data smoothing. Improved accuracy will only be accomplished via higher image resolution, at the expense of patient radiation dose.

An alternative to the retrospective study of computed tomography images presented here would be a prospective study of patients undergoing magnetic resonance (MR) head imaging. MR images would give improved soft-tissue contrast,

and allow for higher resolution slices to be taken without having to account for volunteer radiation dose. Designing such a study would offer a number of other benefits as well, such as limiting head tilt, and scanning patients with forced primary gaze angles as would be the case during stereotactic radiosurgery for AMD. Data from such a study would give a more direct correlation between optic nerve exit angle and gaze angle, and may support the optic nerve movement theory presented here. Relatively long scan times, however, would be required to achieve images approaching the 1-mm slice resolution used in the present CT-based study.

## **2.5 Conclusions Pertaining to Development of Models for AMD Treatment Simulation**

There is currently a need in the medical community for gender-dependent dimensional data for the eye and substructures, as well as for the optic nerve anatomic position and pathway. Such data are important for the development of non-invasive medical procedures such as stereotactic radiosurgery for treatment of wet AMD. The present study examined forty 1-mm head CT image sets, from which gender-dependent means, standard deviations, uncertainty, and ranges were obtained for several anatomic parameters and a relationship between vertical optic nerve exit angle and vertical gaze angle was established.

From the results of the sample population, it could be determined with 95% confidence that there is a difference in gender for the total population for parameters  $M_2$ ,  $M_3$ ,  $M_4$ ,  $M_d$ ,  $M_e$ , and  $M_g$ , while there is no difference between male and female parameters  $M_1$ ,  $M_a$ ,  $M_b$ ,  $M_c$ , and  $M_f$ . Therefore, the average male and female have the same distribution of optic nerve exit angles in the vertical ( $M_1$ ) direction, the same position ( $M_a$ ) and size ( $M_b$  and  $M_c$ ) of the lens within the eye, and the same combined

sclera, choroid, and retinal thickness ( $M_f$ ). As for the parameters with a notable difference, an average male optic nerve is longer ( $M_4$ ) and thicker ( $M_2$  and  $M_3$ ) than an average female optic nerve, making the male optic nerve slightly more difficult to avoid during ocular stereotactic radiosurgery. An average male eye is larger in depth ( $M_d$ ) and width ( $M_e$ ) than that in the average female, which will more heavily attenuate a radiation beam traversing the eye. Parameter  $M_g$  was also larger for males by a more significant margin indicating a larger skull, which corroborates information on gender-dependent reference values given in ICRP Publication 89. As a result, a reference computational model for pre-clinical dosimetry evaluations for AMD kilovoltage radiosurgery should employ separate models, particularly for the optic nerve detail, for male and female patients.

Table 2-1. Statistical summary of ocular length measurement parameters

		M <sub>a</sub> mm	M <sub>b</sub> mm	M <sub>c</sub> mm	M <sub>d</sub> mm	M <sub>e</sub> mm	M <sub>f</sub> mm	M <sub>g</sub> mm
Total	mean	3.18 ± 0.06	3.82 ± 0.06	8.28 ± 0.06	24.27 ± 0.06	25.11 ± 0.06	1.22 ± 0.06	65.47 ± 0.08
	s	0.49	0.56	0.79	0.97	1.22	0.23	4.53
	min	2.0 ± 0.5	2.7 ± 0.5	6.6 ± 0.5	21.8 ± 0.5	22.0 ± 0.5	0.8 ± 0.5	56.6 ± 0.5
	max	4.6 ± 0.5	5.5 ± 0.5	10.7 ± 0.5	26.9 ± 0.5	28.2 ± 0.5	2.1 ± 0.5	77.2 ± 0.5
t value		-0.613	-0.052	1.055	2.635	2.584	1.589	3.122
p value		0.541	0.959	0.295	0.010	0.012	0.116	0.003
Men	mean				24.54 ± 0.08	25.45 ± 0.08		67.49 ± 0.11
	s				0.98	1.09		4.85
	min				22.4 ± 0.5	23.8 ± 0.5		60.0 ± 0.5
	max				26.9 ± 0.5	28.2 ± 0.5		77.2 ± 0.5
Women	mean				23.99 ± 0.08	24.77 ± 0.08		63.45 ± 0.11
	s				0.88	1.26		3.16
	min				21.8 ± 0.5	22.0 ± 0.5		56.6 ± 0.5
	max				25.7 ± 0.5	27.6 ± 0.5		68.9 ± 0.5

Table 2-2. Statistical summary of optic nerve length measurement parameters

		M <sub>2</sub> mm	M <sub>3</sub> mm	M <sub>4</sub> mm
Total	mean	4.97 ± 0.06	3.61 ± 0.06	28.67 ± 0.07
	s	0.89	0.44	3.03
	min	3.2 ± 0.5	2.5 ± 0.5	22.7 ± 0.7
	max	7.0 ± 0.5	4.9 ± 0.5	37.8 ± 0.7
t value		3.760	2.034	5.412
p value		<0.001	0.045	<0.001
Men	mean	5.32 ± 0.08	3.71 ± 0.08	30.25 ± 0.10
	s	1.01	0.45	3.07
	min	3.2 ± 0.5	2.6 ± 0.5	24.3 ± 0.8
	max	7.0 ± 0.5	4.9 ± 0.5	37.8 ± 0.7
Women	mean	4.63 ± 0.08	3.51 ± 0.08	27.10 ± 0.09
	s	0.58	0.42	2.03
	min	3.7 ± 0.5	2.5 ± 0.5	22.7 ± 0.7
	max	6.0 ± 0.5	4.7 ± 0.5	30.7 ± 0.5

Table 2-3. Regression coefficients, number of samples, and  $R^2$  value for Gaussian probability density function for gender-independent measurement parameters

	$M_a$	$M_b$	$M_c$	$M_f$	$M_1$
a	25.25	24.06	26.84	28.15	23.94
b	0.51	0.61	0.75	0.21	8.89
$x_0$	3.19	3.82	8.26	1.18	-1.93
N	80	80	80	80	80
$R^2$	0.98	0.99	0.98	0.97	0.96

Table 2-4. Regression coefficients, number of samples, and  $R^2$  value for Gaussian probability density function for gender-dependent measurement parameters

		$M_d$	$M_e$	$M_g$	$M_2$	$M_3$	$M_4$
Men	a	20.46	16.13	10.41	15.98	16.32	15.95
	b	0.71	1.11	4.61	1.03	0.44	3.04
	$x_0$	24.46	25.35	67.17	5.45	3.66	30.05
	N	40	40	20	40	40	40
	$R^2$	0.97	0.97	0.97	0.91	0.99	0.99
Women	a	15.19	15.97	9.61	15.97	18.73	15.27
	b	0.94	1.26	3.38	0.58	0.34	2.26
	$x_0$	23.95	24.70	62.63	4.54	3.43	27.04
	N	40	40	20	40	40	40
	$R^2$	0.99	0.96	0.95	0.99	0.98	0.96

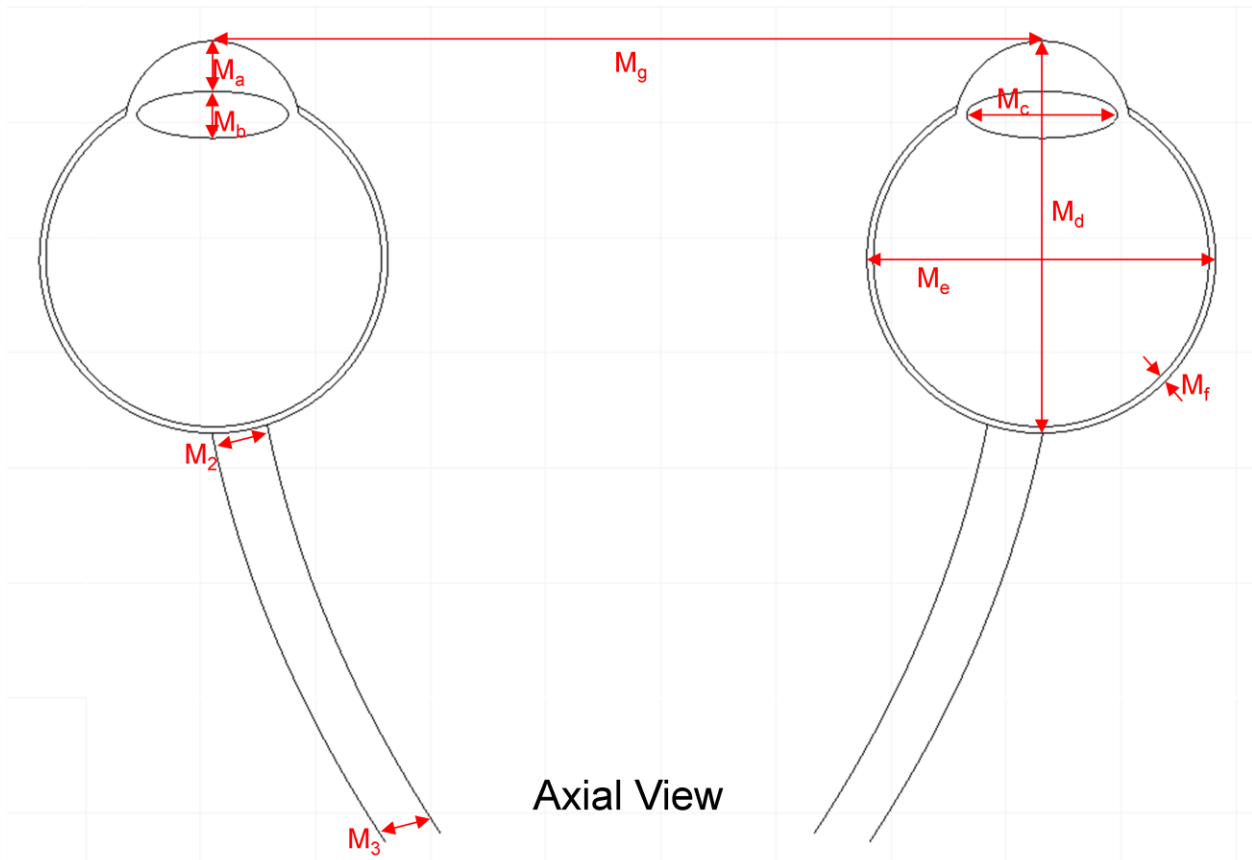


Figure 2-1. Schematic of an axial cross-section of a pair of eyes (not to scale), indicating those anatomic parameters obtained via measurement within a single CT image slice

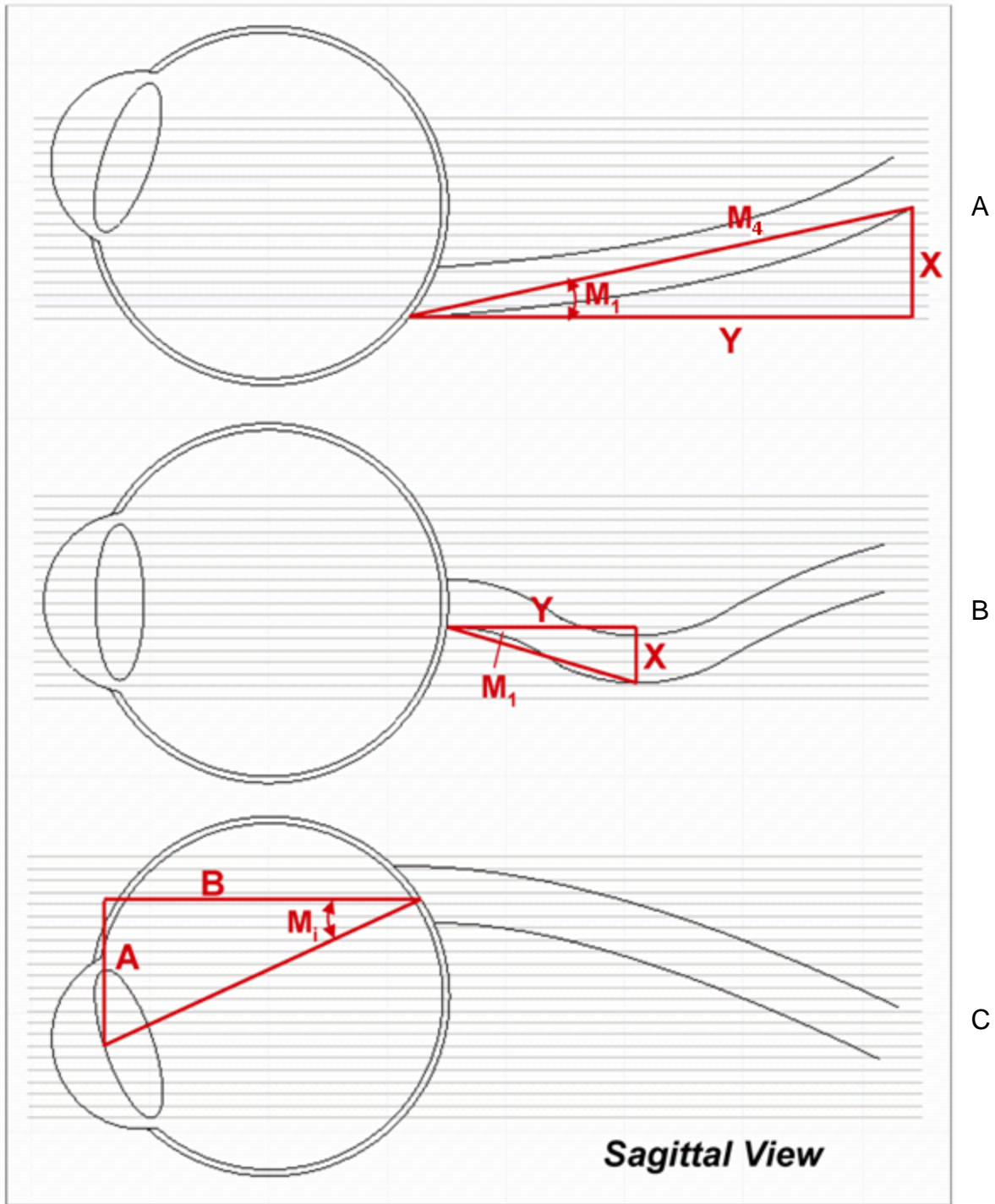


Figure 2-2. Schematic of a sagittal cross-section of an eye (not to scale), indicating those anatomic parameters obtained via measurement within multiple CT images (A) superior gaze (B) primary gaze (C) inferior gaze

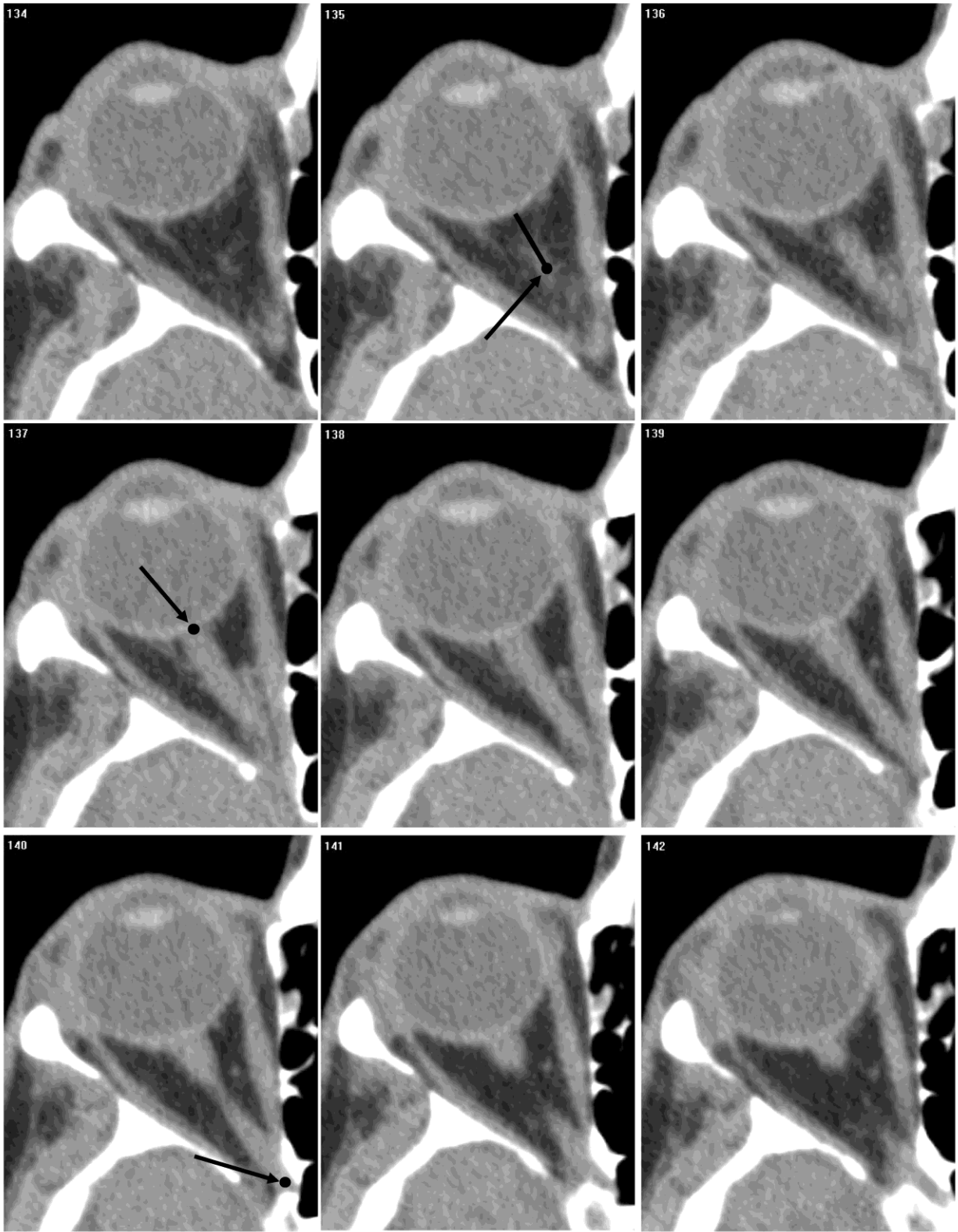


Figure 2-3. CT images of the right orbit of male subject A; slice progression from 134 to 142 is inferior to superior

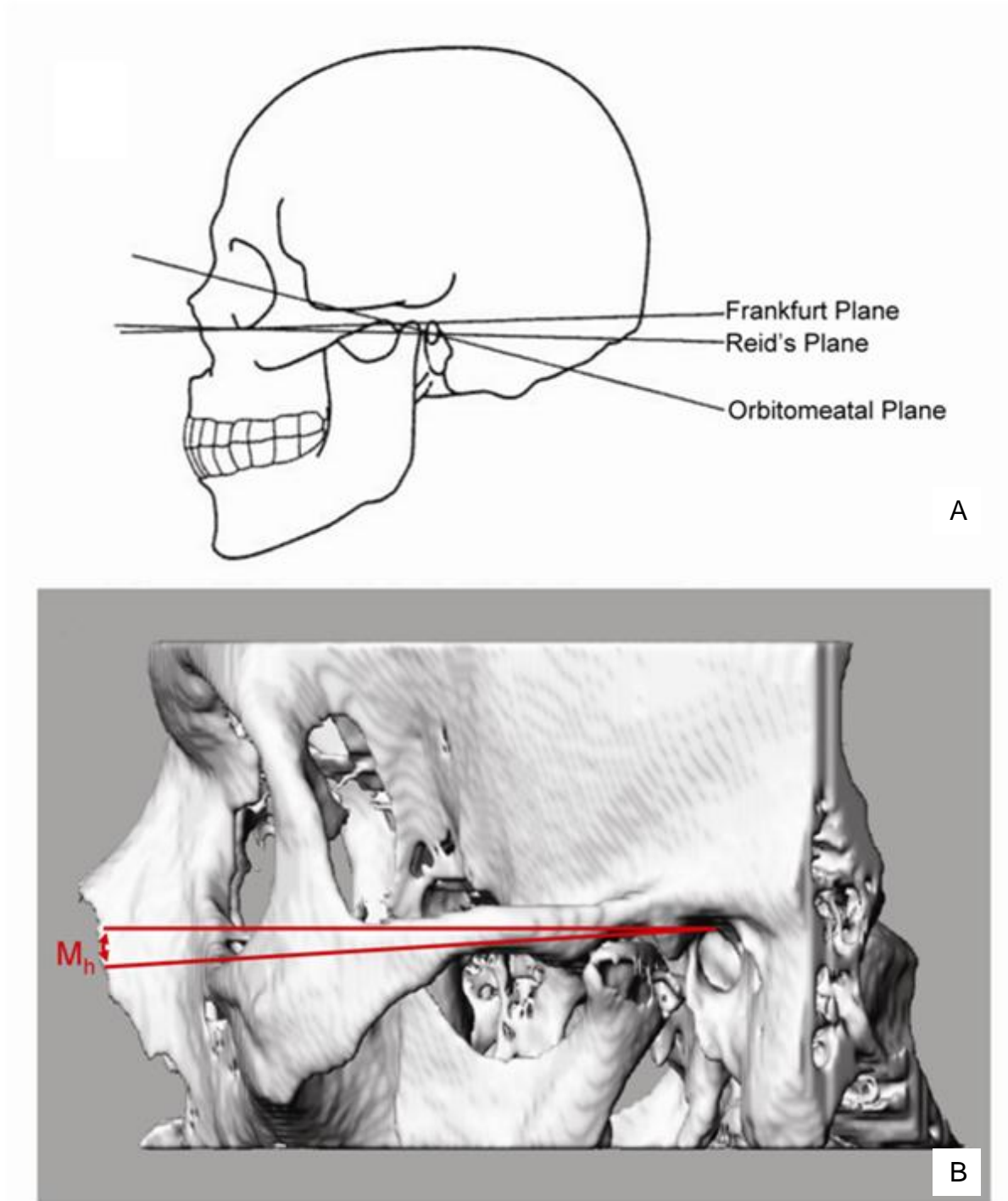


Figure 2-4. Schematic of the Frankfurt plane and normalization parameter (A) common reference planes in the head (adapted from Anthony<sup>38</sup>) (B) 3D reconstructed polygon mesh model of the skull demonstrating measurement of head tilt with respect to the scanning plane

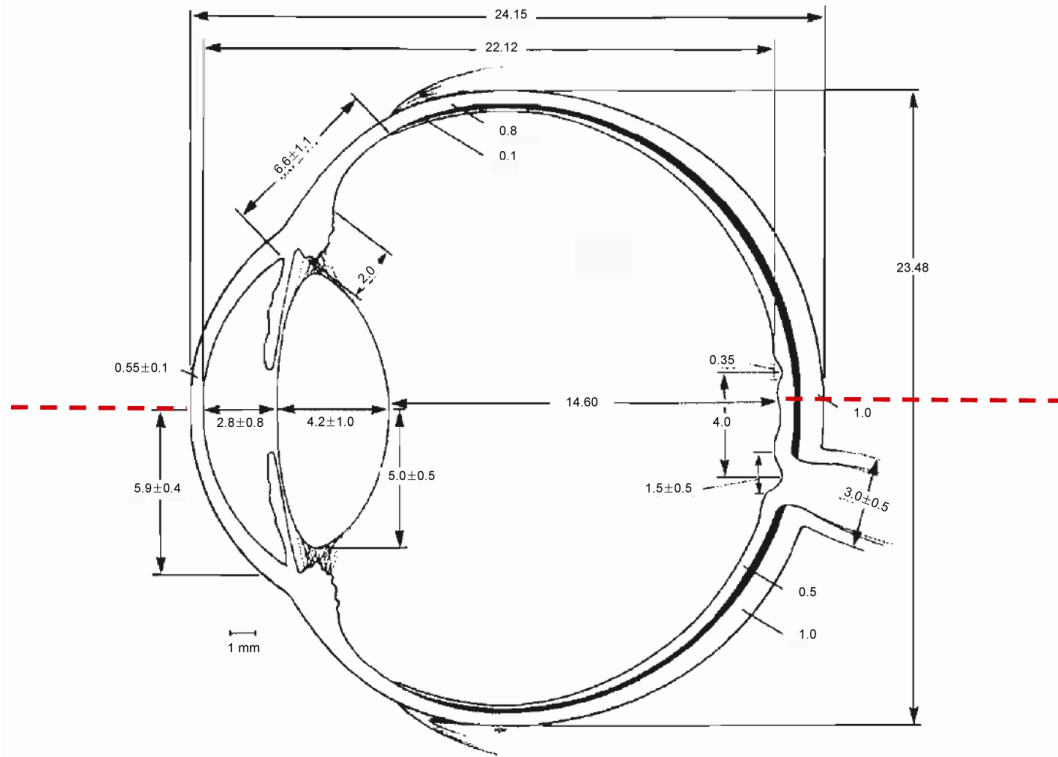


Figure 2-5. Dimensions and locations of tissue structures within the human eye as provided in NCRP Report No. 130; the geometric axis is indicated by the red dashed line; all dimensions are in mm

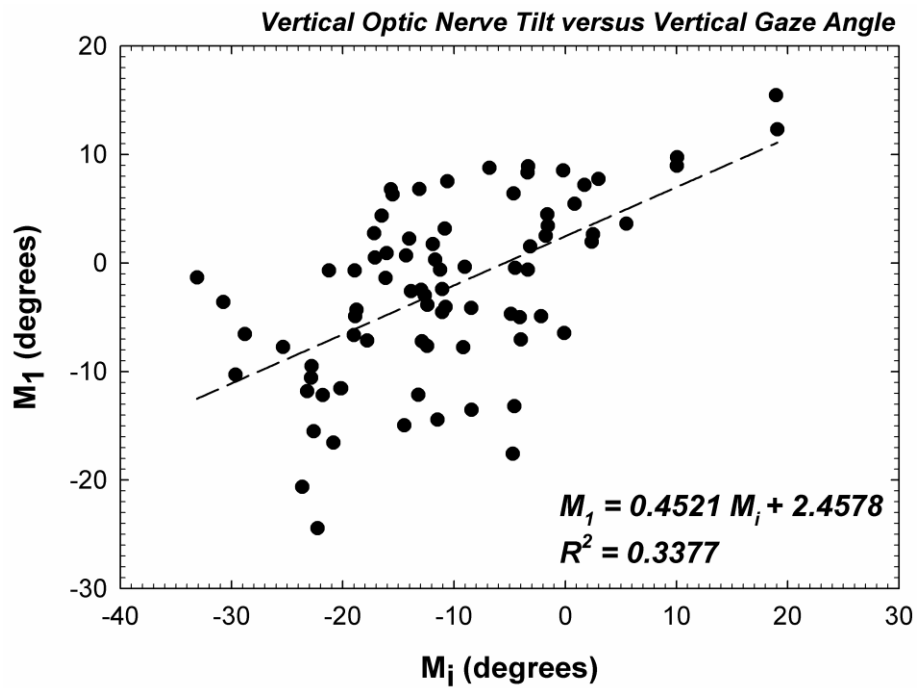


Figure 2-6. Correlation scatter plot for parameter  $M_1$  versus parameter  $M_i$

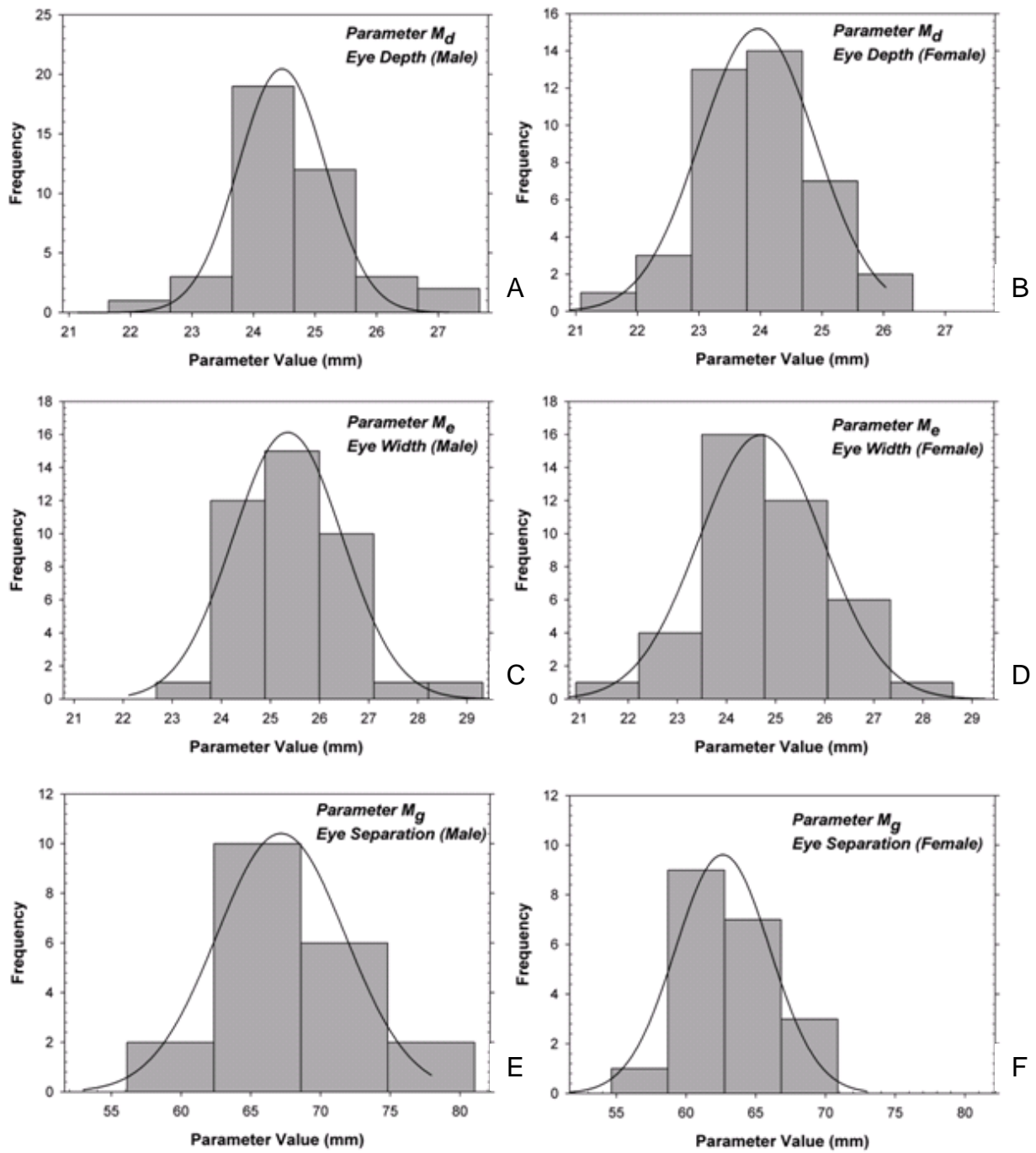


Figure 2-7. Histograms for gender-dependent ocular measurements: (A, B) eye depth, (C, D) eye width, and (E, F) eye separation for males and females, respectively

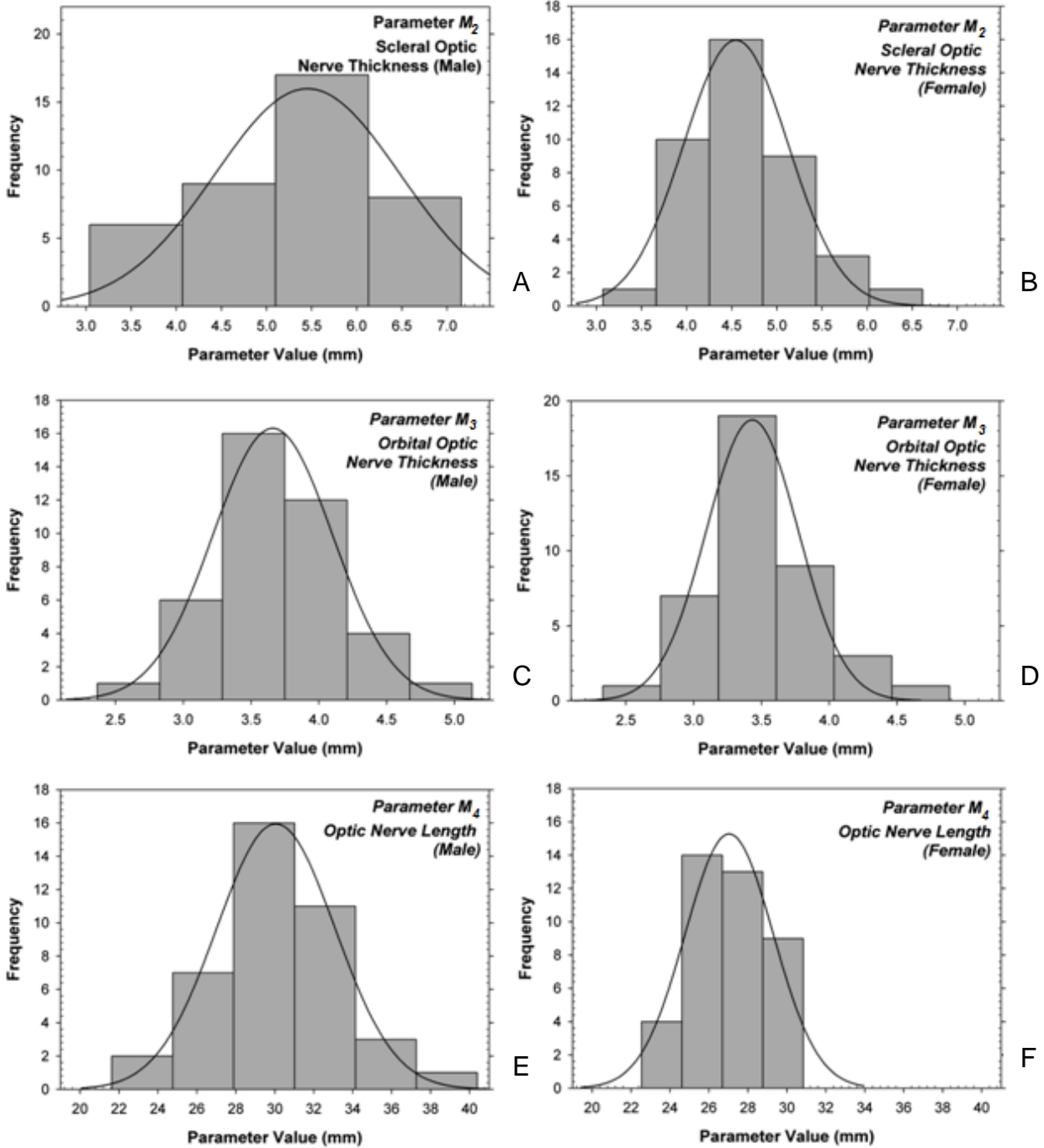


Figure 2-8. Histograms for gender-dependent optic nerve measurements: (A,B) optic nerve thickness at sclera (C,D) optic nerve thickness at orbit, and (E,F) optic nerve length, for males and females, respectively

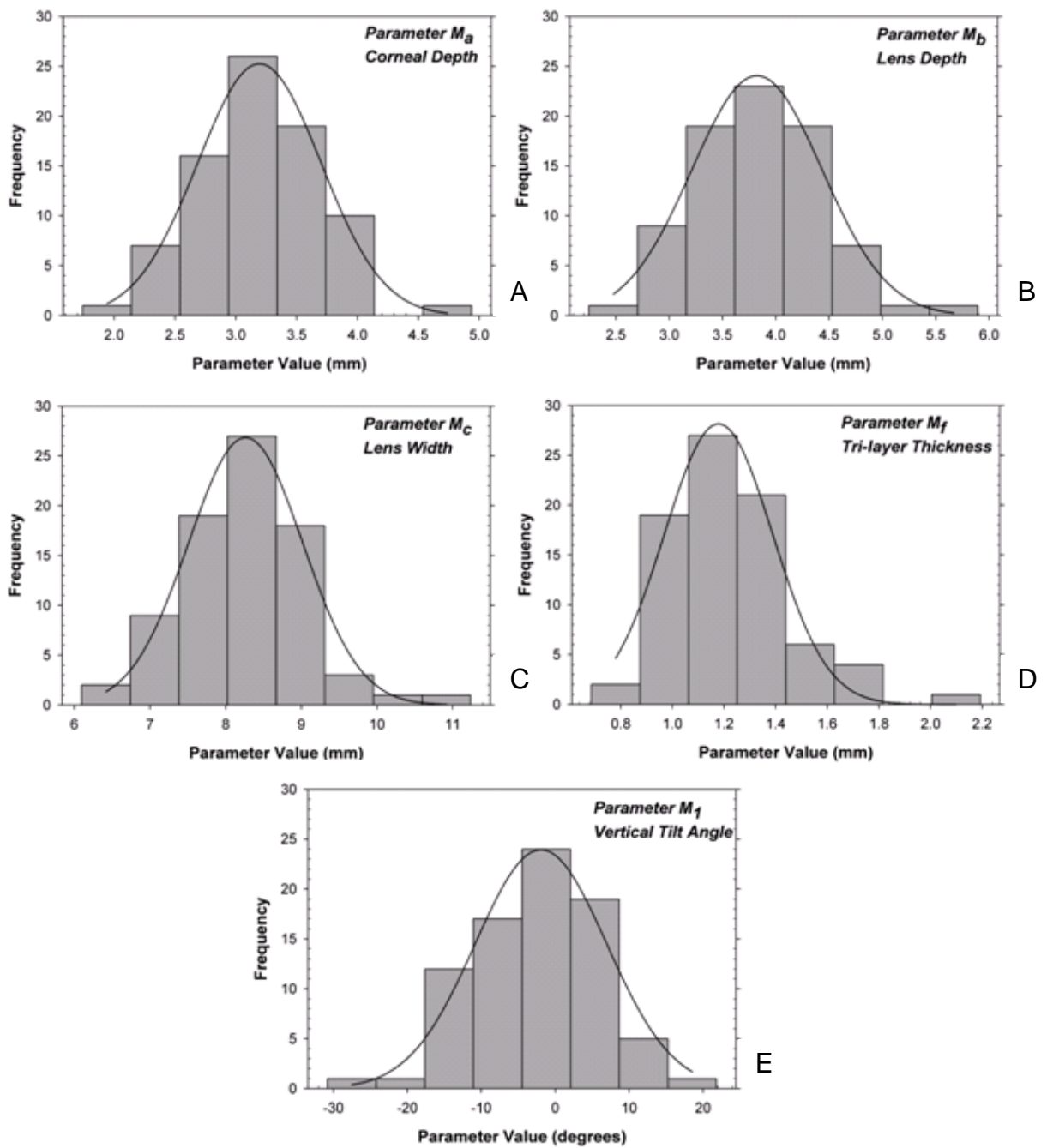


Figure 2-9. Histograms for gender-independent measurements: (A) corneal depth, (B) lens depth, (C) lens width, (D) combined scleral, choroidal, and retinal layer thickness, and (E) vertical optic nerve tilt angle

## CHAPTER 3 ANTHROPOMETRIC PHANTOMS EMPLOYED

### 3.1 History of Computational Phantoms

While the human body's response to ionizing radiation is well documented in literature, direct measurement of absorbed dose in living tissue is not possible. One of the most powerful techniques used to estimate organ doses is through the use of Monte Carlo radiation transport codes with computation anthropometric phantoms, which generally consist of three types: (1) stylized phantoms described by 3D geometric surface equations, (2) voxel phantoms defined by a set of voxels segmented from medical images, and (3) hybrid phantoms constructed from NURBS surfaces.<sup>39</sup>

The Medical Internal Radiation Dose (MIRD) phantom was the first stylized phantom introduced in 1969, but only included three tissue regions (bone, lung, and soft tissue).<sup>40</sup> The evolution of stylized phantoms advanced to include several age groups and match data from International Commission on Radiation Units (ICRU) Publication 23<sup>41</sup> with the construction of the Oak Ridge National Laboratory (ORNL) phantoms in 1980.<sup>42</sup> Stylized phantoms have several advantages such as smooth organ surfaces and flexibility, but are limited to basic geometric shapes such as quadrilaterals, ellipsoids, cylinders, and spheres. Thus, the phantom world evolved to better model the complex and intricate nature of human anatomy through the development of voxel model phantoms.

Voxel phantoms are generated through the contouring of tissues in medical images. The data from these two-dimensional images are stacked to create a three-dimensional matrix of tissue types. This technique is commonly known as *segmenting* and allows for much more detailed modeling of human anatomy than stylized phantoms

can offer. Several independent groups have generated voxel models; however they are not useful for universal distribution because they are not easily deformable and therefore cannot be directly matched to reference values without more complex model manipulation. As such, voxel models are mostly limited to patient specific anatomy. Additionally, surfaces described by voxel geometry are not smooth because voxel models are created from the compilation of many small rigid shapes (usually cubes), and a “stair” artifact is observed near the edge of each tissue. Therefore, the quality of a voxel phantom relies heavily on its voxel resolution, but high resolutions lead to long computer run times during radiation transport.

The third type of computational phantoms devised, hybrid phantoms, attempt to combine the best features of each of the previous two types. The use of non-uniform rational B-spline surfaces (NURBS) allows for a more complex mathematic model of organ surfaces than stylized phantoms can offer.<sup>39</sup> NURBS-based surfaces are defined from a series of control points that can be altered independently for non-uniform scaling and the construction of more complex geometries. A major disadvantage of hybrid phantoms is that they cannot be used directly with radiation transport codes and require a process known as *voxelization*. Thus, for dosimetry purposes, the end result of the hybrid phantom is a voxel model, but with the advantage of having scaled tissue volumes to a desired reference percentile and a user defined voxel resolution. The complete process of voxelization is described subsequently in section 3.4.

### **3.2 UF NURBS Hybrid Reference Models**

Formulation of a male and female whole-body reference phantom was completed within the *Advanced Laboratory for Radiation Dosimetry Studies* (ALRADS) research group at the University of Florida previously (Figure 3-1). The phantoms were

constructed from (1) segmentation of patient CT images using 3D Doctor™ which allows the regions of interest in axial CT slices to be highlighted, and (2) modification of the resulting model to match ICRP Publication 89 50<sup>th</sup> percentile dimensions. Following these general procedures, the skeleton, body contour, major organs and tissues were segmented from the patient CT data and imported into Rhinoceros 4.0™ for conversion to NURBS surfaces. The detailed methodology of the entire process has been given previously by the ALRADS research group.<sup>39, 43</sup>

### **3.2.1 Head Model Detail**

Two head phantoms, male and female, were extracted from the full body models to be used for kilovoltage stereotactic radiosurgery simulation and are shown in Figure 3-2. As noted above, two versions of hybrid phantoms exist: (1) the NURBS phantom constructed from CT image segmentation and volumetrically adjusted to match individual reference tissue volumes and (2) its voxelized counterpart. Table 3-1 gives the final tissue masses for both the hybrid-NURBS and hybrid-voxel adult male head phantoms voxelized at 1 mm x 1 mm x 1 mm resolution. Percent differences from ICRP 89 reference values are indicated along with the ICRP 89 targeted tissue mass and reference densities as given in ICRU Report 46.<sup>44</sup> Corresponding comparisons for the UF hybrid female head phantom are shown in Table 3-2. Several tissues are not of dosimetric concern in this study, but are shown for completeness. Masses for the esophagus and spinal cord are indicated as partial masses (fractional volume contained within the head phantoms). In general, targeted masses are achieved within 1-2% of reference values for both genders.

### 3.2.2 Ocular Model Detail

The eyes have a combined reference mass of 15 g and a combined volume of 14.56 cm<sup>3</sup>, and the lenses have a combined reference mass of 0.5 g and a combined reference volume of 0.42 cm<sup>3</sup>.<sup>29</sup> ICRP Publication 89 only gives reference mass and density for the lens and total eye structure, so additional ocular detail was added based on dimensions given in NCRP Report No. 130. However, the dimensions used in NCRP Report No. 130 are not fully compatible with ICRP Publication 89 reference values, and so the dimensions used to design this model were modified slightly to ensure consistency with ICRP data. The NURBS eye model with dimensions is shown in Figures 3-3.

Anatomically, the macula is a region of the retina surrounding the fovea. Its small size does not permit its direct segmentation in CT images, and thus it must be computationally modeled as a separate structure for dosimetry purposes. In this study, the macula was modeled as a cylinder 4 mm in diameter and 0.5 mm in thickness (retinal thickness from NCRP 130 as given in Figure 2-5). The macula is placed within the posterior region of the eye and translated according to the fovea offset described in section 1.3.2. The cylinder is rotated to align with the curvature of the eye. Coronal and axial views of the fovea shift are depicted in Figure 3-4A and 3-4B, respectively. In the coronal view, the red crosshairs depict where the geometric axis would intersect the posterior pole of the eye. As shown in this figure, the macula has been moved 1.25 mm laterally and 0.5 mm inferiorly so that the center of the macula aligns with the fovea. The center of the optic disc is located 3.3 mm from the geometric axis and 4.6 mm from the center of the fovea. The axial view highlights the necessity to rotate the macula with respect to the curvature of the eye. The optic disc is modeled as a cylinder protruding

into the vitreous humor from the end of the optic nerve, consistent with typical ocular anatomy. The ocular models so described were applied to both the reference male and female head phantoms.

### **3.2.3 Optic Nerve Model Detail**

Due to the absence of available data, the optic nerve measurement parameters described in Chapter 2 were used to design the reference optic nerve models. The mean of the length measurements (parameters  $M_2$ ,  $M_3$ , and  $M_4$ ) and the ranges of the optic nerve tilt measurements ( $M_1$  and estimation of horizontal tilt) were used to provide representative optic nerve models. Based on analysis presented in Chapter 2, the length measurements of the optic nerve were gender-dependent and as such separate models were created for both the male and female. With the IRay<sup>TM</sup> system, targeting error due to patient motion is monitored and maintained below 400  $\mu\text{m}$  on the retina. Therefore, the gaze angle of the patient was not taken into account while building these models, which is the primary reason the standard deviations of the optic nerve tilt parameters are larger than would be seen in a real patient population undergoing AMD radiotherapy (where the gaze angle is fixed with the I-Guide<sup>TM</sup>). As a result, no deviation from primary gaze was assumed during treatment simulation of the reference geometry. However, the use of several optic nerve models, using the full range of optic nerve tilts observed in Chapter 2, will inherently include variation of gaze angle.

The primary optic nerve was fashioned from the means of the measurements, while the other four were formulated from the combination of extreme exit angles in the inferior-superior direction (value of  $M_1$ ) and the medial-lateral direction (estimated from 2D images). For both male and female, the resulting values used in construction of the

optic nerves were -24.4 to +15.5 in the inferior-superior direction and were +18.9 to +28.5 in the medial-lateral direction. The five optic nerve models are labeled as 'mean', 'sup-med', 'sup-lat', 'inf-med', and 'inf-lat' referring to the combination of exit angles used for each. The male set of optic nerve models is displayed in Figure 3-5. While creating these extreme cases for optic nerve exit angle, two control points were maintained within head models: (1) the junction of the eye and optic nerve, and (2) the point at the posterior region of the orbit where the optic nerve enters the cranium. With these two points fixed, another point was needed to measure the exit angle, and so a plane was placed behind the eye and perpendicular to the geometric axis. The plane was placed at a distance equal to the mean of Y in Figure 2-2B, which was 14.3 mm for males and 9.6 mm for females.

### **3.3 Patient Specific Phantoms**

#### **3.3.1 Selection and Development**

Utilizing the CT data obtained as described in section 2.2, 16 image sets were selected for three-dimensional reconstruction. The selection criterion was based on the initial estimates of vertical gaze angle from measurements taken on the axial CT images (parameter  $M_1$ ). Ten patients were found to have a vertical gaze angle within  $5^\circ$  of being parallel to the Frankfurt plane and additional patients were selected in increments of  $5^\circ$  when available, resulting in six additional patients.

Complete three-dimensional reconstruction of the 16 patients was accomplished similarly to the method used to construct the full body reference phantoms. The following anatomical structures of interest were highlighted within the CT head images: the lens, globe of the eye, optic nerve (from the posterior of the globe to the optic foramen), brain, orbital bone, and skin (Figure 3-6). The top and back of the head are

often left out of the field-of-view (FOV) in 1 mm head CT scans, and so only the anterior portions of the brain and skull near the orbit were segmented. This resulted in a model consisting of a small band of tissue surround the ocular anatomy. The resulting polygon mesh files, an example of which is shown in Figure 3-7A, were exported to Rhinoceros 4.0™ to prepare each eye for Monte-Carlo based treatment simulation. The patient specific phantoms constructed were not converted to NURBS surfaces, and as such cannot be accurately described as hybrid phantoms. Rather, these phantoms are classified as voxel phantoms.

### **3.3.2 Expanded (3D) Angular Measurements**

An alternate model with an expanded band of segmentation, an example of which is shown in Figure 3-7B, was also exported to Rhinoceros 4.0™ to re-evaluate vertical gaze angle measurements in 3D and measure optic nerve exit tilt in 3D. Analysis in Chapter 2 provided initial data on vertical optic nerve tilt normalized to the Frankfurt plane, however estimates of horizontal gaze could not be normalized and right-left head tilt was not factored into analysis. Thus, a three-dimensional evaluation of optic nerve tilt and gaze is warranted. The 3D angular positioning measurement parameters are denoted as: ( $\Theta$ ) tilt angle of the optic nerve as it leaves the posterior region of the eye and ( $\Phi$ ) gaze angle. Gaze direction was defined as the line that intersects the volume centroids of the eye and lens. A sagittal reference plane was defined by: (1) a point on the septum in the anterior lobe of the brain, (2) the midpoint of the ear canals, and (3) being perpendicular to the Frankfurt plane, which was again used for the axial reference plane. Both parameters were measured relative to the reference planes and partitioned into vertical and horizontal components. The parameters will be referred to as  $\Theta_v$  and  $\Phi_v$  for the vertical component and  $\Theta_h$  and  $\Phi_h$  for the horizontal component.

Scatter plots and linear regression equations are shown for the measured vertical and horizontal components of the angular measurement parameters  $\Theta$  and  $\Phi$  in Figure 3-8 along with total (angle measured in 3D environment) angular measurements. The parameters from a linear regression indicate that the reference position of the optic nerve is tilted  $0.8^\circ$  superiorly and  $22.4^\circ$  medially.

As in Chapter 2, the results suggest a loose correlation between the gaze angle and optic nerve position. As gaze angle shifts, the optic nerve reacts accordingly by being “stretched” in the opposite direction. Thus, for an upward vertical gaze, the optic nerve would have a superiorly tilted exit angle, and for a downward vertical gaze it would have an inferiorly tilted exit angle. For an inward (medial) horizontal gaze, the optic nerve would increase the degree of tilt in the medial direction from its reference position, which is already tilted approximately  $22.4^\circ$  in the medial direction. For an outward (lateral) horizontal gaze, the optic nerve will reposition itself with a smaller tilt angle with respect to its reference position in the medial direction. The  $R^2$  values are again well below what would be characterized as a statistically significant correlation, indicating that not all optic nerves have the same reference position and may react differently to changes in gaze angle. Additionally, for the optic nerve to be able to react to changing gaze, there must be some “slack” in the optic nerve in the reference or primary gaze position. The position in which this slack comes to rest may depend on the last direction that person gazed, or the person’s head orientation with respect to gravity if sufficient time is allowed for the optic nerve to readjust itself within the orbital fat. Furthermore, it may seem counterintuitive that the distribution of horizontal gaze angles is centered over a negative value, favoring a lateral gaze. However, in this

study, gaze angle was defined using the volume centroids of the lens and globe (geometric axis) which is not coincident with the fovea (visual axis). Since the fovea is located lateral to the posterior pole, which intersects the geometric axis, defining true gaze angles using the visual axis would shift the distribution medially. In this scenario, the true gaze would be dependent on the distance to the object of focus, which has no relevance in the clinic for treatment planning.

### **3.3.3 Patient Specific Treatment Planning**

After angular measurements were evaluated, each of the 32 eyes (left and right done separately) was prepared for computational treatment simulation using the Rhinoceros 4.0™ software. This was accomplished by: (1) locating the center of the optic disc (approximated from the three-dimensionally reconstructed optic nerve), (2) determining the position of the posterior pole (3.3 mm lateral to optic disc center), (3) determining the position of the fovea (1.25 mm lateral and 0.5 mm inferior to the posterior pole), (4) locating the apex of the cornea from the three-dimensionally reconstructed globe, (5) aligning the treatment axis to intersect the fovea and to be parallel with the geometric axis, which is defined as the intersection of the posterior pole and the apex of cornea, (6) insertion of cylinder with 4 mm diameter and 0.5 mm thickness coincident with the fovea representing the macula tissue, and (7) tagging each structure with a tissue name for voxelization.

An important aspect about this method for treatment simulation should be noted here. The position of each eye model was left as segmented to preserve the anatomy observed directly from the CT data and was not rotated into a gaze position clinically realistic of the stereotactic radiosurgery treatment. A range of clinically realistic vertical gaze angles was determined from the analysis of 25 healthy volunteers whose vertical

gaze was measured with their heads situated in the IRay™ head support device (unpublished data). The gender distribution was 15 male and 10 female. The vertical gaze of the individual in the IRay™ system is dependent primarily on anatomical factors, though there is one mechanical degree of freedom that contributes to the vertical gaze angle: the chin rest can be moved anterior-posterior by 25 mm. To control for this flexibility, the vertical gaze angles were determined at the two extremes of chin rest position. Vertical gaze angle was measured from the Frankfurt plane to be consistent with the computational measurements. During treatment, the patient's eye is constrained to gaze 7° below the horizon, and the posts that hold the head rest of the IRay™ stand normal to patient gaze, at 7° from vertical. Image analysis was used to determine how a subject's Frankfurt plane sits in the head rest with respect to the post. With the chin rest set all the way forward, a subject's head was set in the head rest, and a high resolution image was taken normal to the subject's profile capturing the auditory canal, the head rest post, and the eye and cheek. A similar image was taken with the chin rest set all the way back. For the purpose of this measurement, the eye is allowed to roam freely as the direction of the gaze during treatment is constrained to be perpendicular to the post. A line representing the Frankfurt plane was drawn from the top of the auditory canal to the infraorbital rim, based on the folds of the skin, using the *ImageJ* software. A second line was drawn intersecting the first line, parallel to the head rest post. The angle between the Frankfurt line and the post line was measured, from which the vertical gaze angle could be determined.

Clinically, the horizontal gaze angles are small as the patient head is placed in the system looking forward, and the eye is held forward as well. If the head were seated at

an angle in the head restraint, the clinician would re-seat the patient for placement of the eye restraint.

The clinically relevant vertical gaze angles determined from 25 healthy volunteers ranged from  $1.7^{\circ}$  inferior to  $17.3^{\circ}$  superior with respect to the Frankfurt plane. A reasonable estimate for the range of clinically realistic horizontal gaze angles is within  $5^{\circ}$  of the primary gaze position, which is defined as a straight-ahead gaze.

### **3.4 Voxelization**

As mentioned in the description of hybrid phantoms, voxelization is required for use in conjunction with radiation transport. To accomplish this, each organ in the NURBS models were tagged in Rhinoceros 4.0™ and then exported in *raw* format. Using an in-house MATLAB code, *Voxelizer 6.0*, the models were voxelized to a desired resolution in a binary file. Using another in-house MATLAB code, the binary files were converted to lattice file format, which is readable by MCNPX.

When selecting voxel resolution, there is a tradeoff between accurately modeling small structures (higher voxel resolution) and efficient computer run times during radiation transport simulation (lower voxel resolution). To account for this tradeoff, three versions of the UF NURBS reference phantom were selected and voxelized at different resolutions. The torso of the reference phantom, to be used in the calculation of effective dose from leakage radiation, was voxelized to 2 mm x 2 mm x 2 mm resolution. The extracted head model was voxelized to a resolution of 1 mm x 1 mm x 1 mm; however, the limiting size of the macula (0.5 mm in thickness) determines the resolution necessary for accurate ocular anatomy. Consequently, a finer resolution ocular model was begot from voxelizing the full NURBS head model to 0.5 mm x 0.5 mm x 0.5 mm resolution. The finer resolution head model was carefully cropped to

include the entire optic nerve and anterior portions of the brain for the treated right eye using the *ImageJ* software (NIH, Bethesda, MD). Similarly, all of the patient specific models were cropped and voxelized to a 0.5 mm x 0.5 mm x 0.5 mm resolution. The voxelized versions of the reference head and eye models are shown in Figure 3-9 and 3-10, respectively, and a two-dimensional cross section of a patient specific voxel model is shown in Figure 3-11.

Table 3-1. Comparison of tissue masses in the UF hybrid NURBS and voxel male head phantoms with those given in ICRP Publication 89 for the reference adult male

Organ System	Density (g/cm <sup>3</sup> )	ICRP 89 mass (g)	UFH - NURBS mass (g)	% Diff	UFH - Voxel mass (g)	% Diff
Eye Structures						
Eyes (2)	1.03	15	14.946	-0.4%	14.843	-1.0%
Lens (2)	1.07	0.45	0.450	0.1%	0.447	0.7%
Macula (2)	1.03		0.013		0.015	
Optic discs (2)	1.04		0.002		0.004	
Optic Nerves (2)	1.04		1.055		1.058	
Respiratory System						
ET1 (anterior nasal layer)	1.03		2.202		2.062	
ET2 (posterior nasal layer)	1.03		13.717		8.582	
ET2 (oral cavity layer)	1.03		1.370		1.477	
ET2 (larynx)	1.07	28	28.125	0.4%	27.917	-0.3%
ET2 (pharynx)	1.03		3.944		3.394	
Alimentary System						
Tongue	1.05	73	73.158	0.2%	72.119	-1.2%
Salivary glands	1.03	85	85.077	0.1%	84.636	-0.4%
Parotid	1.03	50	50.047	0.1%	49.672	-0.7%
Submaxillary	1.03	25	25.028	0.1%	24.975	-0.1%
Sublingual	1.03	10	10.002	0.0%	9.989	-0.1%
Tonsils	1.03	3	3.016	0.5%	2.980	-0.7%
Esophagus (partial)	1.03		8.814		8.792	
Skeletal System						
Cranium	1.38		919.433		905.192	
Mandible	1.38		81.439		81.479	
Vertebrae-C	1.38		148.638		147.657	
Intervertebral Discs	1.10		5.563		3.478	
Additional Tissues						
Brain	1.04	1450.00	1449.641	0.0%	1434.722	-1.1%
Ears	1.10		14.879		14.874	
External nose	1.05		12.985		12.892	
Pituitary Gland	1.03	0.6	0.602	0.3%	0.600	0.1%
Spinal Cord (partial)	1.04		42.333		38.057	
Thyroid	1.05	20	19.956	-0.2%	19.906	-0.5%

Table 3-2. Comparison of tissue masses in the UF hybrid NURBS and voxel female head phantoms with those given in ICRP Publication 89 for the reference adult female

Organ System	Density (g/cm <sup>3</sup> )	ICRP 89 mass (g)	UFH - NURBS mass (g)	% Diff	UFH - Voxel mass (g)	% Diff
<b>Eye Structures</b>						
Eyes (2)	1.02	15	14.801	-1.3%	14.718	-1.9%
Lens (2)	1.07	0.45	0.450	0.1%	0.442	-1.8%
Macula (2)	1.03		0.013		0.022	
Optic discs (2)	1.04		0.002		0.001	
Optic Nerves (2)	1.04		0.784		0.770	
<b>Respiratory System</b>						
ET1 (anterior nasal layer)	1.07		0.642		0.639	
ET2 (posterior nasal layer)	1.02		9.776		9.073	
ET2 (oral cavity layer)	1.02		1.145		3.486	
ET2 (larynx)	1.07	19	18.999	0.0%	18.728	-1.4%
ET2 (pharynx)	1.02		1.549		1.321	
<b>Alimentary System</b>						
Tongue	1.05	60	59.997	0.0%	59.765	-0.4%
Salivary glands	1.02	70	70.061	0.1%	69.839	-0.2%
Parotid	1.02	41	41.085	0.2%	40.985	0.0%
Submaxillary	1.02	21	20.970	-0.1%	20.867	-0.6%
Sublingual	1.02	8	8.006	0.1%	7.988	-0.2%
Tonsils	1.02	3	2.998	-0.1%	2.963	-1.2%
Esophagus (partial)	1.03		8.244		8.261	
<b>Skeletal System</b>						
Cranium	1.38		799.001		790.616	
Mandible	1.38		62.452		62.515	
Vertebrae-C	1.38		110.662		110.561	
Intervertebral Discs	1.10		4.675		3.737	
<b>Additional Tissues</b>						
Brain	1.04	1300	1302.777	0.2%	1287.817	-0.9%
Ears	1.10		9.200		9.178	
External nose	1.05		16.063		16.638	
Pituitary Gland	1.02	0.6	0.601	0.1%	0.606	1.0%
Spinal Cord (partial)	1.04		11.454		11.972	
Thyroid	1.05	17	16.998	0.0%	16.981	-0.1%

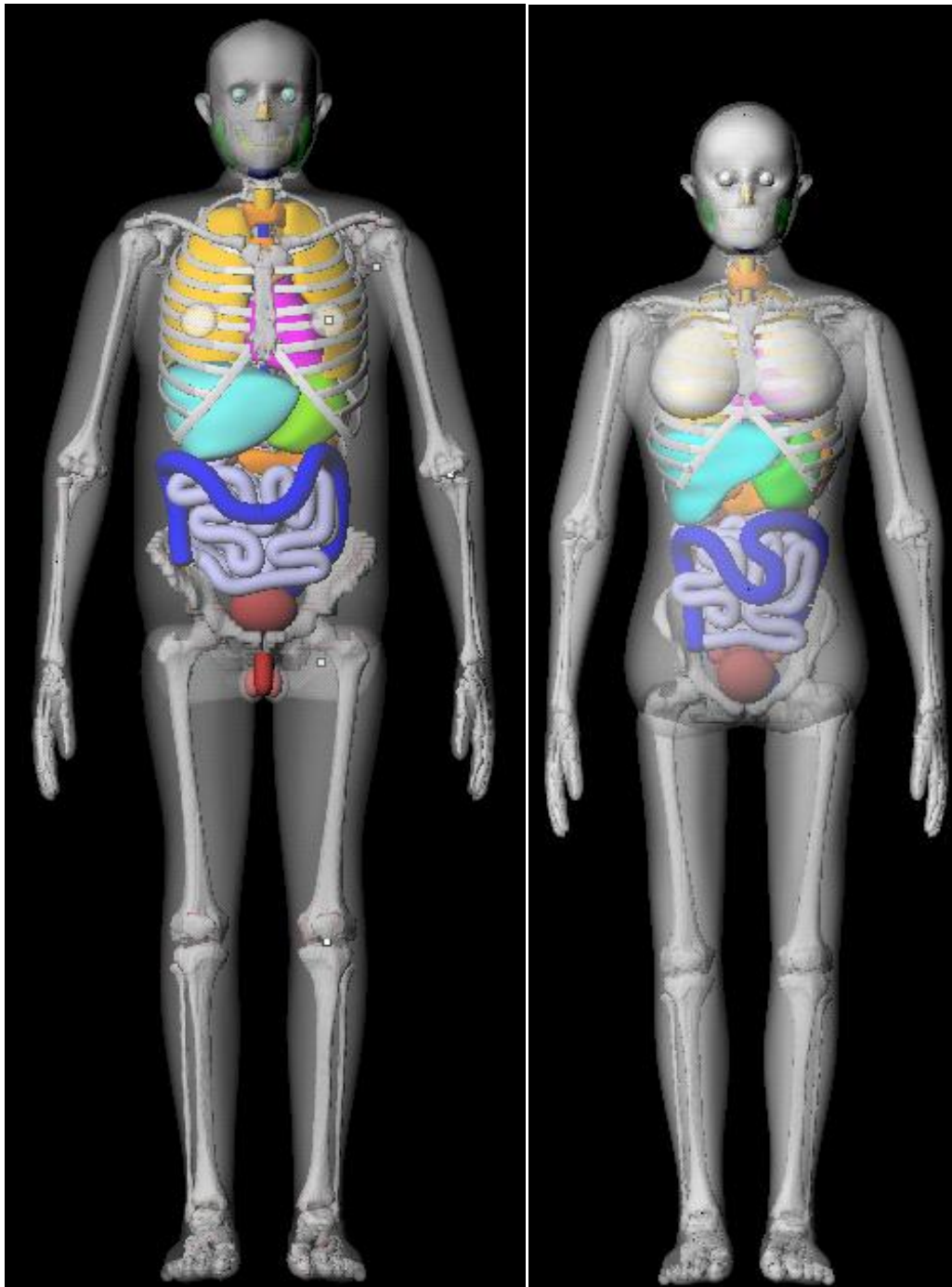


Figure 3-1. The whole body male (left) and female (right) reference phantoms developed within the Advanced Laboratory for Radiological Dosimetry Studies

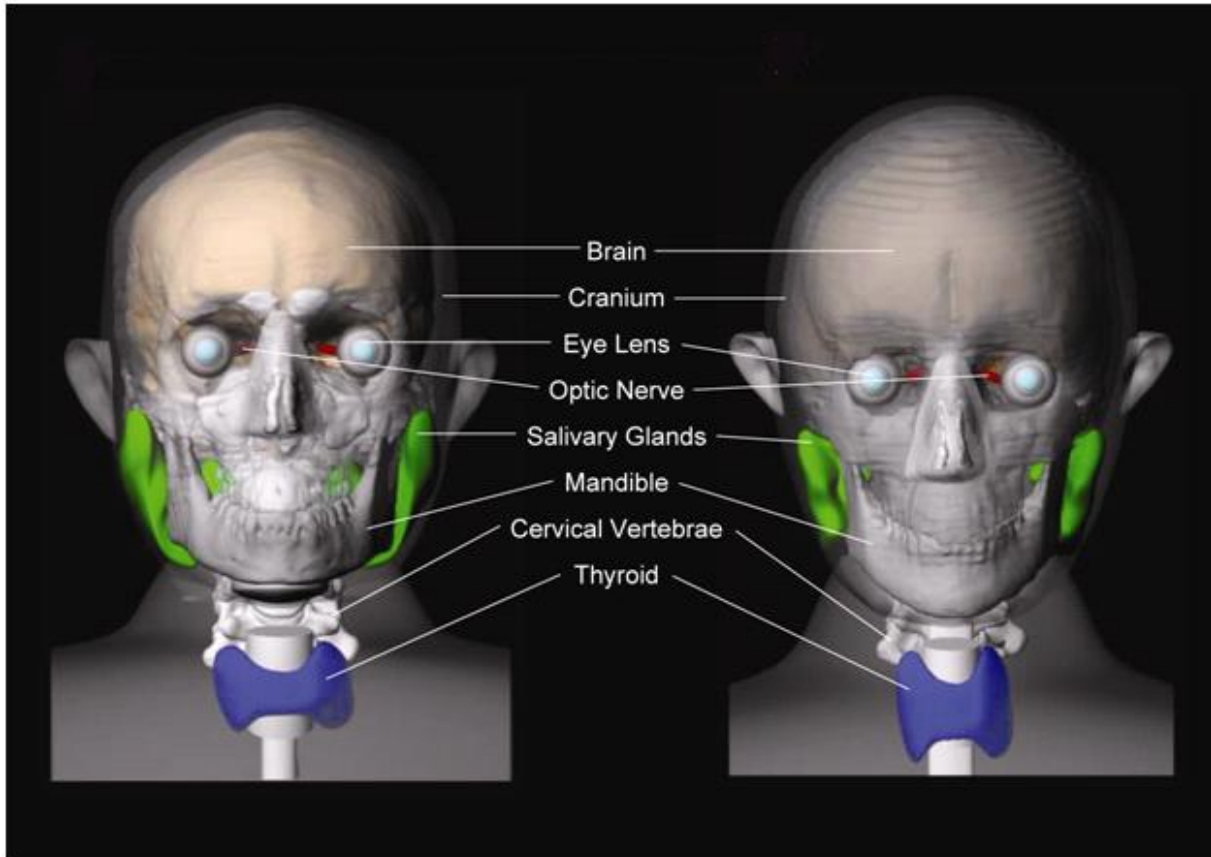


Figure 3-2. University of Florida NURBS male (left) and female (right) head models based on organ masses listed in ICRP Publication 89

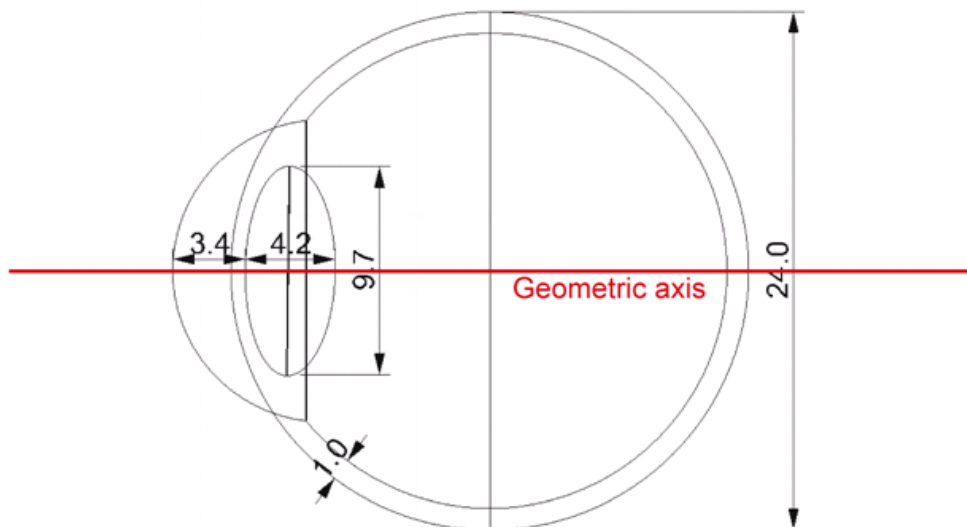


Figure 3-3. Dimensions of the tissues structures in the NURBS eye model; all dimensions are in mm

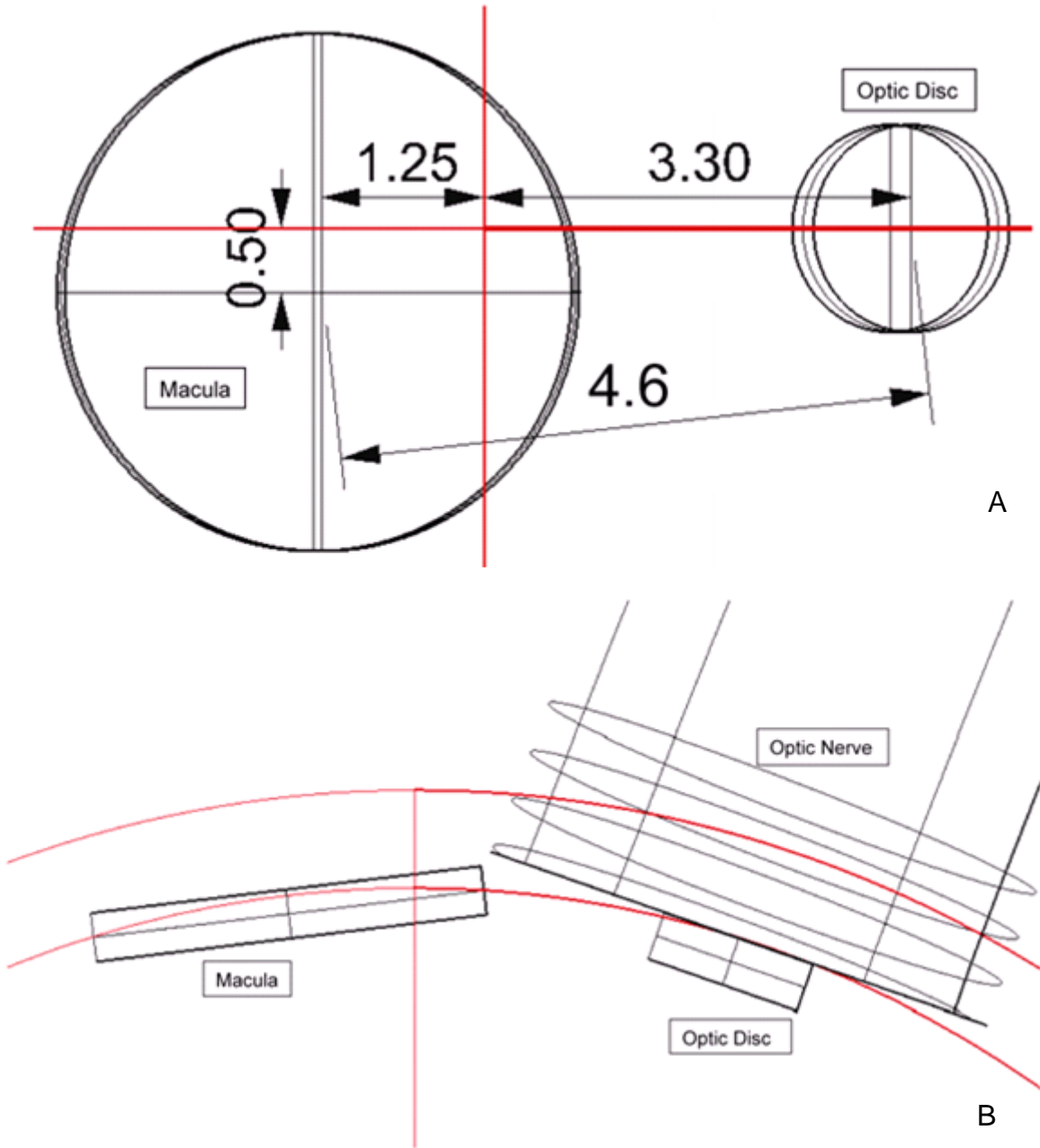


Figure 3-4. Engineering drawings of the eye detail embedded within the reference NURBS head model; (A) coronal view of the posterior region of the right eye demonstrating the fovea offset with the posterior pole located at the intersection of the red lines; all dimensional are in mm (B) axial view of the poster region of the right eye demonstrating the position and rotation of the macula with the geometric axis defined by the red line extending towards the anterior portion of the eye

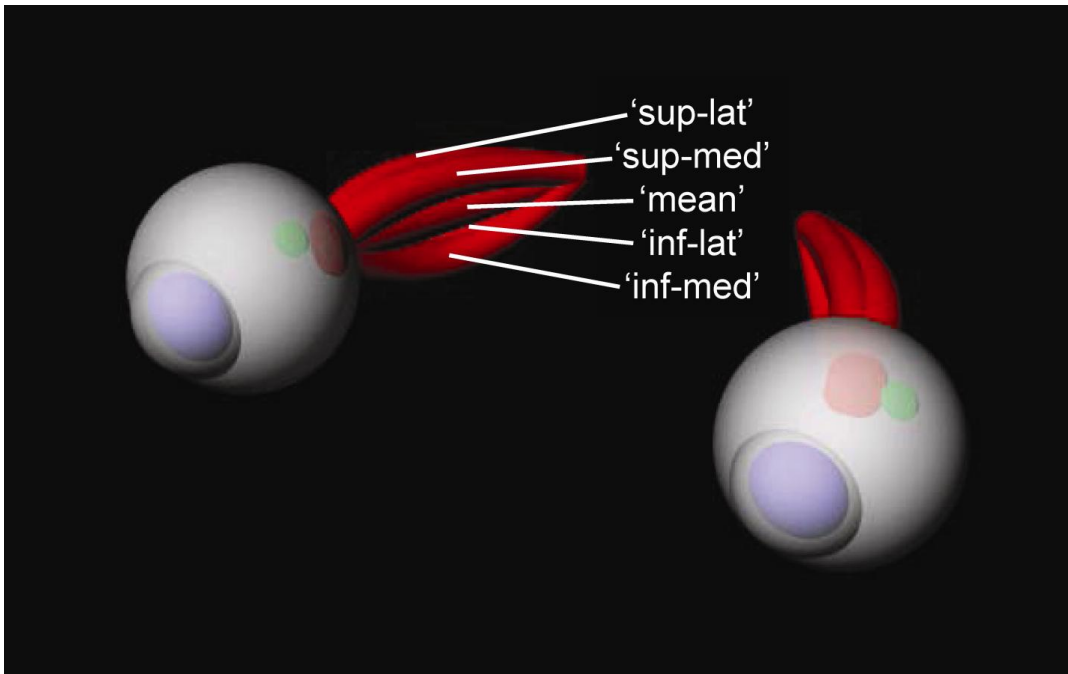


Figure 3-5. Male NURBS eye models with five optic nerve variations (red), the macula targets (green), and the lenses (blue)

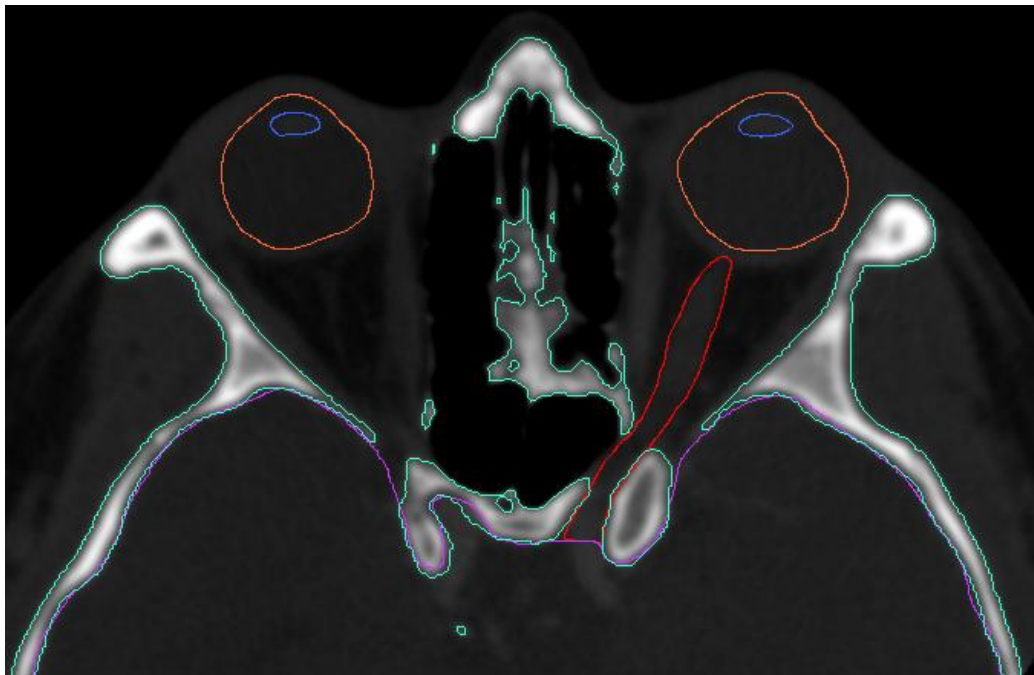


Figure 3-6. Segmentation of the lens (blue), globe (orange), optic nerve (red), brain (purple), and skull (teal) from a 1 mm axial CT image of the orbital region

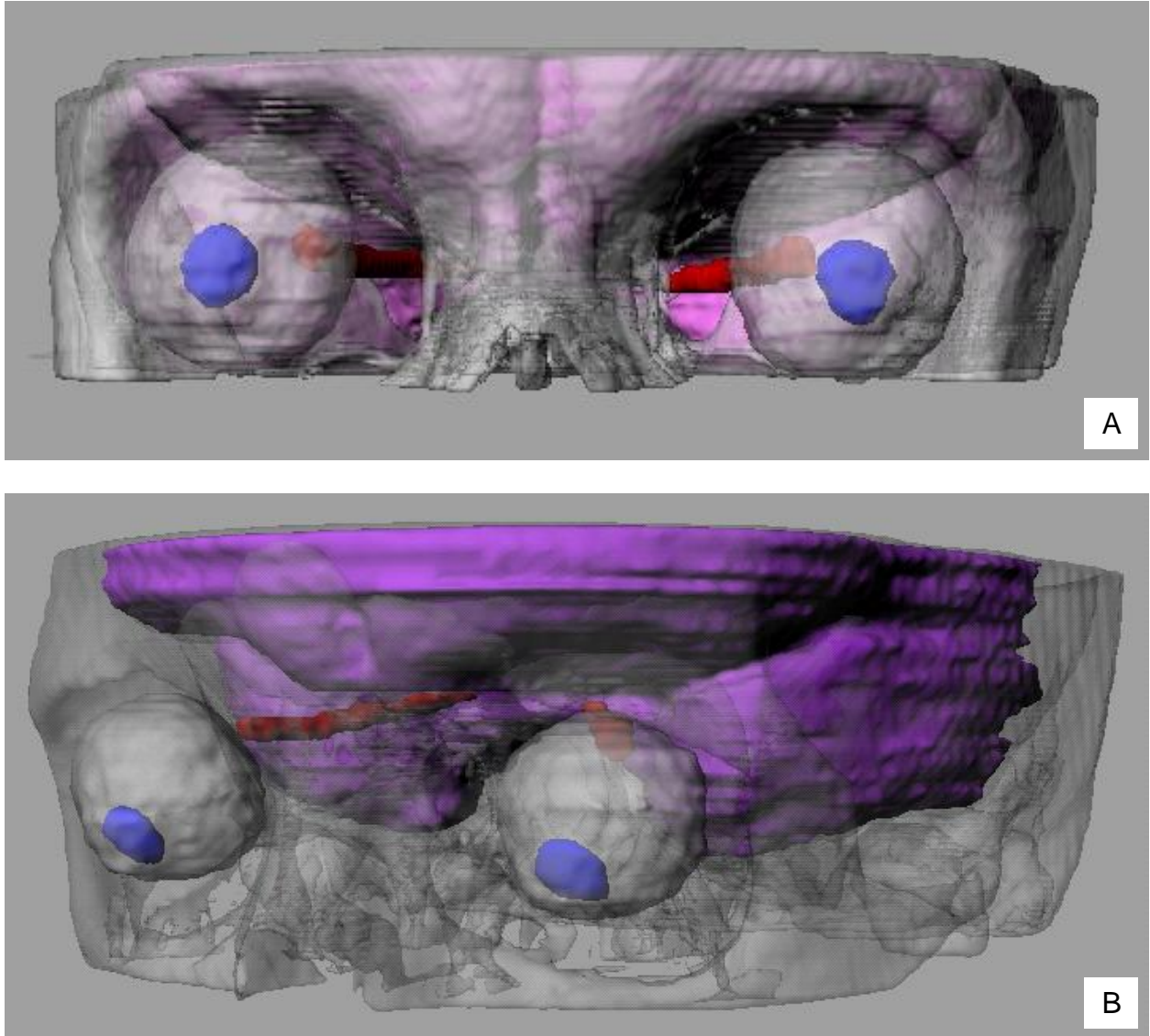


Figure 3-7. Patient specific models in object file format generated from three-dimensional reconstruction of 1 mm CT data (shown without skin); (A) typical size of model to be submitted for 0.5 mm<sup>3</sup> voxelization, and (B) expanded model that includes both the bottom of the orbit and the ear canals so that the Frankfurt plane can be defined for evaluation of 3D measurement parameters

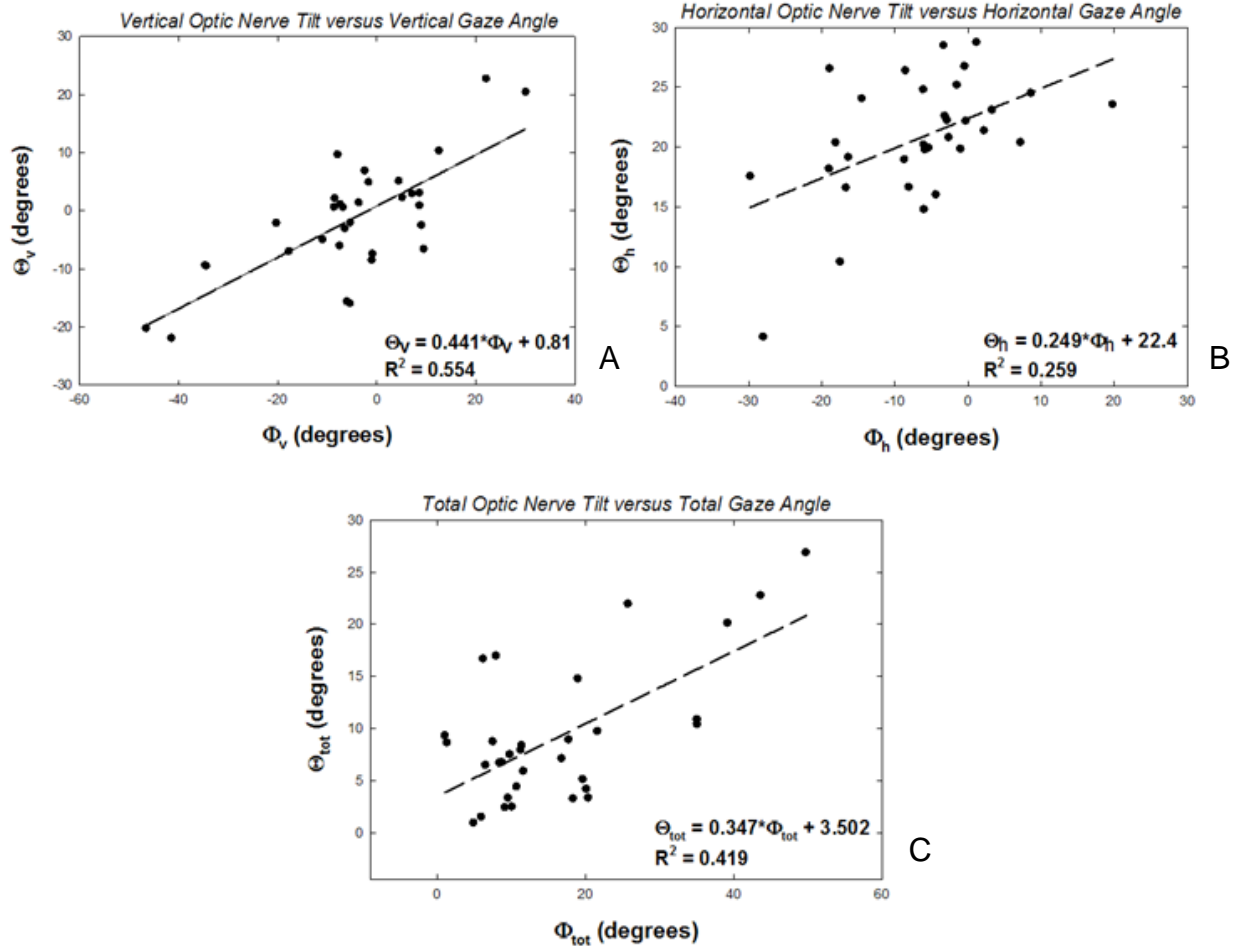


Figure 3-8. Scatter plots of optic nerve tilt as a function of gaze angle; linear regressions determine the reference positions of the optic nerve (y-axis intercept), and the resulting parameters are shown within the plots; (A) vertical components: values positive in the superior direction and negative in the inferior direction (B) horizontal components: values positive in the medial direction and negative in the lateral direction (C) total: all values positive as they were obtained in 3D



Figure 3-9. Coronal (left) and sagittal (right) views of the head model voxelized to  $1 \text{ mm}^3$  resolution

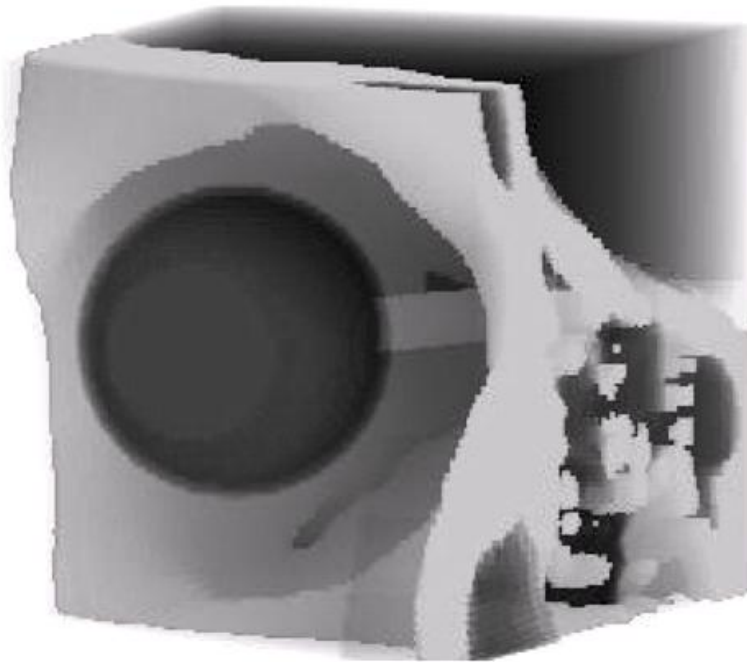


Figure 3-10. Cropped eye section voxelized to  $0.5 \text{ mm}^3$  resolution

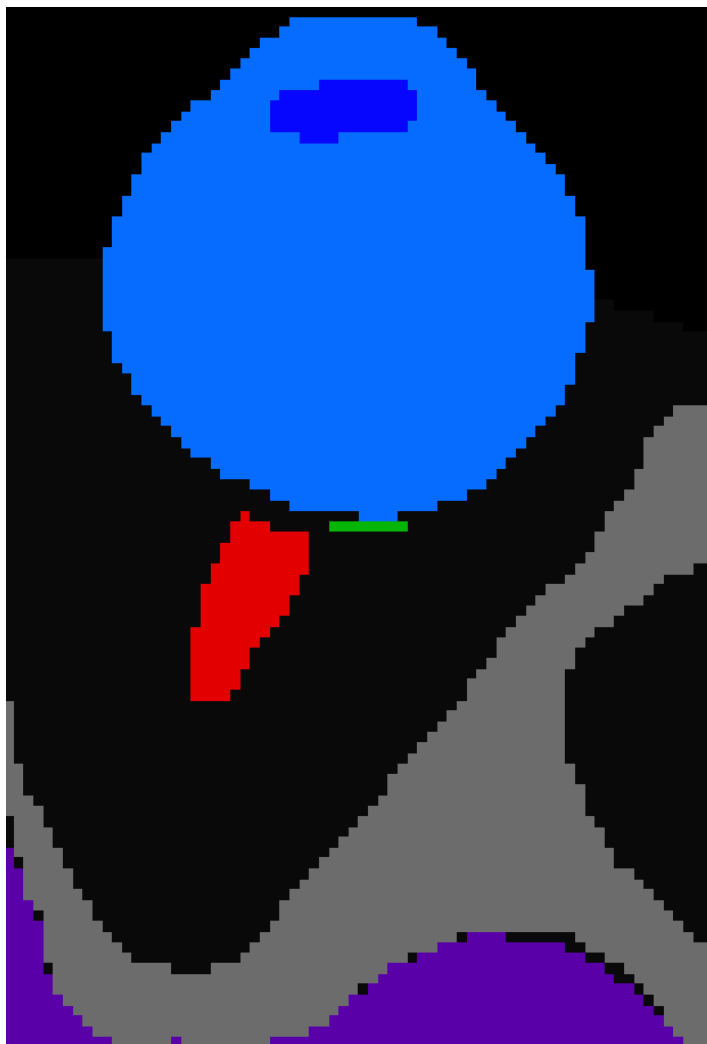


Figure 3-11. Axial cross sectional view of a patient specific model voxelized to  $0.5 \text{ mm}^3$  resolution

## CHAPTER 4 COMPUTATIONAL METHODS

### 4.1 The Monte Carlo Radiation Transport Code MCNPX

Monte Carlo methods use random number generation and probability statistics to solve a variety of physics based mathematical problems. By running a large number of histories (samples of particle tracks), the stochastic (random) behavior of nuclear particles is averaged and macroscopic trends can be observed. The physics model underlying Monte Carlo techniques break down over very small distances (e.g. sub millimeter for electrons), but provides an excellent method to simulate radiation transport on a larger scale. This is an invaluable tool, essentially allowing radiation-based experiments to take place within the safety of computer algorithms. Each particle is tracked to the end of its life (or until it reaches the problem boundary) and each individual physical event (scattering, absorption, etc) is determined by a probability distribution function defined within the nuclear cross section libraries that are stored within the radiation transport code.

MCNPX (Monte Carlo N-Particle eXtended) is a general purpose Monte Carlo radiation transport code written in Fortran 90 that tracks a variety of radiation particles over broad energy ranges.<sup>45</sup> MCNPX began as an extension of MCNP4B in 1994 and was developed by Los Alamos National Laboratory (LANL, Los Alamos, NM). The extended version provides an improvement on physics simulation models, extension of neutron, proton, and photon libraries to higher energies, addition of new particle types, and the formation of new tally techniques. The developers of the code are so confident in its ability to model radiation physics that they promise a \$2 bill for any error found

within the code. Therefore, all simulations of ocular radiotherapy for AMD presented within this study were performed using the MCNPX version 2.5.0.

The structure of the MCNPX code is divided into three sections and a title card. The first two sections, the cell and surface cards, describe the problem geometry. Cells are defined by surfaces using Boolean operators and contain information about the material density. The last section, the data cards, contains information that defines the material composition explicitly, the source definition, and the tally specification. A few other cards are often given in the data card section; some are mandatory (mode and nps cards) but many are optional and allow the user to modify the default settings, such as energy cutoff and energy grouping methods.<sup>45</sup>

## **4.2 Monte Carlo Techniques Used for Treatment Modeling**

An example input deck is given in Appendix A featuring the ‘mean’ optic nerve model within the 0.5 mm x 0.5 mm x 0.5 mm resolution male eye section of the reference phantom.

### **4.2.1 Cell and Surface Cards**

Voxel model geometry was used for all input files in this work, which requires the assignment of universe numbers to each cell within a lattice based on tissue type. Two surface cards are necessary for such a geometry definition (besides the outer boundary of the problem): (1) an rpp box defining the overall dimension of the lattice structure, and (2) an rpp box defining the dimensions of each voxel. The lattice structure is filled using data from an imported lattice (.lat) file, and the result is a lattice box filled with several universes, each with the dimensions of a single voxel. The cell cards define the properties of each universe: material type, density, volume, and importance. This

method is one of the most powerful ways to import complex geometries into an MCNP input deck. A visual of voxel geometry plotted by MCNPX is given in Figure 4-1.

#### **4.2.2 Source Definition**

The relevant x-ray emission spectrum was generated for a tungsten anode tube operated at 100 kVp with anode angle of 12 degrees and total filtration of 0.75 mm Al and 0.8 mm Be using the computer software described in Report No. 78 of the Institute of Physics and Engineering in Medicine.<sup>46</sup> Using the simulated x-ray energy spectrum, a divergent x-ray beam was modeled as a 1 mm x 1 mm area source representing a 1 mm<sup>2</sup> focal spot. The divergence was modeled to simulate a beam collimated by an explicit tungsten aperture with a beam diameter of 4 mm at the macula target over a source-to-target distance of 150 mm. The nominal polar angle of 30° from the treatment axis was accomplished using a transformation card, as were the three different treatment azimuthal angles: 150°, 180°, and 210°.

Leakage calculation requires a different source definition. The leakage source was defined at a point coincident with the location of the anode. The energy spectrum of leakage radiation is generally characterized as hard, that is, higher energy photons have a greater chance to transverse the tube housing unattenuated and the remaining photons are *harder* to attenuate. The clinical energy spectrum of the leakage radiation is unknown for this medical device; therefore an approximation was made using an 80 and 100 keV mono-energetic source of photons. The dosimetry results from both energies were similar and so the 100 keV source was used for final reporting.

#### **4.2.3 Tally Specification**

In all, there are eight different tally specifications and four mesh tally options in MCNPX. Tally cards can be modified by a number of keywords and other cards,

providing a versatile method for extracting useful data from the problem geometry.

Three ways to tabulate dose were utilized for this project: (1) F4 tally for cell fluence modified by a dose response function with DE/DF cards, (2) F6 tally for energy deposition within a cell, and (3) type 1 mesh tallies using the keyword 'pedep'.

The \*F6 tally was used to calculate all tissue-specific mean absorbed doses in this study. The \*F6 tally in MCNPX reports jerks per gram per photon history. A jerk is an MCNP unit of energy equivalent to  $10^9$  Joules, thus the reported value for each organ tally was multiplied by a coefficient of  $10^{12}$  to convert to Gy per photon history using the FM card. Absorbed doses to the brain, thyroid, salivary glands, bone marrow, and bone surfaces were calculated using the  $1 \times 1 \times 1 \text{ mm}^3$  voxel head model, while doses to the macula, lens, optic disc, and optic nerve were calculated with the  $0.5 \times 0.5 \times 0.5 \text{ mm}^3$  voxel eye model. The  $2 \text{ mm} \times 2 \text{ mm} \times 2 \text{ mm}$  voxel torso model was used to calculate the leakage contribution for several other radiosensitive organs.

The F4 tally was set up for calculation of dose to bone marrow and bone surfaces for the cranium, mandible, and cervical vertebrae. The tally was modified by dose response functions described in ORNL/TM-8381/V1 Table D-5.<sup>42</sup> The MCNPX output for this tally type is in units of photons/cm<sup>2</sup> and the dose response functions convert photon/m<sup>2</sup> to Gy. Therefore, each bone tally was multiplied by a coefficient of  $10^4$  to convert to Gy per photon history.

The type 1 mesh tally with the keyword 'pedep' was coded to exactly overlap the lattice structure of the voxel geometry. MCNPX creates a binary output file in the form of a 3D matrix containing the dose to each voxel. Using the built in GRIDCONV

function in MCNPX, this output file was converted to an ASCII file. This output is necessary to beget dose volume histograms and dose contour maps.

Two other tally types were used in this study to tally photon fluence: (1) an F1 tally modified by an e0 and c0 card to evaluate energy and angular dependence of fluence, and (2) a type 1 mesh tally without any keyword (default is for fluence). An evaluation of the distribution of photons exiting the head during treatment was necessary in determining safety parameters and shielding design for clinical staff present during treatment. An F1 tally sphere, with its origin at the macula target and normal vector aligned with the treatment axis, was used to evaluate the energy and angular dependence of photon fluence at a radius of 0.5 meters. Two-dimensional matrices were implemented using type 1 mesh tallies, flush with the edge of the lattice structure, which were used to characterize the spatial distribution of photons emanating from each side of the model.

#### **4.2.4 Material, Mode, and NPS Cards**

All of the material cards defined in this project were derived from ICRU 46 material composition and density data.

The mode 'p' was used for all input decks for this study. This mode approximates that all secondary particles from interactions (electrons) deposit their energy locally at the site in which it was born (KERMA approximation). This increases computing efficiency by not creating and tracking the secondary electrons. It is a good approximation considering the short track length of secondary electrons in the kilovoltage energy group and was validated by Lee *et al.*<sup>28</sup>

A total of  $10^7$  x-ray photon histories were completed for each simulation, and the resulting statistical errors for tissue-averaged dose tallies were found to be less than 2%

for the optic disc, less than 1% for all other tissues, and ranged from 0.6% to 2% for each macula voxel.

### 4.3 Post Processing

#### 4.3.1 Calculation of Effective Dose

**Contribution from primary tube output.** Effective dose was determined for a 3 x 8 Gy treatment using steps described in International Commission on Radiological Protection (ICRP) Publication 103<sup>47</sup> and the following expression:

$$E = \sum_T w_T \sum_R w_R D_{T,R} = \sum_T w_T \left[ \frac{H_T^M + H_T^F}{2} \right] \quad (4-1)$$

Tissue mean absorbed doses ( $D_{T,R}$ ) are included for the brain, thyroid, salivary glands, active bone marrow, and bone surfaces by scaling the output from section 4.2.3 by the number of histories necessary to deliver an absorbed dose of 8 Gy to the macula for each treatment angle. A  $D_{T,R}$  of 0 was assumed for all radiosensitive organs below the neck. Radiation weighting factors ( $w_R$ ) can be found in Table B.4 of ICRP Publication 103 and are 1.0 for photons. The equivalent dose for tissues in the reference adult male ( $H_T^M$ ) and female ( $H_T^F$ ) for each beam angle were summed to give a cumulative equivalent dose for a 3 x 8 Gy treatment and sex averaged. Tissue weighting factors ( $w_T$ ) are found in Table B.2. of ICRP Publication 103 and are given in Table 4-1. The notation in this section is consistent with that in ICRP Publication 103.

Several other weighting factors were implemented for the calculation of effective dose. The parotid, submaxillary, and sublingual portions of the salivary glands were volume weighted to yield a single tissue dose to the target. The bone surfaces (endosteum) were weighted by fraction of bone surface across the entire skeleton. This tissue weighting was as follows: cranium 15.3%, mandible 0.4%, and cervical vertebrae

2.1% for male and cranium 15.8%, mandible 0.4%, and cervical vertebrae 2.2% for female.<sup>48</sup> The bone marrow dose was weighted by values given in Table 9.4 in ICRP Publication 89 which reports the percentage of active marrow in each bone relative to total body active marrow as a function of age. The maximum age of 40 year was used here since the majority of patients undergoing AMD treatment are over the age of 50.

**Contribution from leakage.** The determination of effective dose from the leakage contribution is a more complex process requiring the energy spectrum of leakage radiation and the dose rate at some distance from the anode. The clinical leakage energy spectrum for the IRay<sup>TM</sup> is unknown; therefore an approximation was made using a mono-energetic source 100 keV photons. A dose rate reading in air near the heart was taken in the clinic, found to be 12 mR/hr, and used as a conversion factor for MCNPX output. To apply the conversion factor, modified input files were generated filling each universe with air, thus modeling and irradiating an air phantom. The output from the dose tally for the cells tagged as heart was converted from jerk per gram per history to rad per history by applying a coefficient of  $10^{14}$ . The leakage rate was multiplied by the treatment time per beam (~2 minutes), and converted from mR to rad giving the total rad per beam in the clinic. The rad per beam was divided by the rad per history from the air phantoms to give a conversion factor based on the total number of source particles necessary to give a dose rate of 12 mR/hr near the heart. The MCNPX inputs were re-run with a tissue filled phantom and the conversion factor was applied to the output for dose of each tissue. The remainder of the effective dose calculation was performed in the same manner as for the primary tube output, but with all organs in the torso considered, and again consistent with ICRP 103.

### **4.3.2 Utilizing Mesh Tally Output**

As mentioned, a mesh tally was coded exactly overlapping the voxel geometry allowing for a unique manipulation of mesh tally output. An in-house MATLAB code was written to link the dose to each voxel from the mesh tally to the original tissue types in the voxel model. This allows the presentation of data in several useful formats including: DVH plots, dose distribution tables, and dose contour maps. The code used is given in Appendix B. DVH plots are created within the MATLAB program and the dose distribution tables are exported to Excel. Further manipulation is necessary to actualize dose contour maps using Microsoft Excel, Sigmaplot 10.0™, and a photo editing software.

Table 4-1. Tissue weighting factors for the calculation of effective dose as given by ICRP 103

Tissue	Number of tissues	$w_T$	Total Contribution
Lung, stomach, colon, bone marrow, breast, remainder	6	0.12	0.72
Gonads	1	0.08	0.08
Thyroid, oesophagus, bladder, liver	4	0.04	0.16
Bone surfaces, skin, brain, salivary glands	4	0.01	0.04

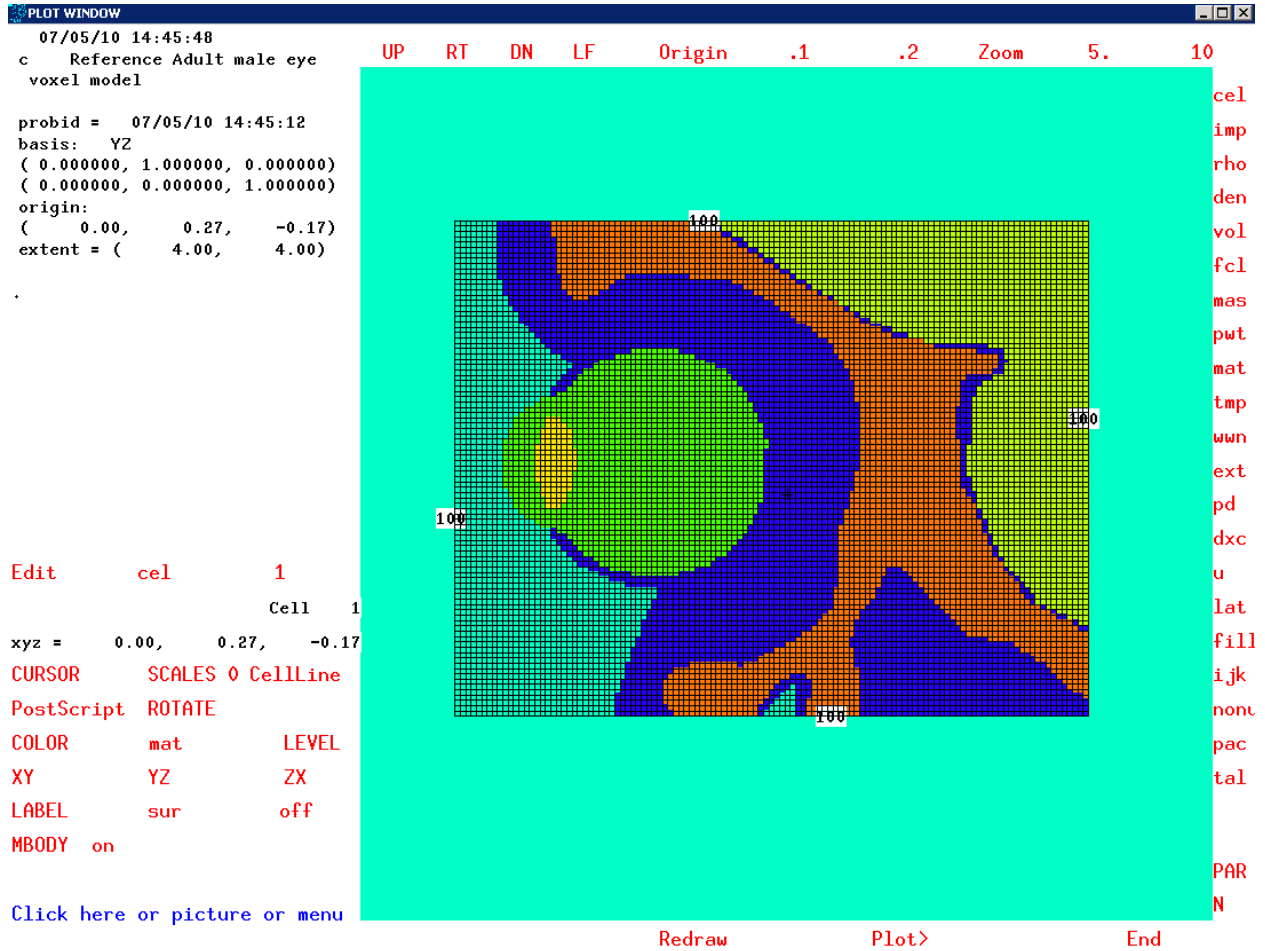


Figure 4-1. MCNPX plot of the male eye section model voxelized to  $0.5 \text{ mm}^3$  resolution

## CHAPTER 5 TREATMENT OUTCOME EVALUATION AND ANALYSIS

### 5.1 Radiation Dose Thresholds for Complications

The biological response of the human eye to ionizing radiation is well documented. A review of the major findings may be found in Section 5 of Report No. 130 of the National Council on Radiation Protection and Measurement (NCRP). Much of the experience on the radiation response of the eye derives from studies with fractionated and chronic regimens of low-LET radiation. The radiation absorbed doses that produce minimally detectable changes or functional disabilities are 6, 5, 30, 15, 16, and 25 Gy, for the lid, conjunctiva, cornea, sclera, iris, and retina, respectively. The corresponding visually debilitating absorbed doses to these same ocular structures are 40, 35, 30, 200, 16, and 25 Gy, respectively.<sup>30</sup>

Until recently, the threshold for minimally detected changes or functional disability to the lens was reported to be 2000 mGy and the threshold for visual debilitation was reported as 5500 mGy.<sup>30</sup> However, more recent studies suggest that the lens is much more sensitive to ionizing radiation than previously thought. A recent report suggests that the tissue-averaged dose threshold for radiation cataractogenesis could be as low as 700 mGy.<sup>49</sup> This limit will be used in this study in the analysis of treatment outcomes to err on the side of greater radiological protection.

The radiological sensitivity of the optic nerve has been studied in patients whose optic nerve was unavoidably or unintentionally irradiated as a consequence of brain or head tumor radiotherapy showing that doses 8 Gy or higher might have some adverse consequence.<sup>50</sup> Another study found that doses less than 12 Gy to a short segment of the anterior optic apparatus during stereotactic radiosurgery resulted in a low risk

(~1.1%) for radiation-induced optic neuropathy (RON); however, 3 of 4 patients in this study that developed RON had previously received external beam radiation therapy (EBRT) and the other had undergone two previous radiosurgery procedures.<sup>51</sup> It is also unclear what percentage of volume characterized the short segment of the anterior optic apparatus. Ultimately, the authors conclude that point doses up to 12 Gy are well tolerated by patients whose optic nerve has not been previously irradiated. Furthermore, a recent study suggest that the optic apparatus may be more tolerant to radiation than previously thought, able to receive up to 14 Gy without risk of developing RON (again under the assumption that the patient has not previously undergone radiation therapy).<sup>52</sup>

Other tissues of interest include the brain and orbital bone. The development of necrosis in brain tissue due to radiological toxicity is summarized by Lawrence *et al*, and it has been determined that the threshold for neurological toxicity is 12 Gy for a volume of at least 5 - 10 cm<sup>3</sup>.<sup>53</sup> Bone, and in this case orbital bone, contains elements with higher atomic numbers that have a higher cross section (probability) for photon interaction, namely the photoelectric effect, than soft tissue and fat. The resulting secondary particles (electrons) are likely to deposit their energy locally and as such the bone absorbs more dose than surrounding tissues. However, the skull is fairly radio-resistant to adverse consequences and the orbital bone contains a negligible percentage of the total active marrow in the cranium.<sup>29</sup>

## **5.2 Reference Model Dose Assessment**

### **5.2.1 Tissue-specific Mean Absorbed Doses**

Mean absorbed doses to several non-targeted tissues are shown in Table 5-1 for a 3 x 8 Gy treatment to the right eye. The MCNPX output has been normalized by the

number of photons necessary to deliver a dose of 8 Gy to the macula target for each beam. The lens received a 3-beam integral mean dose of 124 mGy and 127 mGy in the reference male and female patient, respectively, well below the threshold for cataractogenesis. The optic disc receives a mean dose ranging from 200 to 239 mGy, a factor 33 to 40 times less than that for the macula target, despite its proximity to the macula target (4.6 mm). The average absorbed dose to the optic nerve, a critical part of this project, was found to increase with increasing beam azimuthal angle for the treated right eye. The optic nerve used for calculation in this section was that in the 'mean' position. The highest optic nerve mean dose recorded was 112 mGy in the reference female patient at a  $210^{\circ}$  beam entry angle. Other non-targeted tissue doses were also found to be insignificant. The highest dose to the optic nerve opposite treatment was 2.4 mGy for the female at a  $210^{\circ}$  beam entry. The mean absorbed doses to the brain ranged from 3.0 to 4.9 mGy per treatment beam. The mean absorbed doses to the thyroid and salivary glands were 4 to 5 orders of magnitude less, respectively, than that to the target for all beam angles and both sexes. Considering the mean absorbed doses to the bone structures in the head, the cranium received the highest dose to both the active marrow and endosteal tissues, but these doses were on the order of 9 mGy or less.

### **5.2.2 DVH Analysis**

Dose volume histograms for the male and female *mean* optic nerve model are shown in Figures 5-1 for a cumulative 3 x 8 Gy treatment. These histograms display how the absorbed dose is distributed throughout the structure of the macula, lens, brain, and optic nerve. Ideally the macula histogram would be a step function, but the absorbed dose the macula is not quite evenly distributed, and the plots are thus

designed to show a treatment with a maximum dose of 24 Gy to the target. For both sexes, a steep drop is observed for the lens, indicating that there are no hotspots. The brain DVH also drops off steeply, but small hotspots in the anterior portions of the brain (<10%) contribute doses ranging up to about 2.5 Gy. Nevertheless, for females only about 5% of the brain volume receives a dose exceeding 2.5 Gy and 95% of the male brain receives a dose less than 2 Gy.

The DVH of the 'mean' male optic nerve shows that 2-3% of that structure receives a dose exceeding 2 Gy, and that approximately 1% receives a dose exceeding 5 Gy. Less than 1% of the optic nerve volume receives a dose over 10 Gy with a maximum of about 12 Gy. The DVH of the 'mean' female optic nerve shows that 2-3% of the tissue volume receives more than 1 Gy with less than 1% receiving a maximum dose of 8 Gy. The difference in DVH's for the male and female optic nerve indicate that the maximum dose is a function of optic nerve diameter at the posterior of the eye (value of  $M_2$ ) since the mean of this measurement is 0.7 mm less for females. This correlation will be explored more subsequently.

Due to the lack of literature on quantifying the anatomical location of the optic nerve, and the somewhat large standard deviation of parameter  $M_1$  in this study, DVHs were created for the combination optic nerve exit angle in the superior-inferior and medial-lateral directions and are shown in Figure 5-2 for males and in Figure 5-3 for females. These DVH plots are similar to the case for the 'mean' optic nerve DVH, except for the superior-lateral combination (upper right graphs in these figures). An optic nerve oriented in such a position is likely to come close to the beams exiting the eye, and patients in this case may receive localized optic nerve doses as high as 17.5

Gy for males and 15 Gy for females to less than 1% of its volume. Nevertheless, only 2-3% of the male and ~1% of the female 'sup-lat' optic nerve model receives a dose exceeding 8 Gy. This extreme situation for the reference male patient is shown in the form of a dose contour map in Figure 5-4. As can be seen, only the outermost periphery of the optic nerve is irradiated in this worst-case optic nerve position. Anatomically, this region of the optic nerve would constitute the insulating myelin sheath and would most likely not be of radiobiological importance to nerve function. Thus, the risk of radiation optic neuropathy (RON) is hypothesized to be exceedingly small.

### **5.2.3 Effective Dose**

The calculation of effective dose combined both contributions from primary tube output and leakage estimation. For the primary output, the relevant absorbed tissue doses necessary to calculate effective dose are listed in Table 5-2 for the reference male and female head models. The calculation, based on ICRP Publication 103 recommendations, yields an effective dose of 0.281 mSv for a 3 x 8 Gy treatment to the macula per eye. For leakage contribution, all radiosensitive organs in the head and torso were considered, and the result of the ICRP 103 based calculation was 0.009 mSv. Thus, the total effective dose for a 3 x 8 Gy treatment is 0.29 mSv.

While the stereotactic AMD radiosurgery is therapeutic in nature, this value of effective dose compares very favorably with radiographic imaging doses including skull radiographs (0.1 mSv) and cervical spine radiographs (0.2 mSv), yet are much lower than seen in CT scans of the head (2 mSv) or neck (3 mSv).<sup>54</sup> In contrast, estimates of effective dose in megavoltage radiotherapy are significantly higher as in treatments of head and neck tumors (1870 mSv), brain metastases (270 mSv), and brain primary tumors (580 mSv).<sup>55</sup> Clinical trials are still underway and a smaller therapeutic dose

may eventually be prescribed. For example, if a 16 Gy total dose to the macula is shown to yield good clinical outcome, the estimated effective dose would be proportionally lower (e.g., 0.19 mSv).

### 5.3 Patient Specific Dose Assessment

Dose volume histograms are the most common form of data used to evaluate non-target complication probabilities (NTCP). An alternative to DVH output was contrived for reporting doses to non-targeted tissues in the patient specific population. The alternative approach allows for a more condensed data format with specific quantitative values listed in the form of dose distribution tables. The column headings in these tables are equivalent to the x-axis of a DVH and the values in the tables correspond to the shape of a DVH. The total voxelized volume of the optic nerve, lens, and macula and the percent volume of that tissue over several dose regions are shown in Tables 5-3, 5-4, and 5-5, respectively. The dose regions in the table were chosen in an effort to most clearly depict the distribution of dose within each tissue volume. A conservative approach was taken in reporting volumes to the optic nerve and lens; the reported volumes include all voxels wherein the mean dose plus the computational uncertainty surpasses the given table heading. The reverse is true for the macula table, that is, the mean dose minus the computational uncertainty surpasses that given table heading. The details of the MATLAB code used for this calculation are shown in Appendix B. The abbreviation for each eye model is as follows: the first letter denotes gender (m/f), the second letter denotes subject (A,B,C etc), and the third letter denotes left or right eye (l/r). For example, female subject D's left eye will be denoted as patient model *fdl*.

Table 5-3 is organized in three parts according to clinical realism. A patient model was selected from each of the groups for the formulation of dose contour maps which

are shown in Figures 5-5, 5-6, and 5-7. Table 3 presents the highest (of the set of 32 eye models) tissue-averaged dose to the lens and optic nerve, along with the associated eye model. For all models, no brain voxel received a dose over 12 Gy, the threshold for necrosis. Patient model *fdl* received the highest orbital bone dose with 5 voxels (1.125 mm<sup>3</sup>) receiving between 45 and 50 Gy.

Despite the variability of the location of the optic nerve observed in this study, the highest cumulative tissue-averaged dose received was 1.3 Gy by model *fkf* (Table 5-6). Dose contour maps were fabricated for this patient (Figure 5-6) and it can be seen that the overlapping beams avoid the optic nerve. This patient demonstrated a lateral horizontal gaze of roughly 16°, outside the range of clinically relevant horizontal gaze angles. It is somewhat unclear from the literature what maximum point dose is tolerated by the optic nerve; nevertheless, it is reasonable to assume that the risk of developing RON is negligible for all simulated patient models in this study given the dose volume data presented in Table 5-3.

The highest tissue-averaged dose observed in the present study was 176 mGy by eye model *fol* (Table 5-6). Eye model *fjl* had the highest percentage of volume receiving doses over 300 mGy and no lens volume received a dose exceeding 400 mGy (Table 5-4). The sagittal dose contour map and the most inferior voxelized slice that contains the lens of patient *fjl* are shown in Figure 5-7 and both clearly depict that the converging beams do not directly intersect the lens.

An attempt was made to find correlations between absorbed dose to non-targeted tissues and the measurement parameters mentioned before. For most tissues, there were no statistically significant relationships. Analysis of optic nerve data provided two

significant correlations. These are presented in Figures 5-8 and 5-9. The latter relationship is intuitive; the optic nerve dose will escalate with increasing optic nerve thickness. The former may not be intuitive at first, but becomes clearer with a better understanding of optic nerve tilt as a function of gaze angles. The logarithmic regressions suggest that optic nerve dose increases as vertical and lateral gazes increase. As described in Chapters 2 and 3, an increasing vertical gaze will stretch the optic nerve into a more vertical exit tilt, which would position the optic nerve closer to the beams exiting the eye. As lateral gaze increases, the optic nerve tilt decreases (approaching a limit of being positioned in parallel with the sagittal reference plane described in section 3.3.2) and positions itself in closer proximity to the beam entering from the lateral side (exiting medially from the eye ball). This would be the 5 o'clock beam for the left eye and the 7 o'clock beam for the right eye.

#### **5.4 Photon Fluence Evaluation**

Figures 5-10, 5-11, and 5-12 show that photon fluence was mostly forward directed with respect to the patient's gaze (backscattered in reference to beam entry) with maxima in the 50-60° and 44.4-50 keV bins. A portion of the beam traverses through the head unattenuated, resulting in a smaller peak around 150°. Color coded contour fluence maps are presented in Figure 5-13 to supply a visual representation of fluence. The results of this study provide a better understanding of the radiation physics involved during treatment administration and contributed towards the design of shielding for the treatment device.

Table 5-1. Mean absorbed dose (mGy) to various tissues in the reference head models for a 3 x 8 Gy Oraya Treatment to the right eye; computational error was less than 2% for the optic disc and less than 1% for all other tissues

Beam Azimuthal Angle:	Male			Female		
	150°	180°	210°	150°	180°	210°
Right Macula	8000	8000	8000	8000	8000	8000
Right Lens	46.7	40.6	36.5	47.3	42.7	37.0
Right Optic Disc	211	200	201	239	210	212
Right Optic Nerve	48.2	56.8	93.8	56.4	68.5	112.0
Left Optic Nerve	0.92	1.11	1.40	1.84	2.00	2.44
Brain	2.96	3.72	4.25	3.82	4.86	4.94
Thyroid	0.05	0.05	0.06	0.09	0.09	0.09
Parotid	0.31	0.28	0.30	0.53	0.51	0.52
Submaxillary	0.39	0.38	0.42	0.34	0.36	0.38
Sublingual	0.23	0.24	0.26	0.59	0.58	0.57
Cranium (AM)	3.64	3.25	2.86	3.95	3.54	3.28
Mandible (AM)	0.29	0.29	0.30	0.48	0.47	0.47
Vertebrae (AM)	0.14	0.15	0.19	0.27	0.31	0.37
Cranium (BS)	8.86	7.94	7.04	9.67	8.71	8.10
Mandible (BS)	0.94	0.92	0.97	1.56	1.53	1.51
Vertebrae (BS)	0.46	0.49	0.60	0.87	0.99	1.18

Table 5-2. Mean whole-body absorbed doses  $D_T$  (mGy) for the estimate of the effective dose

Beam Azimuthal Angle:	Male			Female		
	150°	180°	210°	150°	180°	210°
Brain	2.96	3.72	4.25	3.82	4.86	4.94
Thyroid	0.05	0.05	0.06	0.09	0.09	0.09
Salivary Glands	0.32	0.31	0.33	0.48	0.47	0.48
Bone Marrow	0.29	0.26	0.23	0.31	0.28	0.27
Bone Surfaces	1.37	1.23	1.09	1.55	1.40	1.31

Table 5-3. The gaze angles, voxelized optic nerve volume, and percentage of that volume receiving more than the absorbed dose listed, representing the dose distribution, for a cumulative 24 Gy treatment dose to the macula

Model	Vertical Gaze Angle degrees	Horizontal Gaze Angle degrees	Optic Nerve Voxel Volume mm <sup>3</sup>	0.5 Gy %	1 Gy %	5 Gy %	12 Gy %
Both vertical and horizontal gaze are clinically realistic							
fkr	9.0	-3.2	556.8	8.7	3.2	0.9	0
fnl	9.5	2.2	664	7.4	2.1	0.6	0.2
mel	-0.8	-1.0	632.5	9.2	3.5	1.3	0.2
mer	-1.0	-0.3	621.9	6.8	2.4	0.7	0
mkl	5.2	-2.9	599.4	10.7	3.7	1.5	0.4
mkr	8.7	1.2	702.8	9.9	4.1	1.9	0.6
mll	7.2	-4.4	523.8	11.3	4.0	0.8	0
Either vertical or horizontal gaze is clinically realistic							
mlr	4.5	-6.0	640.3	16.4	8.8	4.1	0.9
fkl	8.7	-16.4	521.6	26.9	15.8	6.6	0.3
mml	-1.6	-16.7	590.6	18.1	9.0	3.5	0.1
fnr	12.6	-18.1	704.9	36.7	27.7	4.8	0.3
fsr	-3.6	3.3	551.3	10.6	4.0	1.6	0.4
mar	-6.0	-1.5	566.8	9.0	2.8	1.1	0.2
ffl	-10.9	-3.3	287.8	8.2	0.9	0	0
for	-17.7	-0.5	460.5	6.1	1.6	0.4	0
fol	-20.2	-2.6	547.1	3.4	0.7	0.1	0
Neither vertical or horizontal gaze is clinically realistic							
ftr	-2.4	-6.0	410.3	11.8	4.7	1.3	0.1
mgr	-5.3	-19.0	909.1	11.8	7.1	3.8	0.9
mal	-5.4	-5.9	431	11.4	4.3	1.8	0.3
mgl	-6.4	8.6	686.1	8.6	3.6	1.5	0.4
mor	22.1	-14.5	445	14.3	7.4	2.0	0.3
fsl	-6.8	-6.1	482.4	12.8	4.8	1.8	0.3
mfr	-7.4	-18.9	621.9	11.4	5.6	2.9	0.8
ffr	-7.5	-8.5	356.5	9.2	2.3	0.6	0.1
mmr	-7.9	-17.5	640.1	17.8	11.4	4.9	0.2
ftl	-8.5	-8.1	588.8	10.2	3.4	0.7	0.1
mfl	-8.6	-5.4	776.4	10.0	4.5	2.1	0.6
mol	30.1	-29.8	480	31.4	17.5	6.0	0.2
fdr	-34.4	-8.7	207.9	7.9	1.4	0.2	0
fdl	-34.6	7.2	259.1	4.5	0.2	0	0
fjr	-41.4	19.8	395.0	5.1	0.9	0.3	0.1
fjl	-46.5	-28.0	728.6	6.7	2.2	1.1	0.4

Table 5-4. The voxelized lens volume and percentage of that volume receiving more than the absorbed doses listed, representing the dose distribution, for a cumulative 24 Gy treatment dose to the macula

Model	Lens Voxel Volume	100 mGy	200 mGy	300 mGy	400 mGy
	mm <sup>3</sup>	%	%	%	%
fdl	133.6	86.0	5.7	0	0
fdr	128.3	90.7	8.2	0	0
ffl	100.4	87.5	7.0	0	0
ffr	109	87.6	7.5	0	0
fjl	135.9	90.2	26.1	3.1	0
fjr	115.8	80.6	11.9	0.3	0
fkl	74.6	96.1	8.2	0	0
fkr	94.1	99.3	18.9	0	0
fnl	123.6	82.5	2.0	0	0
fnr	114	91.6	4.9	0	0
fol	101	99.9	30.3	2.4	0
for	94.8	98.5	18.2	0	0
fsl	142.8	94.0	7.2	0	0
fsr	146	95.3	6.8	0	0
ftl	104.5	84.4	2.9	0	0
ftr	122.9	81.3	4.4	0	0
mal	138.9	78.2	4.8	0	0
mar	144.3	97.6	27.5	2.5	0
mel	97	97.0	12.1	0	0
mer	97.9	99.5	15.8	0	0
mfl	118	81.9	0	0	0
mfr	92.9	90.8	0	0	0
mgl	159.4	83.5	7.8	0	0
mgr	148.1	84.5	6.8	0	0
mkl	111	99.0	12.0	0	0
mkr	102.4	91.0	1.3	0	0
mll	139	89.0	8.4	0	0
mlr	133.9	92.9	7.5	0	0
mml	134.4	93.1	8.1	0	0
mmr	131.1	83.9	4.9	0	0
mol	119.8	89.0	10.3	0	0
mor	113.4	96.3	13.3	0	0

Table 5-5. The voxelized macula volume and percentage of that volume receiving more than the absorbed doses listed, representing the dose distribution, for a cumulative 24 Gy treatment dose to the macula

Model	Macula Voxel Volume mm <sup>3</sup>	5 Gy %	10 Gy %	15 Gy %	20 Gy %	25 Gy %
fdl	6.3	100	100	100	100	0
fdr	6.1	100	100	100	95.9	0
ffl	6.3	100	100	100	100	0
ffr	6.3	100	100	100	100	0
fjl	6.4	100	100	100	96.1	0
fjr	6.1	100	100	100	100	0
fkl	6.5	100	100	100	100	0
fkr	6.1	100	100	100	95.9	0
fnl	6.4	100	100	100	96.1	0
fnr	6.3	100	100	100	96.0	0
fol	6.0	100	100	100	95.8	0
for	6.3	100	100	100	100	0
fsl	6.3	100	100	100	100	0
fsr	6.4	100	100	100	96.1	0
ftl	6.3	100	100	100	100	0
ftr	6.1	100	100	100	95.9	0
mal	6.3	100	100	100	100	0
mar	6.3	100	100	100	100	0
mel	6.1	100	100	100	100	0
mer	6.4	100	100	100	96.1	0
mfl	6.1	100	100	100	100	0
mfr	6.3	100	100	100	98.0	0
mgl	6.4	100	100	100	96.1	0
mgr	6.4	100	100	100	96.1	0
mkl	6.1	100	100	100	95.9	0
mkr	6.4	100	100	100	96.1	0
mll	6.4	100	100	100	96.1	0
mlr	6.4	100	100	100	100	0
mml	6.0	100	100	100	95.8	0
mmr	6.3	100	100	100	96.0	0
mol	6.5	100	100	100	100	0
mor	6.3	100	100	100	98.0	0

Table 5-6. The highest tissue-averaged doses received from the set of 32 eyes undergoing treatment simulation and the associated eye model; computational error was less than 1% for all values

Tissue	Beam I mGy	Beam II mGy	Beam III mGy	Total mGy
macula	8000	8000	8000	24000
lens	66 (mar)	57 (fol)	69 (fol)	176 (fol)
optic nerve	747 (fkl)	276 (mol)	1100 (fnr)	1291 (fkl)

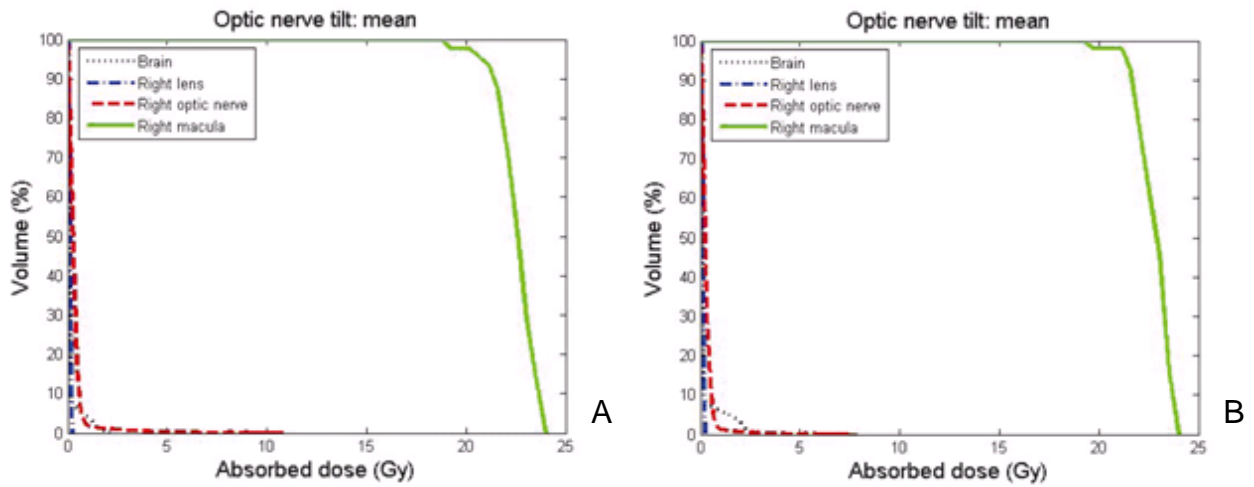


Figure 5-1. DVHs for the 'mean' optic nerves; (A) male (B) female

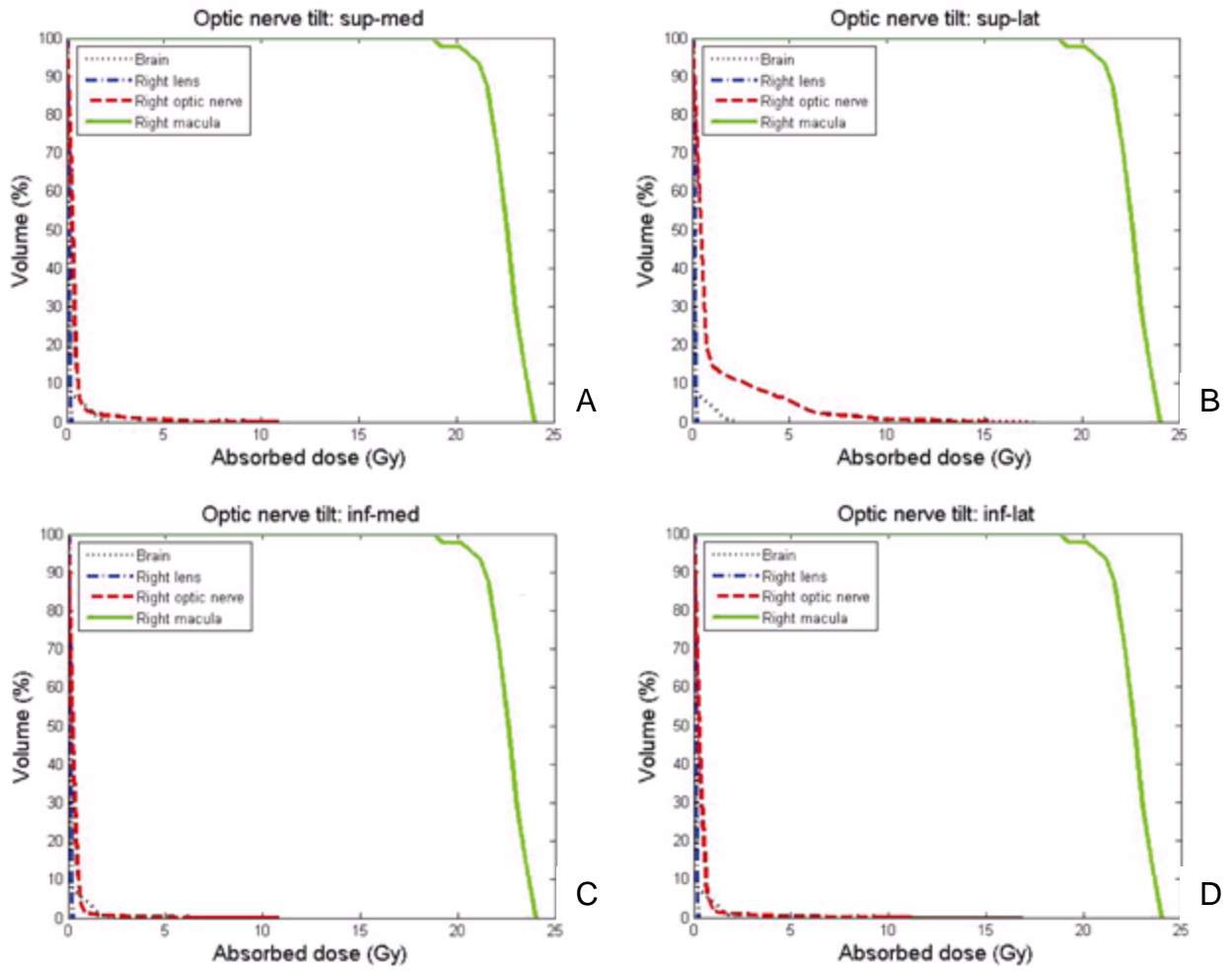


Figure 5-2. DVHs for the extremes of male optic nerve tilt; (A) sup-med (B) sup-lat (C) inf-med (D) inf-lat

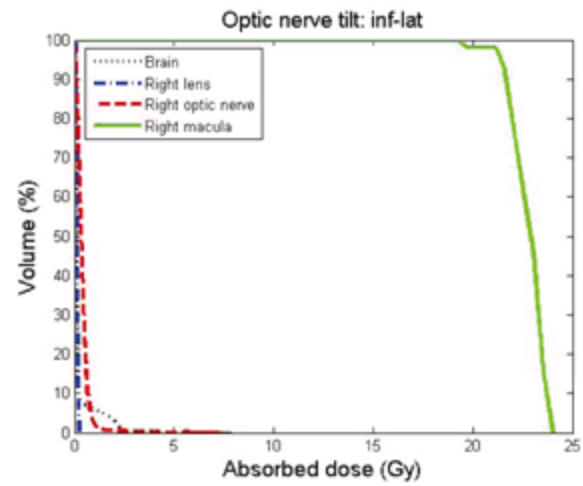
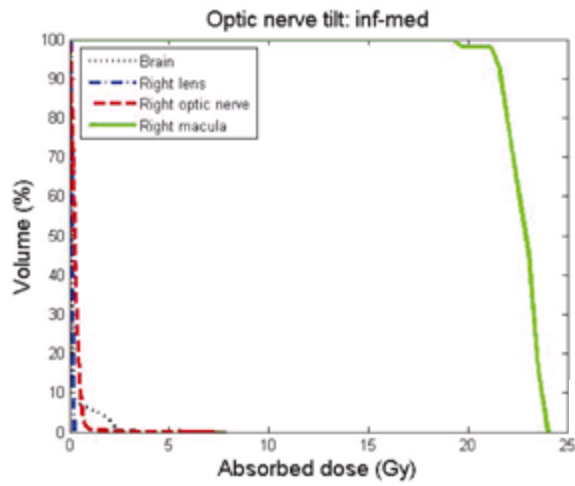
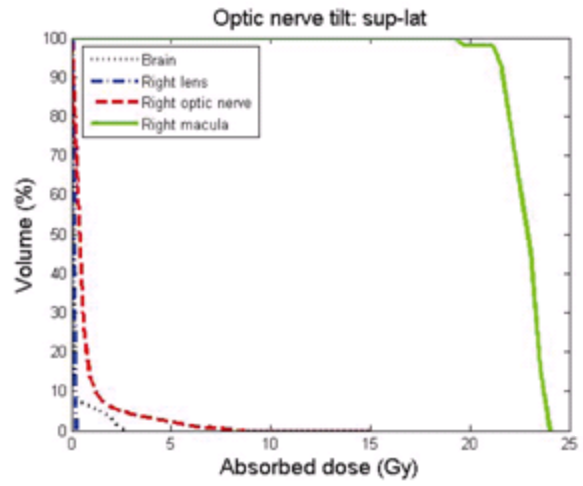
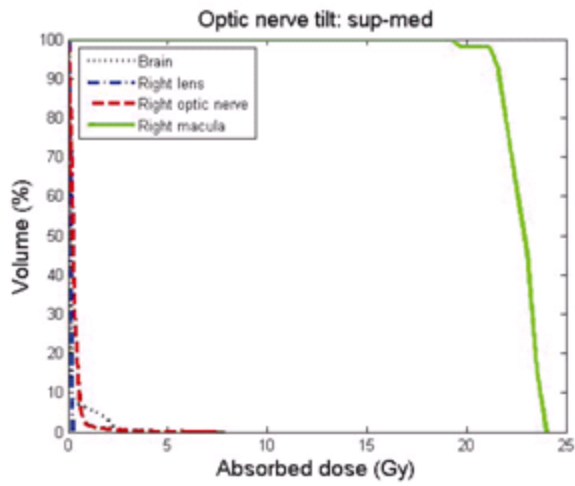


Figure 5-3. DVHs for the extremes of female optic nerve tilt; (A) sup-med (B) sup-lat (C) inf-med (D) inf-lat

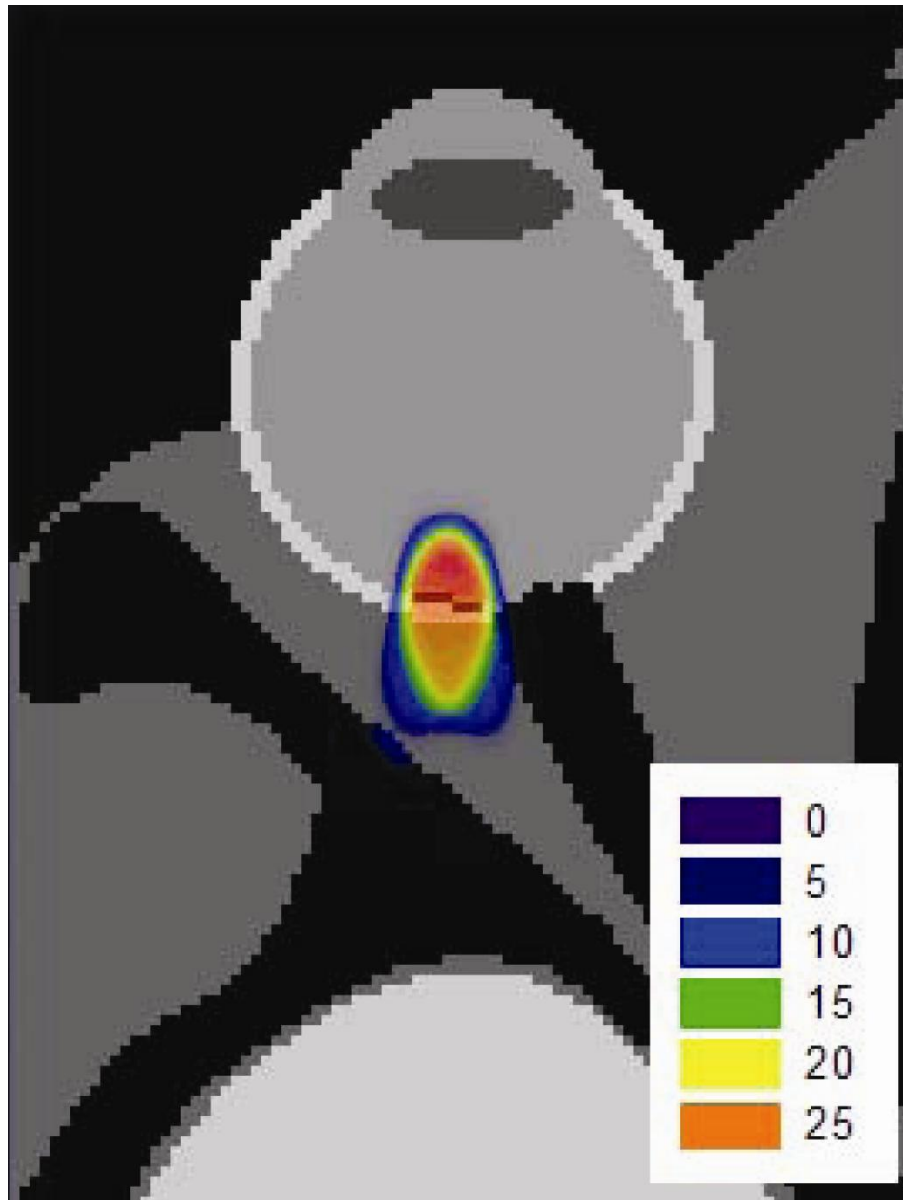


Figure 5-4. Spatial contour map of the dose distribution within the reference eye model of the adult male; legend units are Gy where 0 refers to some value approaching the limit of 0

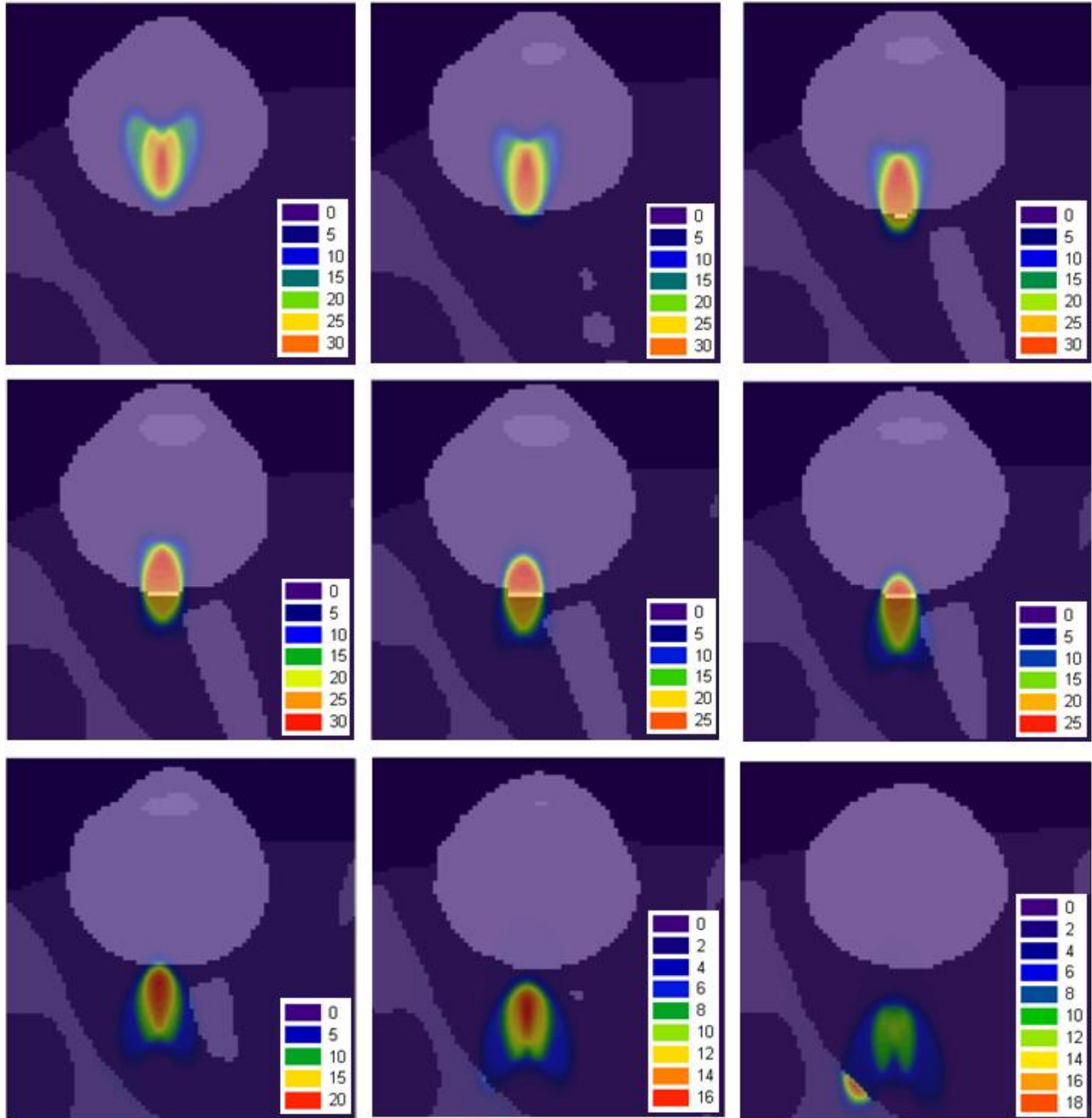


Figure 5-5. Dose contour maps for patient model mer; image progression is from inferior (top left) to superior (bottom right) in 1 mm intervals, with the (center) median slice intersecting the middle of the macula target; legend units are Gy where 0 refers to some value approaching the limit of 0

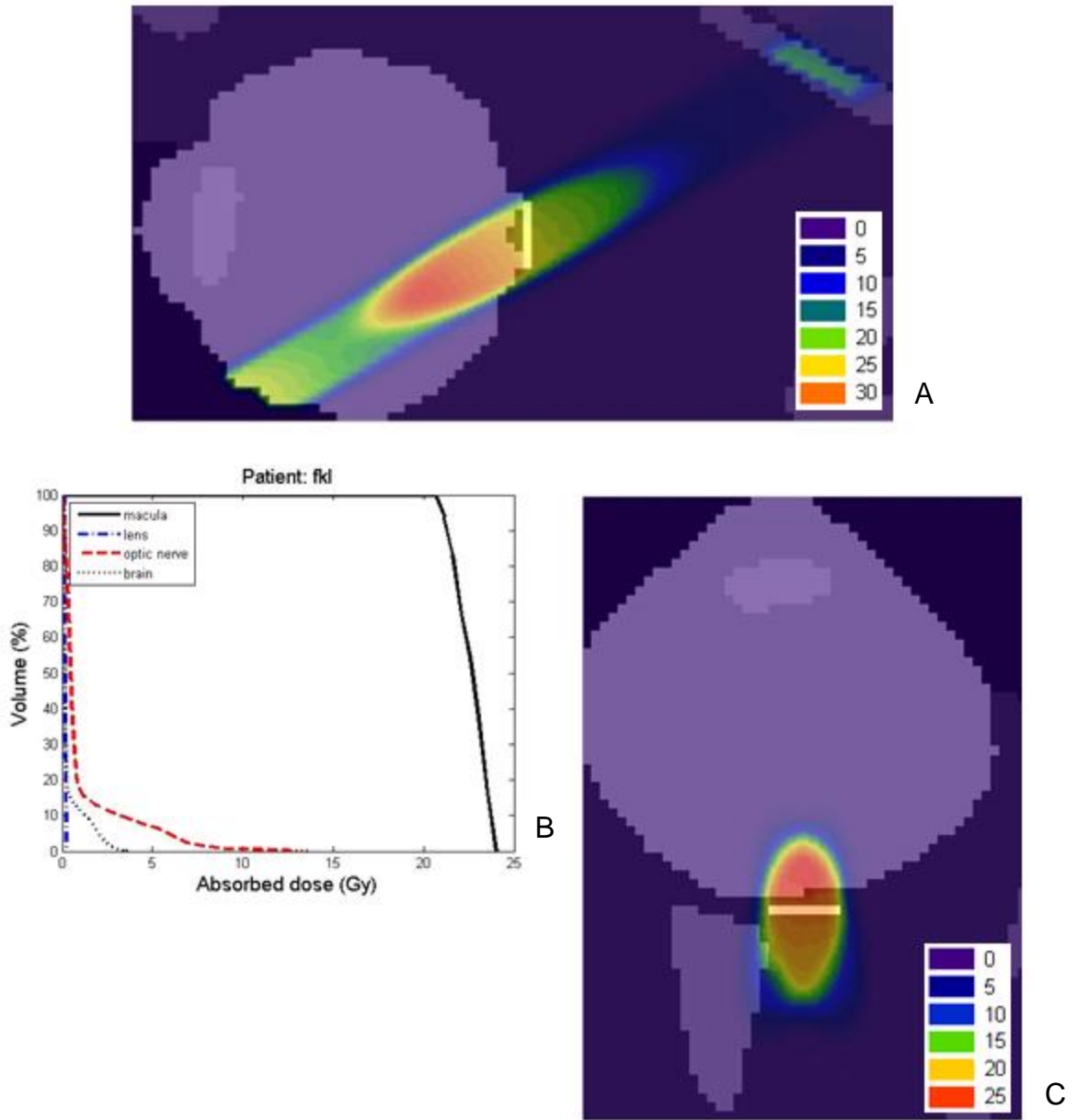


Figure 5-6. Dose contour maps for patient model fkl; (A) sagittal image slice intersecting the middle of the macula target, (B) DVH, and (C) axial image slice intersecting the middle of the macula target; legend units are Gy where 0 refers to some value approaching the limit of 0

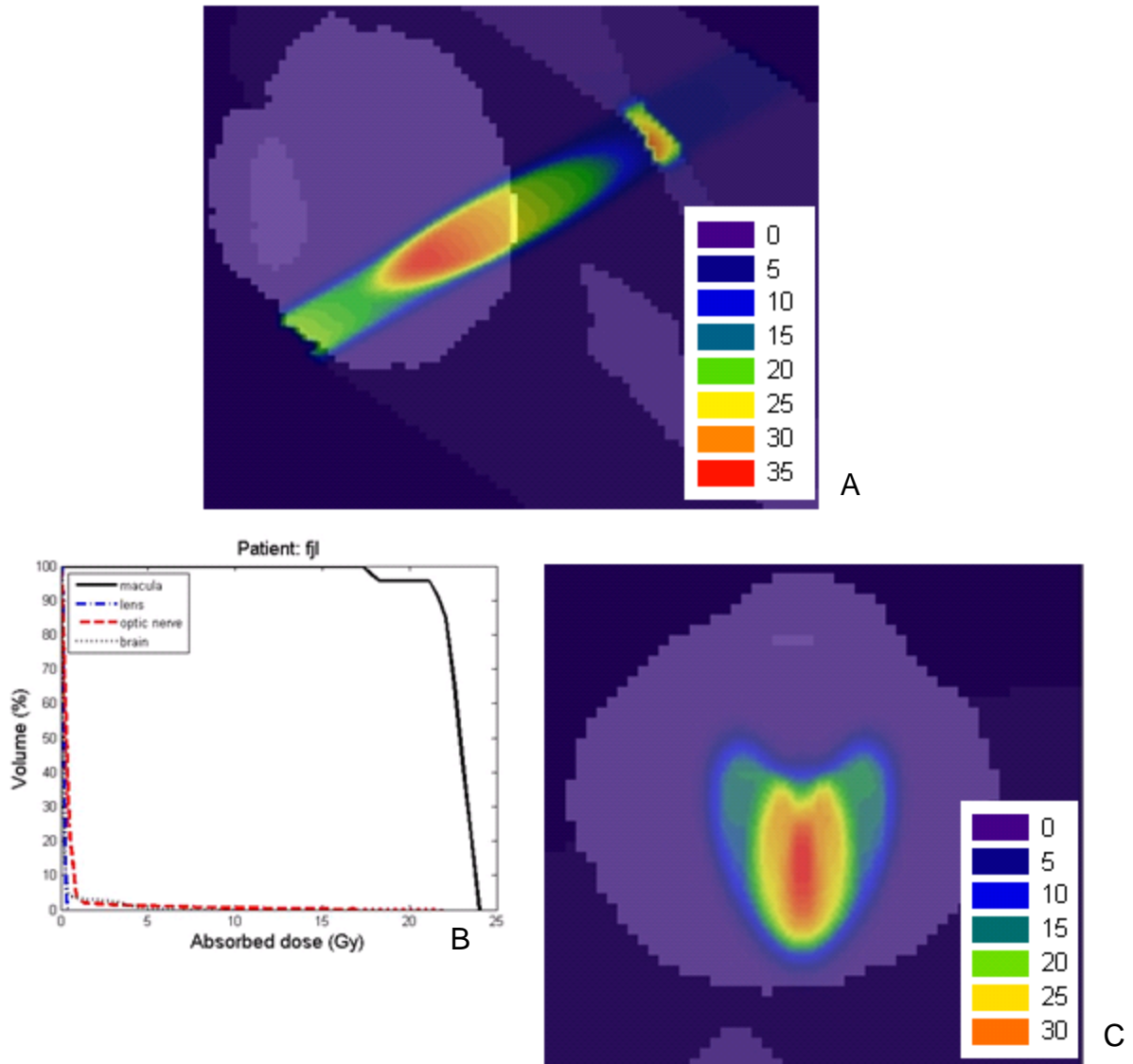
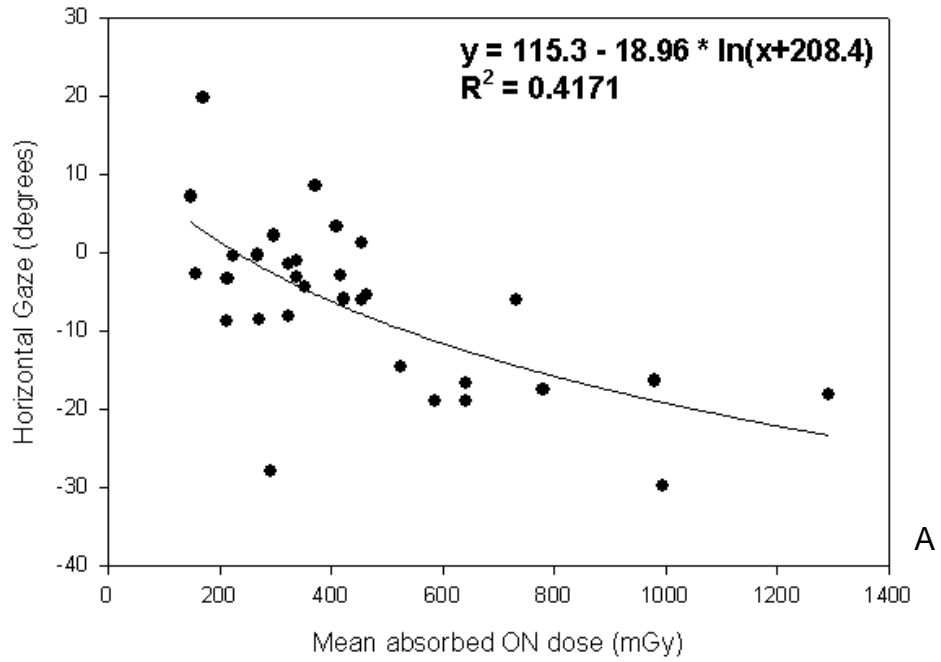


Figure 5-7. Dose contour maps for patient model fjl; (A) sagittal image slice intersecting the middle of the macula target, (B) DVH, and (C) axial image slice intersecting the middle of the macula target; legend units are Gy where 0 refers to some value approaching the limit of 0

Horizontal Gaze vs ON mean absorbed dose



Vertical Gaze vs ON mean absorbed dose

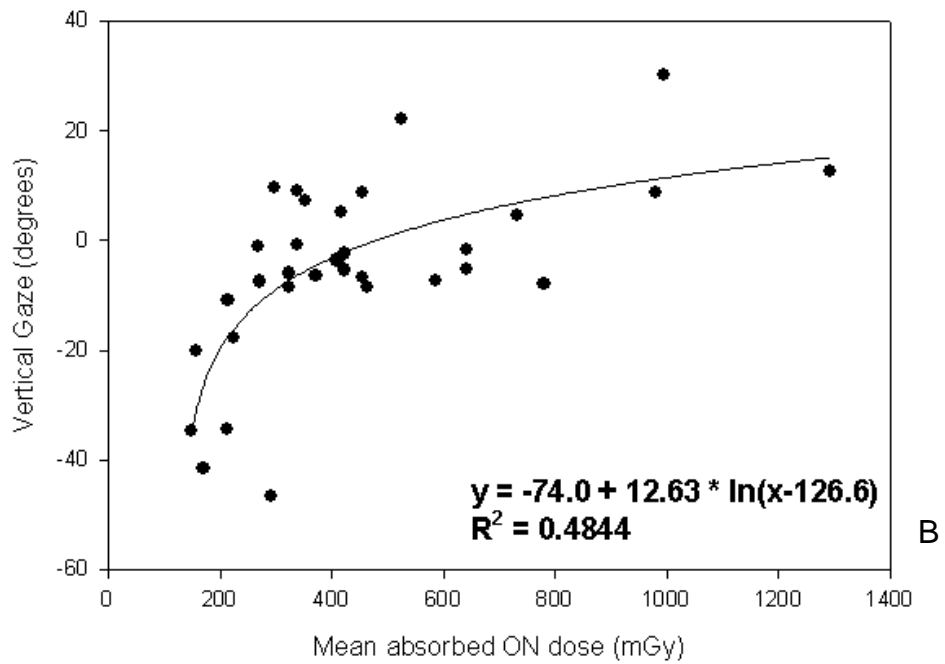


Figure 5-8. Correlation scatter plots of mean absorbed dose to the optic nerve as a function of gaze angle; (A) horizontal gaze (B) vertical gaze

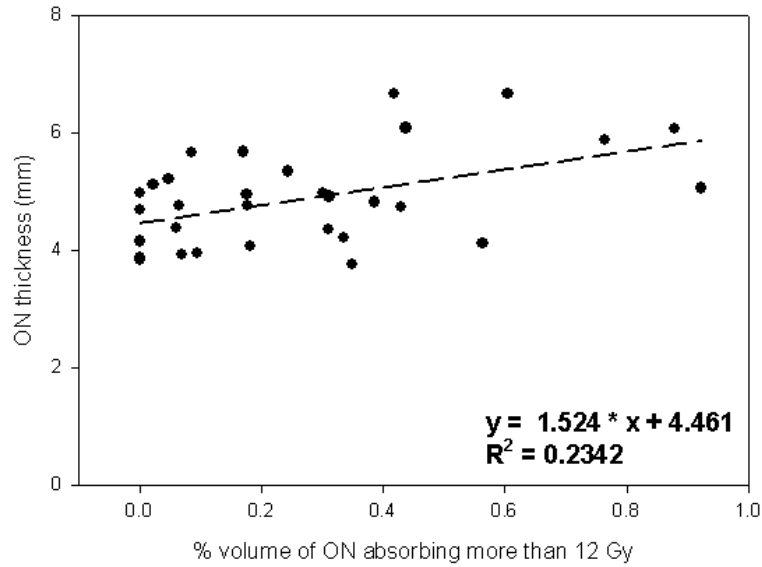


Figure 5-9. Correlation scatter plot and linear regression of optic nerve hotspot dose as a function of optic nerve thickness

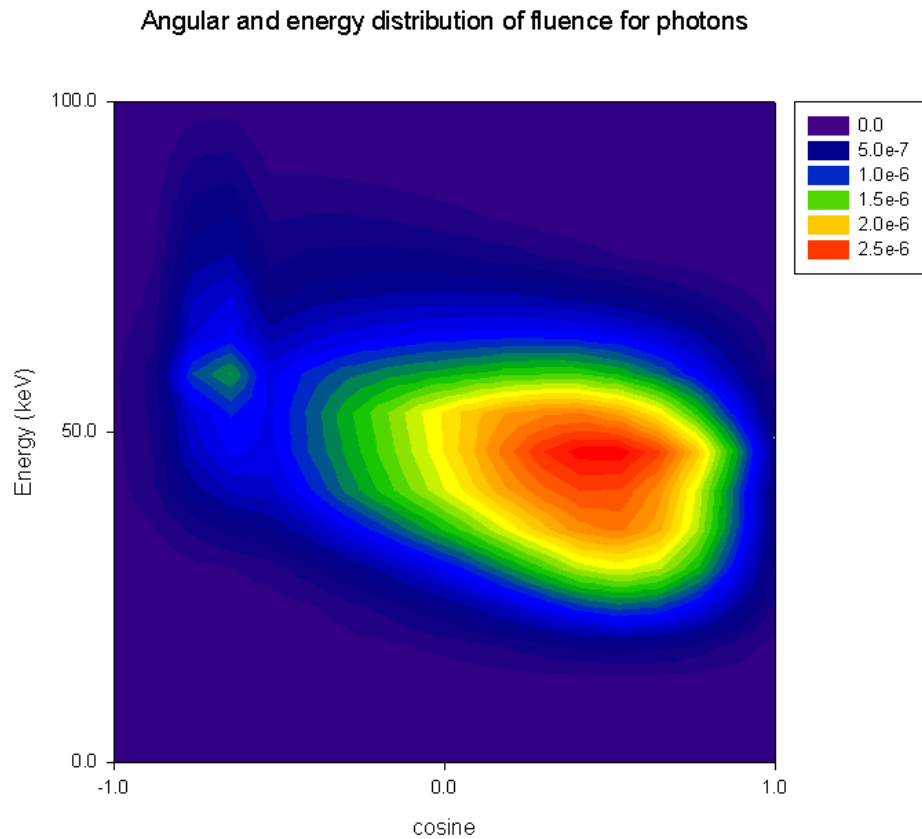
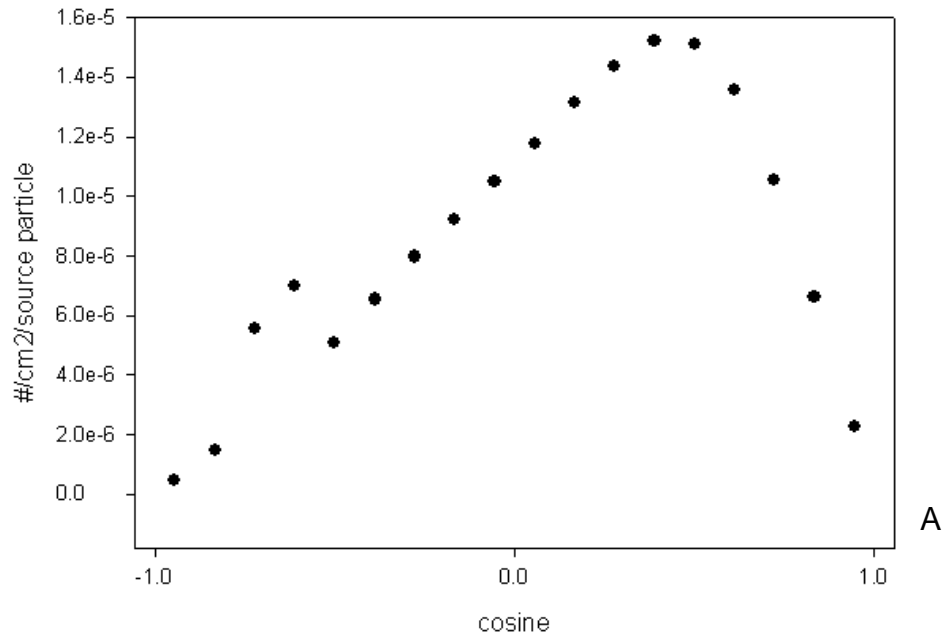


Figure 5-10. Phase space diagram of energy and angular dependence of photon fluence 50 cm from the macula target; cosine equal to 1 is synonymous with primary gaze; all units are  $\#/cm^2/history$

Angular distribution of photon fluence



Energy distribution of photon fluence

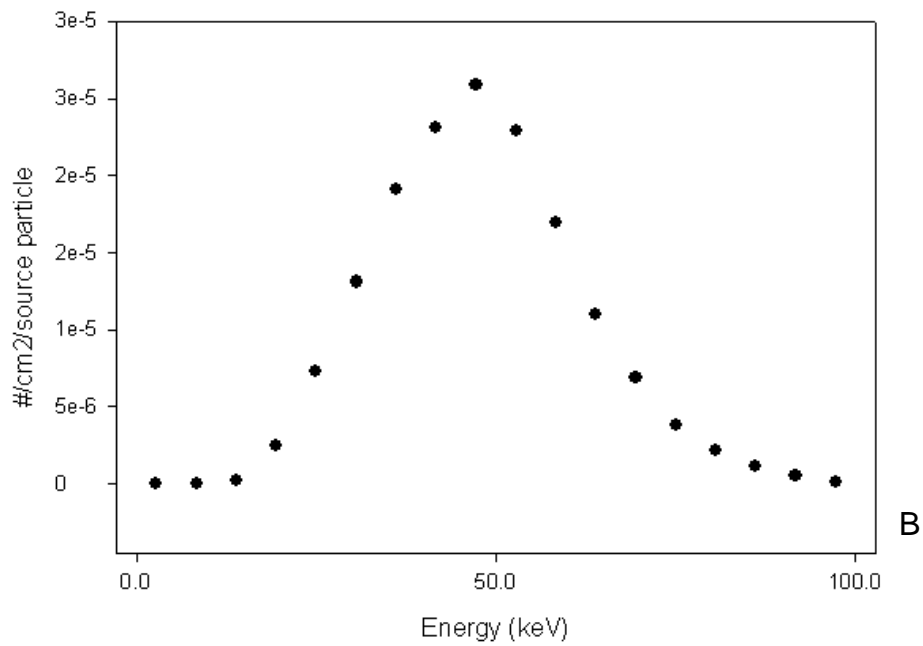


Figure 5-11. Photon fluence distribution plots 50 cm from macula target; (A) angular dependence and (B) energy dependence

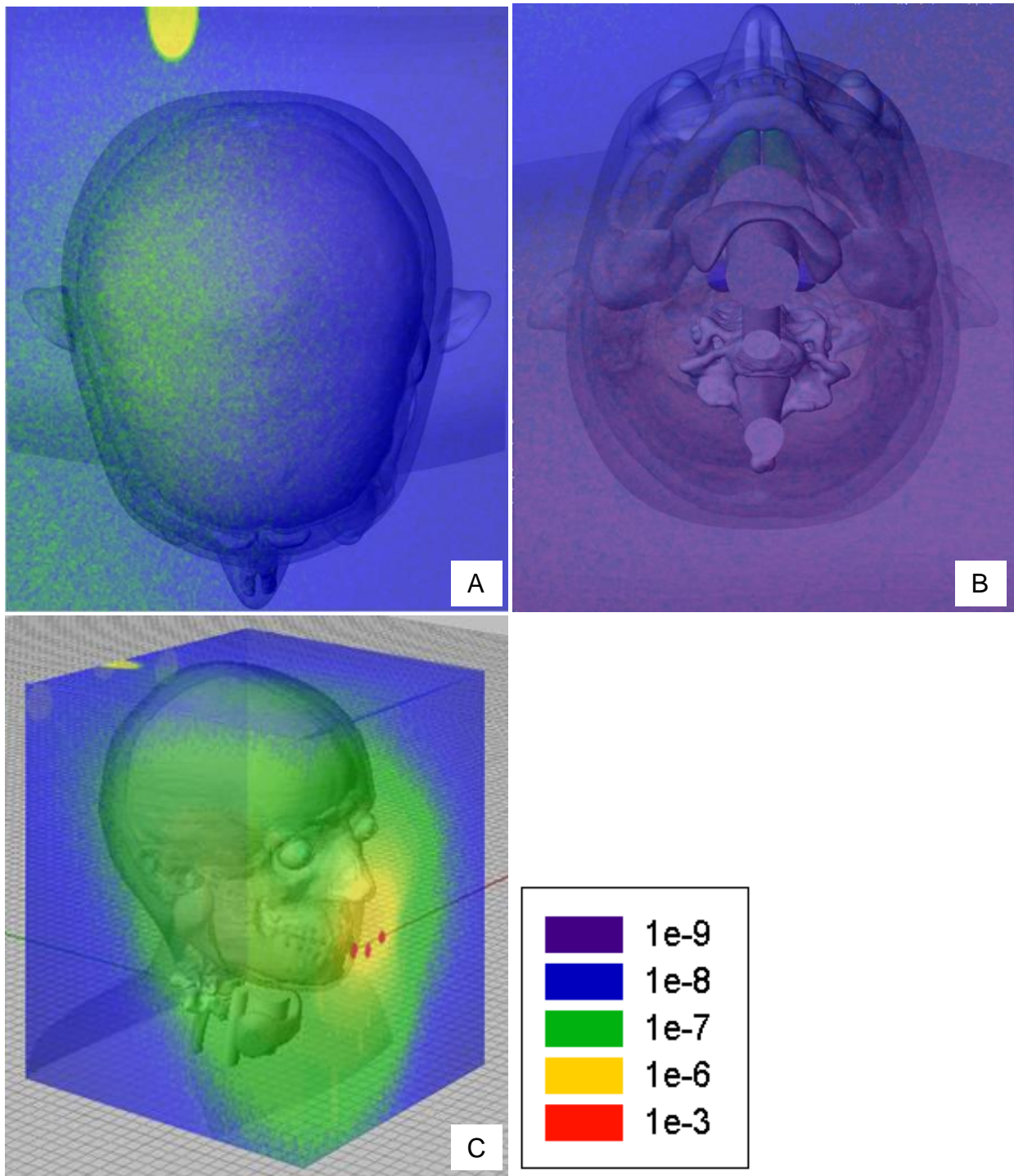


Figure 5-12. Photon fluence contour maps at the edge of the lattice structure; (A) top (B) bottom (C) perspective (D) right side (E) front (F) back and (G) left side; all units are  $\#/cm^2/history$

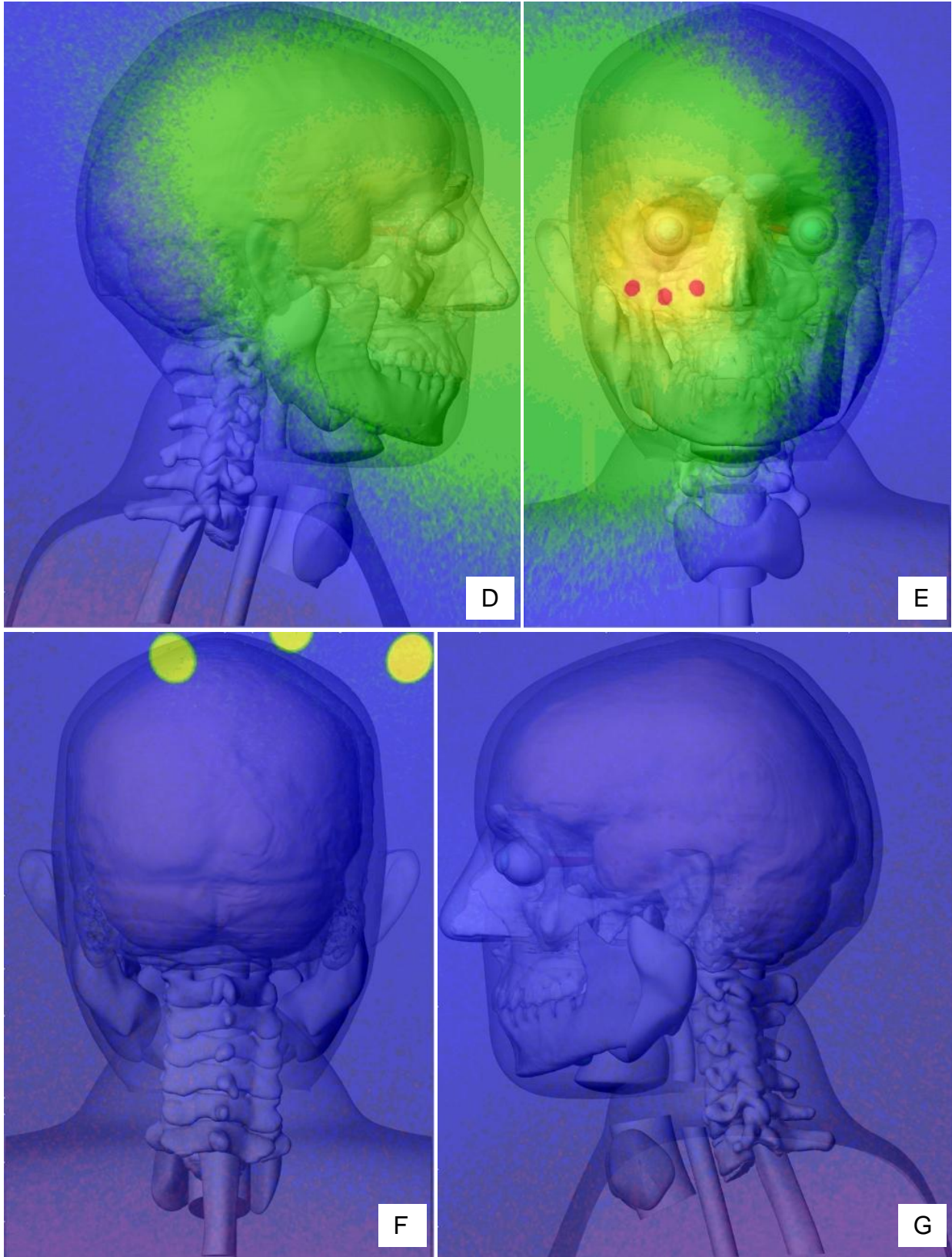


Figure 5-12. Continued

## CHAPTER 6 CONCLUSIONS

### 6.1 Limitations of This Work

The retrospective collection of CT data presented several challenges for this project. Retrospective collection was warranted to limit dose to potential volunteers. MR imaging could have been used but it would have been costly to setup a proactive study. Because the data are collected retrospectively, and not specifically for the purpose of this project, patients display a wide variety of gaze angles and head tilt that would not typically be seen during stereotactic radiosurgery for wet AMD. Measures were taken to account for this, but ideally patient specific model fabrication and treatment planning would have been performed on a patient population potentially undergoing SRS.

It is difficult to obtain a large number of head CT images with fine slice resolution and facial structures intact. High resolution slices are desired for this project to minimize the uncertainty in the measurements taken as described in Chapter 2, but slice resolution is limited during administration because of dose considerations to the patient. When higher slice resolution is needed for the diagnostic procedure it is typically because there is some head trauma to the patient. To account for this tradeoff, a 1 mm slice resolution was chosen for data collection, and, partially due to the size of Shands Hospital at the University of Florida, enough image sets were eventually found at this resolution without significant trauma to the facial structures including the entire orbital region.

While the selection of this slice resolution allows for improved measurement accuracy for orbital structures, it presents a shortcoming in data available for the entire

cranium and brain. At 1 mm slice resolution, the top and back of the head are often left out of the image, again due to dose considerations to the patient. The lack of this data prevents the calculation of mean absorbed dose and formulation of dose volume histograms to these structures since their true total volume is unknown. Fortunately, the area of interest where dose hotspots may form are included in the image sets and valuable information can still be tabulated concerning absorbed dose to localized portions of the anatomy.

Furthermore, the sample size is still too small to be highly confident that the patient specific variations in anatomy observed are an accurate representation of the total population. The image sets were stripped of all personal health information in accordance with our IRB protocol to protect the privacy of subjects whose images were collected. The sample size is further compromised considering all the images were gathered from one location (Gainesville, FL). While Shands Hospital at the University of Florida potentially attracts patients from throughout the state, it still limits the source of data to one geographical location.

Voxel model geometry presents some disadvantages depending on the voxel resolution selected for Monte Carlo simulation. Higher voxel resolutions offer superior geometry detail but slow computer runtime and increased error in mesh tallies. The file size of high resolution voxel models present difficulties in the following scenarios: (1) in-house MATLAB codes crash from memory limitation when attempting to load binary voxel model files, (2) MCNPX has trouble compiling when attempting to load lattice files, and (3) the MCNPX built in program GRIDCONV fails when attempting to convert mdat files from mesh tallies to ASCII files. To avoid these problems, appropriate voxel

resolutions were selected for the eye and head models: 0.5 mm<sup>3</sup> and 1 mm<sup>3</sup> voxel resolution, respectively. The selection of these resolutions allowed for successful completion of all MCNPX and MATLAB operations, but these resolutions restrict the dimensions that can be accurately modeled. Specifically, the fovea offset described in Chapter 1 cannot be modeled with the same level of accuracy as the IRay™ targeting system. The 1.25 mm offset in the lateral direction will be approximated to 1 mm or 1.5 mm by the *Voxelizer* code. Despite this limitation, voxel geometry still offers numerous benefits over stylized geometry including the ability to model tissues with complex shape and preservation of patient specific anatomy.

## **6.2 General Conclusions**

A new treatment for wet AMD involving kilovoltage stereotactic radiosurgery is proposed by Oraya Therapeutics, Inc. with the establishment of the IRay™. The benefits of this treatment modality include non-invasive application, treatment time and frequency, and potentially efficacy (pending results of preliminary clinical trials). A major advancement in quantifying the position of the macula with the Oraya Shift was incorporated into the targeting system, and subsequently the modeling involved with this project.

The scope of this research involved the dosimetry characterization of the treatment scheme using a variety of anthropometric models, both reference and patient specific. Reference whole body male and female phantoms were designed by members of the Advanced Laboratory for Radiation Dosimetry Studies (ALRADS) and were used for this work with the improvement and addition of detail to the ocular anatomy. Details were derived from data in ICRP 89, NCRP 130, and measurements taken on 40 head CT scans of equal gender distribution. The statistical analysis of the

measurement parameters provided insight into which anatomical structure's sizes are gender dependent and quantified the optic nerve pathways. Five reference optic nerve models were evaluated in each head phantom based on the range of optic nerve exit tilts observed and to indirectly account for non-primary gaze angles. To fully account for varying gaze and anatomy, several patient specific voxel phantoms were derived from segmentation of the CT data collected. In all, 16 patient and 32 eye models were evaluated.

The reference models were voxelized to  $0.5 \text{ mm}^3$ ,  $1 \text{ mm}^3$ , and  $2 \text{ mm}^3$  resolution for the eye section, head and neck region, and torso, respectively. Each of the patient specific eye models were voxelized to  $0.5 \text{ mm}^3$  resolution. The voxelized versions of the phantoms were imported into MCNPX 2.5.0 Monte Carlo radiation transport code for simulation of ocular radiotherapy. The results provided insight into the mean absorbed dose received for several radiosensitive tissues at potential risk for a three beam treatment cumulating in 24 Gy delivery to the macula.

Mean absorbed doses, dose volume histograms, and effective dose were evaluated for the reference phantom. DVHs were assessed for macula target and three non-targeted tissues: lens, optic nerve, and brain. Cumulative mean absorbed doses to the lens were found to be 124 mGy in the reference male and 127 mGy in the reference female for the 3-beam treatment. Integral mean absorbed doses to the optic nerve were 200 mGy and 237 mGy in the reference male and female, respectively. The lens and optic nerve were of utmost importance and interest, and the absorbed doses received were below the generally accepted thresholds for cataracts and radiation induced optic neuropathy (RON).

The doses to the remainder of the tissues in the reference phantom were used to estimate an effective dose as per ICRP Publication 103 schema. The effective dose for the proposed stereotactic AMD radiotherapy, including contribution from both the primary tube output and leakage, is estimated to be 0.29 mSv which is a factor of  $\sim 10^2$  to  $10^3$  lower than seen in external beam radiotherapy, a factor of  $\sim 10$  lower than seen in CT imaging, and is comparable to that seen in radiographic imaging of the head and neck.

Considering the patient specific phantom series (n=32), the dosimetry performed for kilovoltage stereotactic radiosurgery treatment simulation show that tissues at risk do not receive tissue-averaged doses over the generally accepted thresholds for complications, specifically the formation of cataracts and brain necrosis. Likewise, point doses delivered to the optic nerve were not significant in terms of the risk associated with developing RON. This study provided a worst-case-scenario risk assessment by including a range of clinically unrealistic gaze angles, and correspondingly a diverse range of optic nerve positions. The eye models receiving the highest average or point doses were further analyzed using dose contour maps. Trends were observed for dose as a function of gaze angle in the horizontal and vertical directions, and dose escalation corresponded to increasing optic nerve thickness.

Ultimately, considering the results of this work, the treatment scheme employed by the IRay<sup>TM</sup> device has the potential to deliver a therapeutic dose to the macula with minimal irradiation of non-target tissues within a set limit of clinically realistic gaze angles. Furthermore, the doses reported in this study could be scaled proportionally for

a cumulative therapeutic dose of 16 Gy to the macula tissue, the treatment scheme currently planned for US clinical trials.

### **6.3 Future Work**

As with any work of complex nature, there always room for improvement and expanded investigations. The work of this research provided valuable data for the initial phases of the project, but device development is ongoing and Phase II clinical trials are currently being set up for the IRay™.

To date, the computational evaluation of the device has explored only variations in anatomy and gaze, and has not taken into account the uncertainty in the targeting system. A recent publication by Gertner *et al*<sup>26</sup> claims that the uncertainty and precision of the machine are 600 and 400 microns, respectively. Therefore, a computational sensitivity study could be designed to answer the question, “what if we are a little bit off?” Using the reference phantoms, the treatment axis could be transposed by 600 microns in each of the four major directions; superior, inferior, lateral, and medial to the center of the macula target. Then, fixing the target point at the center of the macula, the treatment axis could be rotated in each of the four major directions in increments of one degree up to five degrees. An evaluation of non-targeted dose could be explored much like in this present work, but also an exploration of the dose distribution to the macula.

Furthermore, experimental verification in the clinic of the computations performed could be undertaken. A real time dosimetry system coupled with physical anthropometric phantoms could not only validate the computational work, but also describe how dose is deposited as a function of treatment time.

## APPENDIX A EXAMPLE OF MCNPX INPUT CODE

```

c Reference Adult male eye voxel model
c Matrix size [90,119,93]
c Voxel resolution=0.05*0.05*0.05 cm^3
c 10-22-08
c Justin Hanlon
c The University of Florida
read file=mmeanlat noecho
1001 0 -100 fill=999 imp:p=1 $ surrounding box
c -----
c Body composition and density
c -----
1 1 -1.03 -70 u=1 imp:p=1 vol=40.269625 $residual soft tissue
4 7 -1.04 -70 u=4 imp:p=1 vol=17.91375 $Brain
11 3 -1.1 -70 u=11 imp:p=1 vol=0.525376 $external nose
12 1 -1.03 -70 u=12 imp:p=1 vol=1.468625 $right Eye (soft tissue)
29 1 -1.03 -70 u=29 imp:p=1 vol=0.952125 $nasal layer (posterior)
57 5 -0.001205 -70 u=57 imp:p=1 vol=4.273875 $Air
62 6 -1 -70 u=62 imp:p=1 vol=5.732375 $right vitreous humor (water)
64 8 -1.07 -70 u=64 imp:p=1 vol=0.21125 $right lens
66 1 -1.03 -70 u=66 imp:p=1 vol=0.005875 $right macula
68 7 -1.04 -70 u=68 imp:p=1 vol=0.001125 $right optic disc
71 101 -1.525 -70 u=71 imp:p=1 vol=28.22775 $cranium
74 7 -1.04 -70 u=74 imp:p=1 vol=0.5045 $right optic nerve
c -----
c window and outside of the window
c -----
1002 5 -0.001205 100 -1000 #2000 imp:p=1 $Out of Voxel inside medium
1003 0 1000 imp:p=0 $Out of ROI
2000 9 -19.3 -2000 2010 2030 -2020 imp:p=1 $aperture

c -----
c surface cards
c -----
c Matrix size [90,119,93]
c Voxel resolution=0.05*0.05*0.05
100 rpp -2.1 2.4 -2.85 3.1 -2.25 2.4 $origin at center of macula
200 rpp 0 0.05 0 0.05 0 0.05 $0.05 for voxel size
1000 so 200
70 so 200
2000 11 cy 5
2010 11 cy 0.1175
2020 11 py -7.45
2030 11 py -7.7

mode p
C Material Cards
c Defined using ICRP 46 tissue compositions
C Soft tissue (male) (rho=1.03)
m1 1000 -0.105
    6000 -0.256
    7000 -0.027
    8000 -0.602

```

```

11000 -0.001
15000 -0.002
16000 -0.003
17000 -0.002
19000 -0.002
c rest of the material cards omitted for space
c -----
c tally
c -----
fc6 right lens
*f6:p 64 $jerks/g
fc16 right macula
*f16:p 66
fc26 right optic disc
*f26:p 68
fc36 right optic nerve
*f36:p 74
c DVH mesh tally for right lens, macula, optic nerve, brain
tmesh
c Matrix size [90,119,93]
c rpp -2.1 2.4 -2.85 3.1 -2.25 2.4
rmesh1:p pedep
cora1 -2.1 89i 2.4
corb1 -2.85 118i 3.1
corc1 -2.25 92i 2.4
endmd
c -----
c beam description (180 degree)
c -----
sdef par=2 x=d4 y=-15 z=d5 erg=d3 dir=d1 vec=0 1 0 tr=11
# si3 sp3
0.0005 0.00000E+00
c full energy spectra omitted for space
0.1 3.04454E+01
si4 -0.05 0.05
sp4 0 1
si5 -0.05 0.05
sp5 0 1
si1 h -1 0.999644633962 1
sp1 d 0 0.999822316981 0.000177683019
sb1 d 0 0 10
c *tr11 0.08 0.05 0.08 30 90 60 104.4775 30 64.3411 115.6589 120 41.4096 $ beam 5 o'clock
*tr11 0.08 0.05 0.08 0 90 90 90 30 60 90 120 30 $ beam 6 o'clock
c *tr11 0.08 0.05 0.08 30 90 120 75.5225 30 64.3411 64.3411 120 41.4096 $ beam 7 o'clock
nps 1e7

```

## APPENDIX B SAMPLES OF MATLAB CODES

```
% import eye phantom binary file
% mesh files (result of mdat files after GRIDCONV) must be in same directory
% and must be named mesh1, mesh2, and mesh3
clear all;
name=input('Cropped model name?', 's');

%mesh file adjustment
beam=5:7;
for j=1:3;
    filename=['mesh', num2str(j)];
    fid=fopen(filename);

    c=textscan(fid, '%s', 'delimiter', '\n');
    fclose(fid);
    d=length(c{1});
    e=(length(c{1})-10) ./2;

%mesh w/o error generation
    f=e+10;
    for i=11:f
        g{1}{i-10}=c{1}{i};
    end
    filename=['mesh', num2str(beam(j))];
    fid=fopen(filename, 'w');
    for i=1:e
        fprintf(fid, '%s\n', g{1}{i});
    end
    fclose(fid);
    clear f g;

%error mesh generation
    f=e+11;
    for i=f:d;
        g{1}{i-f+1}=c{1}{i};
    end
    filename=['error', num2str(beam(j))];
    fid=fopen(filename, 'w');
    for i=1:e
        fprintf(fid, '%s\n', g{1}{i});
    end
    fclose(fid);
    clear c d e f g i j filename;
end

%phantom matrix generation
nameid1=str2num(char(name(5:6)));
nameid2=str2num(char(name(8:10)));
nameid3=str2num(char(name(12:13)));
fid = fopen(name);
phantom=reshape(fread(fid, 'ubit8'), nameid1, nameid2, nameid3);
fclose(fid);
clear nameid1 nameid2 nameid3;
```

```

phantom(find(phantom==0))==57;
s=size(phantom);

% assign organ tag and density
organ_density=[
1  1.03      % residual soft tissue
2  1.04      % Brain
3  1.525     % skull
4  1.04      % optic nerve
5  1         % vitreous humor
6  1.07      % lens
7  1.03      % macula
57 0.001205]; % air

% assign organ name
organ_name=cellstr(char(...
'Residual soft tissue',...
'brain',...
'skull',...
'optic nerve',...
'vitreous humor',...
'lens',...
'macula',...
'air'
'));

% compose density matrix to be multiplied to flux matrix from mesh tally
density_matrix=zeros(s(1),s(2),s(3));
for x=1:s(1);
    for y=1:s(2);
        for z=1:s(3);
density_matrix(x,y,z)=organ_density(find(organ_density(:,1)==phantom(x,y,z)),
2);
        end
    end
end

% read mesh tally for 5, 6, and 7 o'clock beams and sum them up
total_meshtally=zeros(s(1),s(2),s(3));
dose_werror=zeros(s(1),s(2),s(3));
target_dose=0;
for beam=5:7; % 5,6, and 7 o'clock beam direction
target_dose=target_dose+8;
filename=['mesh',num2str(beam)];
temp=reshape(load(filename),s(2),s(3),s(1));
meshtally=zeros(s(1),s(2),s(3));
    filename2=['error',num2str(beam)];
    temp2=reshape(load(filename2),s(2),s(3),s(1));
    errormatrix=zeros(s(1),s(2),s(3));
for x=1:s(1);
    for y=1:s(2);
        for z=1:s(3);
            meshtally(x,y,z)=temp(y,z,x);
            errormatrix(x,y,z)=temp2(y,z,x);
% incorporate computational error
            if phantom(x,y,z)==7;

```

```

                dose_werror(x,y,z)=meshtally(x,y,z)-
meshtally(x,y,z).*errormatrix(x,y,z);
                else

dose_werror(x,y,z)=meshtally(x,y,z)+meshtally(x,y,z).*errormatrix(x,y,z);
                end
            end
        end
    end

% unit conversion
% MeV/cm3 / density(g/cm3) * 1.6e-13 * 1e3 = Gy/particle
dose_werror=dose_werror./density_matrix.*1.6e-13.*1e3;
dose_werror(find(phantom==57))=0;
total_meshtally=total_meshtally+dose_werror;
end

% DVH plotting -----
% modify dvh_organ array for organ tags you're interested in
% currently the number of organs for DVH is limited to 5 which is enough
graph_color=cellstr(char('-k','-b','--r',':k','--b'));
dvh_organ=[7 6 4 2];
maximum_macula_dose=max(total_meshtally(find(phantom==7)));
hold off
for i=1:size(dvh_organ,2)
    legend_title(i)=organ_name(find(organ_density(:,1)==dvh_organ(i)));
    maximum_dose=max(total_meshtally(find(phantom==dvh_organ(i))));
    dose=[0:maximum_dose/50:maximum_dose];
    dvh_temp=hist(total_meshtally(find(phantom==dvh_organ(i))),dose);
    dvh_temp(51)=0;
    for j=size(dose,2):-1:2;
        dvh_temp(j-1)=dvh_temp(j-1)+dvh_temp(j);
    end
plot(dose/maximum_macula_dose*target_dose,dvh_temp./dvh_temp(1)*100,char(graph_color(i),'LineWidth',2.5));
hold on
end
titlename=['Patient: ',char(name(1:3))];
title(titlename,'fontsize',14);
xlabel('Absorbed dose (Gy)','fontsize',14);
ylabel('Volume (%)','fontsize',14);
legend(char(legend_title),2);

%dose distribution code
%scales doses to give max macula dose 24Gy
maximum_macula_dose=max(total_meshtally(find(phantom==7)));
sourceparticlesneeded=24/maximum_macula_dose;
dosematrix=total_meshtally.*sourceparticlesneeded;

braindose=zeros(1,5);
skulldose=zeros(1,5);
ONDose=zeros(1,5);
lensdose=zeros(1,5);
macdose=zeros(1,5);
heading1=[0.5,1,2,5,10,1000];
heading2=[0.1,0.2,0.3,0.4,0.5,1000];

```

```

heading3=[5,10,15,20,25,1000];
heading4=[0.5,1,5,12,15,1000];
heading5=[25,40,45,47.5,50,1000];

for i=1:5
    brain=0;
    skull=0;
    ON=0;
    lens=0;
    mac=0;
    for x=1:s(1);
        for y=1:s(2);
            for z=1:s(3);
                if phantom(x,y,z)==4;
                    ON=ON+1;
                    if dosematrix(x,y,z)>=heading4(i);
                        ONdose(1,i)=ONDose(1,i)+1;
                    end
                end
                if phantom(x,y,z)==2;
                    brain=brain+1;
                    if dosematrix(x,y,z)>=heading1(i);
                        braindose(1,i)=braindose(1,i)+1;
                    end
                end
                if phantom(x,y,z)==6;
                    lens=lens+1;
                    if dosematrix(x,y,z)>=heading2(i);
                        lensdose(1,i)=lensdose(1,i)+1;
                    end
                end
                if phantom(x,y,z)==7;
                    mac=mac+1;
                    if dosematrix(x,y,z)>=heading3(i);
                        macdose(1,i)=macdose(1,i)+1;
                    end
                end
                if phantom(x,y,z)==3;
                    skull=skull+1;
                    if dosematrix(x,y,z)>=heading5(i);
                        skulldose(1,i)=skulldose(1,i)+1;
                    end
                end
            end
        end
    end
end

%converts #voxels to mm^3
brain=brain.*0.125;
skull=skull.*0.125;
ON=ON.*0.125;
lens=lens.*0.125;
mac=mac.*0.125;
braindose=braindose.*0.125;
skulldose=skulldose.*0.125;

```

```

ONDose=ONDose.*0.125;
lensdose=lensdose.*0.125;
macdose=macdose.*0.125;

%writes to excel
menu={'OAR','Total Vol','Threshold Vol'};
xlswrite('DVH_Table.xls',menu(1,:),1,'a1:c1');
xlswrite('DVH_Table.xls','O',1,'a7');
xlswrite('DVH_Table.xls',ON,1,'b7');
xlswrite('DVH_Table.xls',ONDose(1,:),1,'c7:g7');

xlswrite('DVH_Table.xls','B',1,'a5');
xlswrite('DVH_Table.xls',brain,1,'b5');
xlswrite('DVH_Table.xls',braindose(1,:),1,'c5:g5');

xlswrite('DVH_Table.xls','L',1,'a3');
xlswrite('DVH_Table.xls',lens,1,'b3');
xlswrite('DVH_Table.xls',lensdose(1,:),1,'c3:g3');

xlswrite('DVH_Table.xls','M',1,'a11');
xlswrite('DVH_Table.xls',mac,1,'b11');
xlswrite('DVH_Table.xls',macdose(1,:),1,'c11:g11');

xlswrite('DVH_Table.xls','S',1,'a9');
xlswrite('DVH_Table.xls',skull,1,'b9');
xlswrite('DVH_Table.xls',skulldose(1,:),1,'c9:g9');

% Dose map code
% Must find the slice desired and input into dosematrix(x,[:,:]) part
% Must enter the other 2 dimensions of your matrix in the reshape part
% Copy .xls output to Sigmaplot and create a 'many Z' contour map

% % -----
% % Axial
% % -----
% two_d_matrix=dosematrix(:, :, 23);
% two_d_matrix=fliplr(two_d_matrix);

% -----
% Sagittal
% -----
% two_d_matrix=dosematrix(26, :, :);
% two_d_matrix=reshape(two_d_matrix, 114, 61);

% xlswrite('Dosemap.xls',two_d_matrix);

```

## LIST OF REFERENCES

1. H. Leibowitz, D. E. Krueger and L. R. Maunder, "The Framingham Eye Study Monograph: an ophthalmological and epidemiological study of cataract, glaucoma, diabetic retinopathy, macular degeneration, and visual acuity in a general population of 2631 adults," *Surv Ophthalmol* **24**, 335-610 (1980).
2. R. P. Murphy, "Age-related macular degeneration," *Ophthalmology* **93**, 969-971 (1986).
3. N. M. Bressler, S. B. Bressler and S. L. Fine, "Age-related macular degeneration," *Surv Ophthalmol* **32**, 375-413 (1988).
4. S. Haddad, C. A. Chen, S. L. Santangelo and J. M. Seddon, "The genetics of age-related macular degeneration: a review of progress to date," *Surv Ophthalmol* **51**, 316-363 (2006).
5. J. Gass, *Stereoscopic Atlas of Macular Disease and Treatment*. (CV Mosby co, St. Louis, 1985).
6. L. A. Donoso, T. Vrabec and H. Kuivaniemi, "The role of complement Factor H in age-related macular degeneration: a review," *Surv Ophthalmol* **55**, 227-246 (2010).
7. A. DeWan, L. Mugen, S. Hartman, S. S. Zhang, D. Liu, C. Zhao, P. Tam, W. M. Chan, D. Lam, M. Snyder, C. Barnstable, C. P. Pang and J. Hoh, "HTRA1 promoter polymorphism in wet age-related macular degeneration," *Science* **314**, 989-992 (2006).
8. R. S. Snell and M. A. Lemp, *Clinical anatomy of the eye*. (Blackwell Science, Malden, MA, 1998).
9. R. W. Young, "Pathophysiology of age-related macular degeneration," *Surv Ophthalmol* **31** (1987).
10. J. Gass, "Drusen and disciform macular detachment and degeneration," *Arch Ophthalmol* **90**, 206-217 (1973).
11. Macular Photocoagulation Study Group, "Visual outcome after laser photocoagulation for subfoveal choroidal neovascularization secondary to age-related macular degeneration. The influence of initial lesion size and initial visual acuity.," *Arch Ophthalmol* **112**, 480-488 (1994).
12. Verteporfin in Photodynamic Therapy Study Group, "Photodynamic therapy of subfoveal choroidal neovascularization in pathologic myopia with verteporfin. 1-year results of a randomized clinical trial--VIP report no. 1," *Ophthalmology* **108**, 841-852 (2001).

13. P. J. Rosenfeld, D. M. Brown, J. S. Heier, D. S. Boyer, P. K. Kaiser, C. Y. Chung and R. Y. Kim, "Ranibizumab for neovascular age-related macular degeneration," *N Engl J Med* **355**, 1419-1431 (2006).
14. P. A. Quiram, K. A. Drenser, M. M. Lai, A. Capone and M. T. Trese, "Treatment of vascularly active familial exudative vitreoretinopathy with pegaptanib sodium (Macugen)," *Retina* **28**, S8-S12 (2008).
15. M. P. Avila, M. E. Farah, A. Santos, J. P. Duprat, B. W. Woodward and J. Nau, "Twelve-month short-term safety and visual-acuity results from a multicentre prospective study of epiretinal strontium-90 brachytherapy with bevacizumab for the treatment of subfoveal choroidal neovascularisation secondary to age-related macular degeneration," *Br J Ophthalmol* **93**, 305-309 (2009).
16. M. P. Avila, M. E. Farah, A. Santos, Z. Kapran, J. P. Duprat, B. W. Woodward and J. Nau, "Twelve-month safety and visual acuity results from a feasibility study of intraocular, epiretinal radiation therapy for the treatment of subfoveal CNV secondary to AMD," *Retina* **29**, 157-169 (2009).
17. H. Churei, K. Ohkubo, M. Nakajo, H. Hokotate, Y. Baba, J. Ideue, K. Miyagawa, H. Nakayama, Y. Hiraki, T. Kitasato and N. Yabe, "External-beam radiation therapy for age-related macular degeneration: two years' follow-up results at a total dose of 20 Gy in 10 fractions," *Radiat Med* **22**, 398-404 (2004).
18. H. J. Zambarakji, A. M. Lana, E. Ezra, D. Gauthier, M. Goitein, J. A. Adams, J. E. Munzenrider, J. W. Miller and E. S. Gragoudas, "Proton beam irradiation for neovascular age-related macular degeneration," *Ophthalmology* **113**, 2012-2019 (2006).
19. A. Haas, G. Papaefthymiou, G. Langmann, O. Schrottnner, B. Feigl, K. A. Leber, R. Hanselmayer and G. Pendl, "Gamma knife treatment of subfoveal, classic neovascularization in age-related macular degeneration: a pilot study," *J Neurosurg* **93**, 172-176 (2000).
20. M. Hayashi, M. Chernov, M. Usukura, K. Abe, Y. Ono, M. Izawa, S. Hori, T. Hori and K. Takakura, "Gamma knife surgery for choroidal neovascularization in age-related macular degeneration. Technical note.," *J Neurosurg* **102**, 200-203 (2005).
21. M. A. Henderson, S. Valluri, S. S. Lo, T. C. Witt, R. M. Worth, R. P. Danis and R. D. Timmerman, "Gamma knife radiosurgery in the treatment of choroidal neovascularization (wet-type macular degeneration)," *Stereotact Funct Neurosurg* **85**, 11-17 (2007).
22. S. V. Goverdhan, F. A. Gibbs and A. J. Lotery, "Radiotherapy for age-related macular degeneration: no more pilot studies please.," *Eye* **19**, 1137-1141 (2005).

23. G. J. Bergink, C. B. Hoyng, R W van der Maazen, J. R. Vingerling, W A van Daal and A. F. Deutman, "A randomized controlled clinical trial on the efficacy of radiation therapy in the control of subfoveal choroidal neovascularization in age-related macular degeneration: radiation versus observation," *Graefes Arch Clin Exp Ophthalmol* **236**, 321-325 (1998).
24. D. H. Char, A. I. Irvine, M. D. Posner, J. Quivey, T. L. Phillips and S. Kroll, "Randomized trial of radiation for age-related macular degeneration," *Am J Ophthalmol* **127**, 574-578 (1999).
25. R. P. Singh, D. Moshfeghi, E. M. Shusterman, S. A. McDormick and M. Gertner, "Evaluation of transconjunctival collimated external beam radiation for age-related macular degeneration (ARMD)," *AAO Abstract 08-PP-30018701-AAO* (2008).
26. M. Gertner, E. Chell, K. H. Pan, S. Hansen, P. K. Kaiser and D. M. Moshfeghi, "Stereotactic targeting and dose verification for age-related macular degeneration," *Med Phys* **37**, 600-606 (2010).
27. M. E. Arnoldussen, M. Shusterman, D. Fletcher, L. Renninger, L. Dang, I. Koruga, M. Firpo, J. Liang and M. Gertner, "Quantitative Measurements of Retinal Structures Relative to the Geometric Axis of the Eye," *ARVO E-Abstract 3789* **50** (2009).
28. C. Lee, E. Chell, M. Gertner, S. Hansen, R. W. Howell, J. Hanlon and W. E. Bolch, "Dosimetry characterization of a multibeam radiotherapy treatment for age-related macular degeneration," *Med Phys* **35**, 5151-5160 (2008).
29. ICRP, "ICRP Publication 89: Basic anatomical and physiological data for use in radiological protection - reference values," *Ann ICRP* **32**, 1-277 (2002).
30. NCRP, "Biological effects and exposure limits for hot particles," *National Council on Radiation Protection and Measurements Report No. 130* (1999).
31. M. W. Charles and N. Brown, "Dimensions of the human eye relevant to radiation protection," *Phys Med Biol* **20**, 202-218 (1975).
32. B. V. Worgul, *The Edward S. Harkness Eye Institute Resident's Basic Science Study Guide*. (Columbia University, New York, NY, 1991).
33. R. Unsold, J. DeGroot and T. H. Newton, "Images of the optic nerve: anatomic-CT correlation," *AJR Am J Roentgenol* **135**, 767-773 (1980).
34. J. A. Rogers, A. G. Podoleanu, G. M. Dobre, D. A. Jackson and F. W. Fitzke, "Topography and volume measurements of the optic nerve using en-face optical coherence tomography," *Optics Express* **9**, 533-545 (2001).

35. T. Krzizok and B. Schroeder, "Quantification of recti eye muscle paths in high myopia," *Strabismus* **11**, 213-220 (2003).
36. J. Hanlon, C. Lee, E. Chell, M. Gertner, S. Hansen, R. W. Howell and W. E. Bolch, "Kilovoltage stereotactic radiosurgery for age-related macular degeneration: assessment of optic nerve dose and patient effective dose," *Med Phys* **36**, 3671-3681 (2009).
37. D. Scott, "On optimal and data-based histograms," *Biometrika* **66**, 605-610 (1979).
38. T. Anthony, *Neuroanatomy and the Neurologic Exam*. (CRC Press, New York, NY, 1994).
39. C. Lee, C. Lee, D. Lodwick and W. E. Bolch, "NURBS-based 3-D anthropomorphic computational phantoms for radiation dosimetry applications," *Radiat Prot Dosimetry* **127**, 227-232 (2007).
40. W. S. Snyder, "Estimates of absorbed fractions for monoenergetic photon sources uniformly distributed in various organs of a heterogeneous phantom," Society of Nuclear Medicine MIRD Pamphlet No. 5 (1969).
41. ICRP, "ICRP Publication 23: Report on the Task Group on Reference Man," Ann ICRP (1975).
42. M. Cristy and K. F. Eckerman, "Specific absorbed fractions of energy at various ages from internal photon sources," Oak Ridge National Laboratory Report No. ORNL/TM-8381/Volumes I-VII (1987).
43. C. Lee, D. Lodwick, D. Hasenauer, J. L. Williams, C. Lee and W. E. Bolch, "Hybrid computational phantoms of the male and female newborn patient: NURBS-based whole-body models," *Phys Med Biol* **52**, 3309-3333 (2007).
44. ICRU, "Photon, electron, proton and neutron interaction data for body tissues," International Commission on Radiation Units and Measurements Report No. 46 (1992).
45. D. B. Pelowitz, "MCNPX User's Manual Version 2.5.0," (Los Alamos National Laboratory, Los Alamos, NM, 2005).
46. K. Cranley, B. J. Gilmore, G. W. A. Fogarty and L. Desponds, "Catalogue of diagnostic x-ray spectra and other data," The Institute of Physics Report No. 78 (1997).
47. ICRP, "ICRP Publication 103: Recommendations of the International Commission on Radiological Protection," Ann ICRP **37**, 1-332 (2007).

48. M. Zankl, K. F. Eckerman and W. E. Bolch, "Voxel-based models representing the male and female ICRP reference adult--the skeleton," *Radiat Prot Dosimetry* **127**, 174-186 (2007).
49. B. V. Worgul, Y. I. Kundiyeu, N. M. Sergiyenko, V. V. Chumak, P. M. Vitte, C. Medvedovsky, E. V. Bakhanova, A. K. Junk, O. Y. Kyrychenko, N. V. Musijachenko, S. A. Shylo, O. P. Vitte, S. Xu, X. Xue and R. E. Shore, "Cataracts among Chernobyl clean-up workers: implications regarding permissible eye exposures," *Radiat Res* **167**, 233-243 (2007).
50. C. A. Girkin, C. H. Comey, L. D. Lunsford, M. L. Goodman and L. B. Kline, "Radiation optic neuropathy after stereotactic radiosurgery," *Ophthalmology* **104**, 1634-1643 (1997).
51. S. L. Stafford, B. E. Pollock, J. A. Leavitt, R. L. Foote, P. D. Brown, M. J. Link, D. A. Gorman and P. J. Schomberg, "A study on the radiation tolerance of the optic nerves and chiasm after stereotactic radiosurgery," *Int J Radiat Oncol Biol Phys* **55**, 1177-1181 (2003).
52. T. Hasegawa, T. Kobayashi and Y. Kida, "Tolerance of the optic apparatus in single-fraction irradiation using stereotactic radiosurgery: evaluation in 100 patients with craniopharyngioma," *Neurosurgery* **66**, 688-694 (2010).
53. Y. R. Lawrence, X. A. Li, I. el Naga, C. A. Hahn, L. B. Marks, T. E. Merchant and A. P. Dicker, "Radiation dose-volume effects in the brain," *Int J Radiat Oncol Biol Phys* **76**, S20-S27 (2010).
54. F. A. Mettler, W. Huda, T. T. Yoshizumi and M. Mahesh, "Effective doses in radiology and diagnostic nuclear medicine: a catalog," *Radiology* **248**, 254-263 (2008).
55. NCRP, "Ionizing Radiation Exposure of the Population of the United States," National Council on Radiation Protection and Measurements Report No. 160 (2009).

## BIOGRAPHICAL SKETCH

Justin Hanlon was born in 1985 in Nashua, New Hampshire. The older of two children, he grew up in Auburn, New Hampshire, and graduated from Pinkerton Academy in 2003. He earned his B.S., a dual degree in nuclear engineering and engineering physics, at Rensselaer Polytechnic Institute, in 2007.

In 2007, he was granted admission to the Ph.D. program within the Nuclear and Radiological Engineering Department at the University of Florida to perform research as a graduate assistant in computational medical physics. Since September 2007, he has worked closely with Oraya Therapeutics Incorporated, a medical device development company based in Newark, California, which funded his research.

He completed his Ph.D. degree at the University of Florida in August 2010.